**MARMARA UNIVERSITY**

**INSTITUTE FOR GRADUATE STUDIES**

**IN PURE AND APPLIED SCIENCES**

# LEVAN-ENCAPSULATED MAGNETIC NANOCOMPOSITES

İLKER ÇALGERİŞ

**Ph.D. THESIS**

Department of Bioengineering

**ADVISOR**

Prof. Dr. Ebru TOKSOY ÖNER

İSTANBUL, 2017

**MARMARA UNIVERSITY**

**INSTITUTE FOR GRADUATE STUDIES IN PURE AND APPLIED**

# LEVAN-ENCAPSULATED MAGNETIC NANOCOMPOSITES

İLKER ÇALGERİŞ

(724210001)

**Ph.D. THESIS**

Department of Bioengineering

**ADVISOR**

Prof. Dr. Ebru TOKSOY ÖNER

İSTANBUL, 2017

# MARMARA UNIVERSITY

## INSTITUTE FOR GRADUATE STUDIES IN PURE AND APPLIED SCIENCES

İlker ÇALGERİŞ, a Doctor of Philosophy student of Marmara University Institute for Graduate Studies in Pure and Applied Sciences, defended her thesis entitled "Levan-encapsulated Magnetic Nanocomposites", on..... and has been found to be satisfactory by the jury members.

**Jury Members**

| | | |
|---|---|---|
| Prof. Ebru TOKSOY ÖNER<br>Marmara University | (Advisor) | ..... |
| Prof. Mehmet S. EROĞLU<br>Marmara University | (Jury Member) | ..... |
| Assist. Prof. Seval GENÇ<br>Marmara University | (Jury Member) | ..... |
| Assoc.. Prof. Ahmet C. GÖREN<br>The Scientific and Technological Research Council of Turkey | (Jury Member) | ..... |
| Assist. Prof. Cem ALTAN<br>Yeditepe University | (Jury Member) | ..... |

**APPROVAL**

Marmara University Institute for Graduate Studies in Pure and Applied Sciences Executive Committee approves that İlker ÇALGERİŞ is granted the degree Doctor of Philosophy in Department of Bioengineering, Program on 06.07.2017. (Resolution no: 2017/14-02)

**Director of the Institute**

**Prof. Dr. Uğur YAHŞİ**

**ACKNOWLEDGMENTS**

The research presented in this thesis was conducted at Biongineering Department of Marmara University and School Of Chemicals and Material Engineering (SCME) of National University of Sciences and Technology (NUST) in Islamabad-Pakistan from 2010 to 2017. During this period, I have received great help in various ways that I wish to acknowledge here.

I would like to first express my gratitude to my advisor Prof. Ebru TOKSOY ÖNER for her continuous guidance, generous support, and valuable advice I received through my education. Also, thanks to Prof. Mohammed MUJAHID and Prof. Mehmet S. EROĞLU for their support in this study and giving me opportunity of working in SCME and polymer chemistry laboratories.

I express my endless thanks to Assist. Prof. İftihar GUL, Assoc. Prof. Yalçın ARGA, for their contributions to my academic career prior and during the thesis.

I present my special thanks to Assist. Prof. Özlem ATEŞ, Assist. Prof. Hande KAZAK, Dr. Deniz KÖŞEBENT, Merve ERGİNER for being more than friends and never letting me fall down in hard times.

I also want to thank Mr. Shems UDDIN, Mr. Tanveer ul Haq ZIA for their helps and friendship during the studies I have conducted in the laboratory of NUST.

I appreciate SCME and Bioengineering and Chemical Engineering Departments for their support in this study and giving me opportunity of working in their laboratories.

I wish to express my love and gratitude to my beloved family; for their support, understanding and endless love, through my life and my studies. I want to thank my mother Fatma ÇALGERİŞ, my father Hasan ÇALGERİŞ for their encouragement and assistance. At last, I would like to express gratitude to my wife Hülya EFE ÇALGERİŞ for her deeply support and love. Our sons Ömer Mete and Oğuzhan are worth everything in life and I would not have finished this thesis without their endless love. This thesis is dedicated to my family whom I owe my all.

**June 2017** **İLKER ÇALGERİŞ**

# TABLE OF CONTENTS

# ÖZET

## LEVAN-KAPLAMALI MANYETİK NANOKOMPOZİTLER

Hipertermi, kanserli hücrelere hedeflenen metal nanopartiküllerin manyetik özelliği kullanılarak sıcaklığın yükseltilip kanserli hücrelerin vücuttan temizlenmesini sağlayan alternatif tedavi yöntemidir. Demir oksit nanopartikülleri bioyuyumlu olması ve fonksiyonel grupların takılabilirliğinden dolayı bu uygulama için uygun adaylardır. Bu tez çalışmasında $CoFe_2O_4$ nanopartikülü ortak çöktürme metodu ile sentezlenmiştir. Sentez aşamasında sıcaklık ve pH parametreleri değiştirilerek bu çalışmada en uygun koşullarda $CoFe_2O_4$ sentezi yapılmıştır. FTIR, SEM, EDS AFM, TG-DTA, VSM, manyetik ısıtma testleri 85$^oC$ reaksiyon sıcaklığı ile pH12' de optimum özelliklerde $CoFe_2O_4$ nanopartikülleri elde edildiğini göstermiştir. $CoFe_2O_4$ nanopartiküllerine N-(Phosphonomethyl)iminodiacetic acid hydrate (PMIDA) bileşiği kullanılarak –COOH fonksiyonel grupları takılmıştır. Modifiye $CoFe_2O_4$ nanpartiküllerine Folik asit takılarak kanserli hücrelere hedefleme tasarlanmıştır. Folik asit üzerindeki hidroksil grubu ile modifiye $CoFe_2O_4$ üzerindeki karboksil grubu etkileşerek ester bağı oluşturmuştur. Bu bağ FTIR analizinde tespit edilmiştir. Bu aşamada nanopartiküllerin floresans spektroskopisindeki özelliği araştırılmış ve 265-300nm aralığında floresans özelliği gözlenmiştir. Nanopartikül büyüklükleri SEM ve AFM sonuçlarından anlaşıldığı üzere ortalama 20nm civarındadır. Çıplak nano parçacıklar kimyasal olarak aktiftirler, hava ile kolayca okside olurlar ve biraraya gelerek enerjilerini azaltmak eğilimindedirler. Bu nanopartiküller sentez sonrasında stabilize edilerek bu problem kolayca aşılabilir. Bu çalışmada, levan fosfonat ile nanopartiküller enkapsüle edilerek bu sorun aşılmaya çalışılmıştır. Levan fosfonat, mikroorganizmalardan elde edilen Levan biyopolimerinin $PCl_3$ ile etkileştirilmesi sonucu elde edilmiştir. FTIR, SEM-EDS, AFM analizleri yapılarak elde edilen yapışkan özellliği fazla olan malzemenin fosfonatlanmış levan olduğu anlaşılmıştır. Levan fosfonat ile enkapsüle olmuş nanopartiküller TEM, AFM and SEM ile tespit edilerek son aşamada biyolojik testleri yapılmıştır.

**Haziran 2017** **İlker ÇALGERİŞ**

# ABSTRACT

## LEVAN-ENCAPSULATED MAGNETIC NANOCOMPOSITES

Hyperhermia application is one of the alternative treatment methods that uses the magnetic properties of metal nanoparticles targeted to cancerous cells to increase the temperature and to remove the cancerous cells. Iron oxide nanoparticles are suitable candidates for this application because of their biocompatibility and the ability to attach functional groups. In this work, $CoFe_2O_4$ nanoparticle was synthesized by the co-precipitation method. $CoFe_2O_4$ synthesis was carried out by changing the parameters of temperature and pH in the synthesis phase. FTIR, SEM, EDS AFM, TG-DTA, VSM, magnetic heating tests have shown that $CoFe_2O_4$ nanoparticles are obtained at optimum parameters at pH 12 with a reaction temperature of 85°C. $CoFe_2O_4$ nanoparticles were attached with -COOH functional groups using the PMIDA compound. Modified $CoFe_2O_4$ nanoparticles were designed by attaching folic acid to target cancerous cells. Hydroxyl groups on the folic acid interacted with the carboxyl group on the modified $CoFe_2O_4$ to form ester bond. This bond was detected in the FTIR analysis. At this stage, the properties of the nanoparticles on the fluorescence spectroscopy were investigated and fluorescence properties were observed in the range of 265-300 nm. Nanoparticle sizes were about 20 nm as understood from the SEM and AFM results. Nanoparticles are chemically active, readily oxidized by air, and tend to aggregate to reduce their energy. These nanoparticles can be stabilized after synthesis to overcome this problem easily. In this study, this problem was tried to overcome by encapsulating nanoparticles using levan phosphonate. Levan phosphonate was obtained with the interaction of $PCl_3$ and levan biopolymer. FTIR, SEM-EDS, AFM analysis were performed and it was understood that the material with excess adhesive property is phosphonated levan. TEM, AFM and SEM Mapping results showed that nanoparticles encapsulated with levan phosphonate were identified. At the final stage, encapsulated nanoparticles were biologically tested.

**June 2017** **İlker ÇALGERİŞ**

# CLAIM FOR ORIGINALITY

## LEVAN-ENCAPSULATED MAGNETIC NANOCOMPOSITES

Microbial levan has many remarkable properties such as great biocompatibility, strong adhesivity, and film-forming ability, which offers a variety of industrial applications in the fields of cosmetics, health, foods and pharmaceuticals. However, some of the disadvantages of biodegradable polymers obtained from renewable sources is their dominant hydrophilic character, fast degradation rate and unsatisfactory mechanical properties, especially under wet environments. Considering this fact, levan was modified with phosphate groups for overcoming these drawbacks in this study. Levan phosphonate can be a useful material as well as having too many application areas as a pure material for biomedical industry. $CoFe_2O_4$ nanoparticles are considered to have biomedical application such as hyperthermia therapy due to their unique physical and chemical properties. The nanoparticles should be small enough to escape from the macrophages in the RES and large enough not to leak into the capillaries. These properties will allow longer circulation in the bloodstream. Nanoparticles are chemically active, readily oxidized by air, and tend to aggregate to reduce their energy. These nanoparticles can be stabilized after synthesis to overcome these problems easily. In this study, this problem was surmounted by encapsulating nanoparticles using levan phosphate. Sulfate, hydroxyl and carboxyl groups present on the surface show relatively more RES absorption. The levan was modified with phosphate to try to reduce the hydroxyl groups present. Hydrophilic polymers escape more easily from macrophages in the RES and act as a kind of shield protecting blood proteins from binding to nanoparticles. Considering the hydrophilic character and biocompatibility of the levan phosphonate, it may be a good biopolymer for encapsulation. In this study, -COOH functional groups were attached to $CoFe_2O_4$. Then, Folic Acid was tagged to modified $CoFe_2O_4$ as a ligand and then encapsulated with levan phosphonate. For hyperthermia application, a novel levan encapsulated magnetic nanoparticles design were performed within this study. This is a new method for targeting strategy and levan phosphonate was firstly used in the literature for hyperthermia application.

**June 2017** **Prof. Ebru TOKSOY ÖNER** **İLKER ÇALGERİŞ**

## AIM OF THE THESIS

Cancer is a genetic disease that is caused by an uncontrolled division of abnormal cells. Today, cancer disease threatens humanity more than it did in the past. There are many types of cancer treatments. But side effects on healthy cells may lead to negativities in patients' quality of life. Alternative treatment methods are being developed every passing day. Hyperhermia application is one of these alternative treatment methods that uses the magnetic properties of metal nanoparticles targeted to cancerous cells for removing the cancerous cells. In this treatment, abnormal cells are exposed to 41-46°C and they do not sustain uncontrolled division due to the deterioration of their metabolism.

In this study, a novel nanomaterial is aimed to be synthesized for hyperthermia application. $CoFe_2O_4$ nanoparticles are considered to have biomedical applications such as hyperthermia due to their unique physical and chemical properties. The first part is concentrated on the optimization and characterization of $CoFe_2O_4$ nanoparticles. Co-precipitation method was used that is widely used for biomedical applications due to the ease of implementation and need for less hazardous materials and simple procedures. AFM, SEM, XRD, FT-IR and TG-DTA analyses were conducted to confirm the $CoFe_2O_4$ nanoparticles and to get optimum results for further applications. $CoFe_2O_4$ nanoparticles were analyzed for magnetic and electrical properties with LCR meter and vibrating sample magnetometer. And then, PMIDA was attached to $CoFe_2O_4$ nanoparticles. As a ligand, Folic Acid was tagged to modified nanoparticles. Small sized nanoparticles are chemically active, are readily oxidized by air, and tend to aggregate to reduce their energy. These nanoparticles can be stabilized by encapsulating them using polymers such as levan phosphonate. Sulfate, hydroxyl and carboxyl groups present on the surface show relatively more RES absorption. The levan was modified with phosphate to reduce the hydroxyl groups present. Hydrophilic

polymers escape more easily from macrophages in the RES and act as a kind of shield protecting blood proteins from binding to nanoparticles. Considering the hydrophilic character and biocompatibility of the levan phosphonate, it may be a good biopolymer for encapsulation.

Microbial levan is a homopolymer of fructose with many remarkable properties like hydrophilic character, strong adhesivity, well biocompatibility and film forming capability. Levan has industrial importance, which proposes a variety of industrial applications in the fields of pharmaceuticals, health, cosmetics and foods. Modified levan can be a useful material for biomedical industry, as well as being too many application areas as a pure material. Levan phosphonate was obtained with the reaction of $PCl_3$ and levan biopolymer at Marmara University Chemical Engineering Laboratories. F-TIR, SEM- EDS, AFM and Contact Angle analyses were performed to check structure, physicochemical and topographic properties and it was understood that the material with excess adhesive property is phosphonated levan.

Within the scope of this study, novel application areas were investigated for chemically modified forms of levan polysaccharide and $CoFe_2O_4$. They were characterized both chemically and biologically. Then, using this knowledge, potential biomedical applications can be proposed for these biomaterials.

The results of the proposed work can serve as a framework for biomedical application of modified levan and modified nanoparticle based nanocomposites.

# SYMBOLS

**G** : gram

**mg** : Mili grams

**µg** : Micro grams

**L** : liter

**mL** : mili liters

**µL** : micro liters

**M** : molar

**H** : hour

**min** : minute

**nm** : nanometer

**Mw** : weight average molecular weight

**rpm** : Round per minute

**J** : Joule

**W** : Watts

**V** : Volts

# ABBREVIATIONS

| | |
|---|---|
| **NPs** | : Nanoparticles |
| **CFO** | : $CoFe_2O_4$ |
| **AFM** | : Atomic Force Microscopy |
| **STM** | : Scanning Tunneling Microscope |
| **DDS** | : Drug Delivery Systems |
| **DI** | : Deionize |
| **EDS** | : Energy Dispersive Spectroscopy |
| **Ac.A** | : Acetic Acid |
| **LP** | : Levan Phosphonate |
| **FDA** | : Food and Drug Administration |
| **FT-IR** | : Fourier Transform Infrared Spectroscopy |
| **XRD** | : X-ray Powder Diffraction |
| **QDs** | : Quantum dots |
| ***In vitro*** | : Cells or biological molecules studied their laboratory environment |
| ***In vivo*** | : Cells or biological molecules studied in a normal biological environment |
| **PBS** | : Phosphate Buffer Saline |
| **SEM** | : Scanning Electron Microscopy |
| **TG-DTA** | : Thermogravimetric (TG) and Differential Thermal Analysis (DTA) |
| **UV** | : Ultraviolet |

| | |
|---|---|
| **TE** | : Temperature Effect |
| **PE** | : pH effect |
| **$T_C$** | : Curie Temperature |
| **H** | : Magnetic Field |
| **B** | : Magnetic Induction |
| **$M_s$** | : Saturation Magnetization |
| **$M_r$** | : Remanent Magnetization |
| **$H_c$** | : Coercive Field |
| **LCR meter** | : a type of electronic test equipment used to measure the inductance (L), capacitance (C), and resistance (R) of an electronic component |
| **$dH_2O$** | : Deionized water |
| **έ** | : Dielectric constant |
| **ε″** | : Dielektric loss |
| **tan δ** | : Dielectric tangent loss factor |
| **CTAB** | : Cetrimonium bromide |
| **PMIDA** | : *N*-(Phosphonomethyl) iminodiacetic acid hydrate |

# LIST OF TABLES

**PAGE**

# LIST OF FIGURES

# LIST OF FIGURES

# LIST OF FIGURES

**PAGE**

# 1. Introduction to Nanotechnology

## 1.1. What`s Nano?

Nowadays, nano is a popular word of science and technology. It has taken the attention of researchers from physics to chemistry, biology and engineering. What is nano? The prefix ‘nano’ , derived from the Greek nanos signifying dwarf, is becoming increasingly common in scientific literature. The definition of word nano is a physical length scales that are on the order of a billionth of a meter long. Popularly, ‘nano’ is used as an adjective to describe objects, systems, or phenomena with characteristics arising from nanometer-scale structure. How small “nano” is difficult to imagine, so there are some examples: A human hair is between 80.000 and 100.000 nanometers wide, a sheet of paper is approximately 100.000 nanometers thick. The figure is showing below has three examples of the scale and the size of nanotechnology, [1]

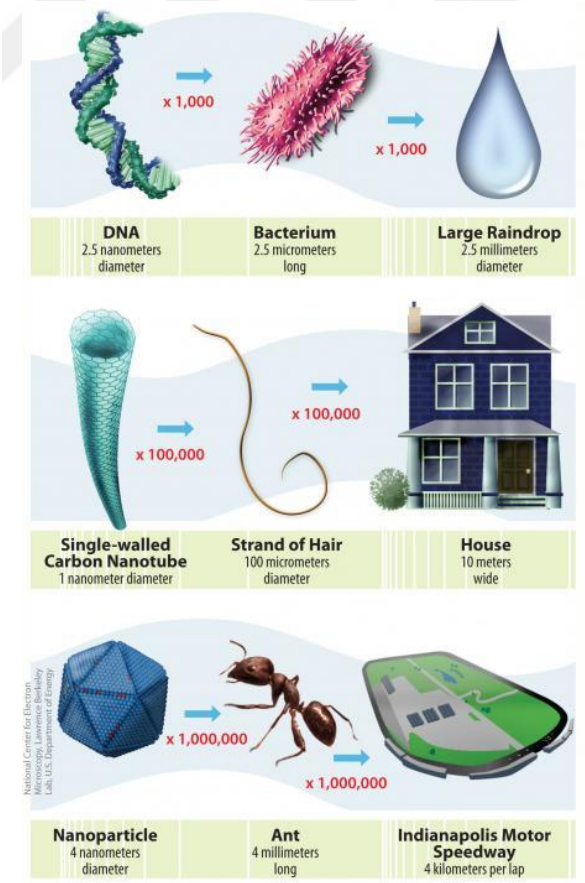


**Figure 1.1.** Size comparison of nano-patterns [1]

### 1.2. History of Nanotechnology

Nanotechnology has existed for a few centuries but has expanded with the occurrence of the Information Age [2]. Scientists had focused on large scale materials in their research for more than a century. The ideas and concepts behind nanotechnology started with a lecture entitled “There’s Plenty of Room at the Bottom” given at the American Physical Society meeting at Caltech by physicist Richard Feynman in 1959. It is frequently quoted as giving birth to the concept of nanotechnology [3]. In his talk, The process has been described by Richard Feynman in which scientists could manipulate individual atoms and molecules, molecules might be controlled [4]. In 1974, First time, the term "nano-technology" was used by Japanese scientist Norio Taniguchi [5]. In 1980, Drexler run against Feynman's lecture "There's Plenty of Room at the Bottom" while preparing his first scientific paper on the subject, “Molecular Engineering: An approach to the development of general capabilities for molecular manipulation” published in the *Proceedings of the National Academy of Sciences* in 1981 [3]. Nanotechnology got an enhancement in the early 1980s with a major development. With the development of the scanning tunneling microscope (STM) that could see individual atoms, that modern nanotechnology began [1].

### 1.3. Differences in Nano and Bulk materials

According to the US Government’s National Nanotechnology Initiative “Nanotechnology is the understanding and control of matter at dimensions of roughly below 100 nanometers, where unique phenomena enable novel applications”. Nanotechnology has generated too many interests in recent years due to the significantly different properties of these novel materials ascribed to their characteristic structural properties in between the isolated atoms and the bulk materials [5,6]. Properties of the materials vary largely as the size of the constituents shifts from bulk to nano size range. There are two important factors between nano and bulk materials. They are surface effects and quantum effects [7]. These factors affect the chemical reactivity of materials, as well as their mechanical, optical, electric, and magnetic properties. Compared to bulk materials, nanoparticles have higher particle number and larger surface area per unit mass. The large surface area of nanoparticles change magnetic properties and show super paramagnetic phenomena because each particle could be considered as single magnetic domain [6]. For instance, the ratio of surface area to volume for a particle with a diameter of 1μm is 1000 times smaller than a particle with a diameter of 1nm. Compared to bulk materials, chemical reactivity of nanomaterial is enhanced roughly

1000-fold. While chemical reactivity generally increases with decreasing particle size, surface coatings and other modifications can have complicating effects, even reducing reactivity with decreasing particle size in some instances [8]. The atoms have less neighbors than bulk atoms at the surface. Hence, the less particle size, the lower binding energy per atom. A result of lower binding energy per atom is a melting point reduction with particle radius, following the Gibbs-Thomson equation. For example, the melting temperature of 3 nm gold nanoparticles is more than 300 degrees lower than the melting temperature of bulk gold [7].

Other factor is quantum effects. Quantum dots (QDs) are quite small particles or nanocrystals of a semiconducting material with diameters in the range of 2-10 nanometers [9]. These nanoparticles frequently have unexpected optical properties called quantum effects. Synthesised QDs have great fluorescence properties which can be used in the imaging instead of the organic labels that can produce different colors determined by the size of the particles [10].

### 1.4. Crystal Structure of Nanoparticles

Crystallography is a study for determining the arrangement of atoms in the crystalline solids. Symmetry and crystal's structure play a role for determining nanoparticle's physical properties like electronic band structure, optical transparency and cleavage [11]. Unit cells create a crystal structure. The unit cell is a small box containing one or more atoms arranged in 3-dimensions that contains all of the structural and symmetry information to build-up the macroscopic structure of the lattice. It describes a extremely ordered structure, occurring due to the intrinsic nature of its constituents to form symmetric patterns [12]. Angles and lenghts of the cell edges are the lattice parameters which represent a unit cell. The positions of the atoms inside the unit cell are measured from a lattice point and it is described by the set of atomic positions ($x_i$ , $y_i$ , $z_i$). **Figure 1.2** shows the structures of unit cells [13].

Here, we will focus on the cubic category due to $CoFe_2O_4$, which are simple cubic, body-centered cubic, and face-centered cubic. Cubic unit cells are very important that is relatively easy to do calculations since the cell-edge lengths are all the same and the cell angles are all $90^o$ [14].

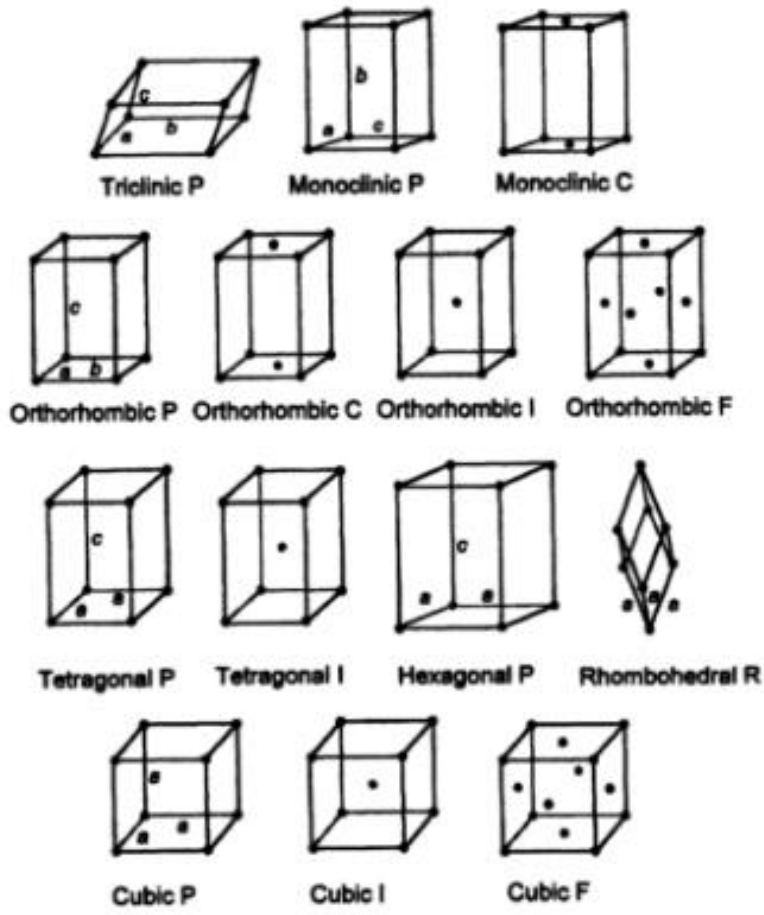


**Figure 1.2.** The structures of Bravais unit cells [15].

### 1.4.1. Simple Cubic Structure

In a simple cubic structure, the simple cubic unit cell is the simplest repeating unit. Each corner of the cubic unit cell is described by a lattice point at which an atom, molecule, or ion could be found in the crystal. The unit cell, at the edge, always connects equivalent points. An identical particle must be contained at the eight corners of the unit cell. Other particles may be present at the edges, faces or within the body of the unit cell. But, to be classified as simple cubic, eight equivalent particles on the eight corners must be present in the unit cell [16].

### 1.4.2. Body-Centered Cubic Structure

In a body-centered cubic structure, the simplest repeating unit is the body-centered unit cell. Once more, there are eight identical particles on the eight corners of the unit cell. On the other hand, there is one more identical particle in the center of the body of the unit cell [16].

### 1.4.3. Face-Centered Cubic

The face-centered cubic unit cell is the simplest repeating unit in a cubic closest-packed structure. The face-centered cubic unit cell starts with identical particles on the eight corners of the cube. For a total of 14 identical lattice points, this structure contains the identical particles in the centers of the six faces of the unit cell [16] .

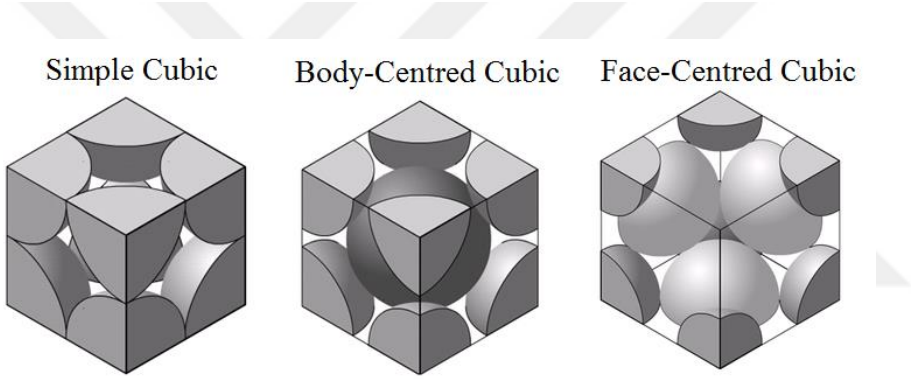


**Figure 1.3**. 3D view showing the number of atoms per unit cell [17].

## 1.5. Miller indices

In the crystal structure, directions and planes are defined with three integers. Normally, these values are created by using the Miller indices. Miller indices parameters are decided by finding the intersection of the plane with the x, y, z axis. Miller index notation ($\ell mn$) describes vectors and planes [18].

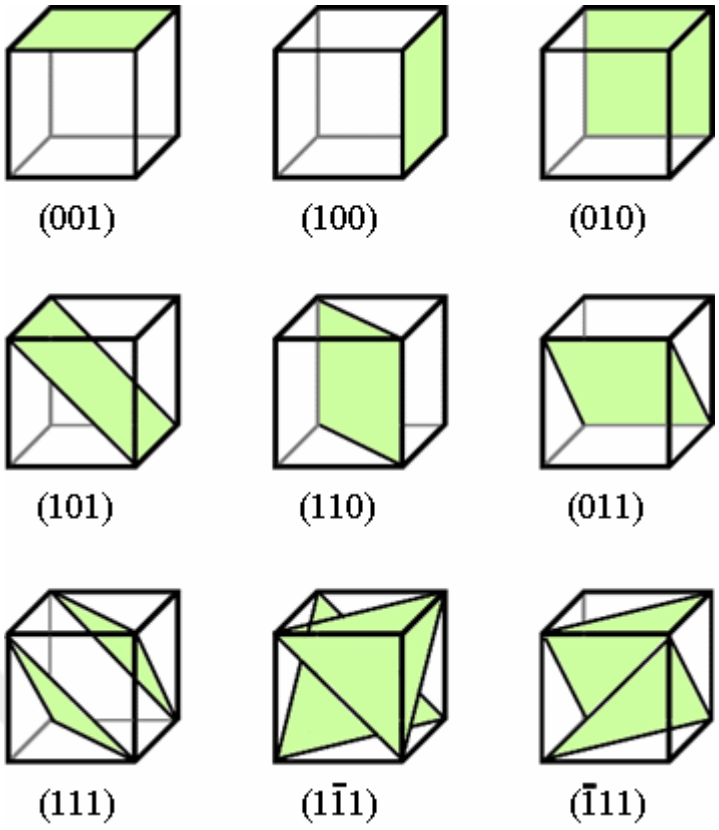


**Figure 1.4.** Cubic Planes [19].

### 1.6. Magnetic properties of Nanoparticles

Magnetism is a feature of materials which relates to the magnetic moments when an external field is applied. According to Pauli Exclusion Principle, an orbital contains only two electrons, and the two electrons must be opposing spins. While an electron is “spin up”, the other is “spin down”. In case, magnetic fields are in opposite directions , they may cancel each other. On the other hand, an atom contains one or more unpaired electrons whose spin can form a directional magnetic field. The direction of the magnetic field is determined by the spin up or its opposite directions [20]. Magnetism generally arises from electric current, because of moving electric charges create magnetic fields. Materials have a tendency to orient in a special direction. The region is called as the magnetic domain where alignment takes place. In magnetic domains, dipoles spontaneously align due to the exchange interaction. These are ferromagnetic, ferrimagnetic and antiferromagnetic materials. However, for paramagnetic and diamagnetic materials, the dipoles align in response to an external field [21].

### 1.6.1. Paramagnetism

Paramagnetic properties is a form of magnetism in which material contains unpaired electrons. These unpaired electrons are randomly oriented and whose spins align themselves when a external magnetic field is applied, and turn to its nonmagnetic state as soon as the external field is removed.

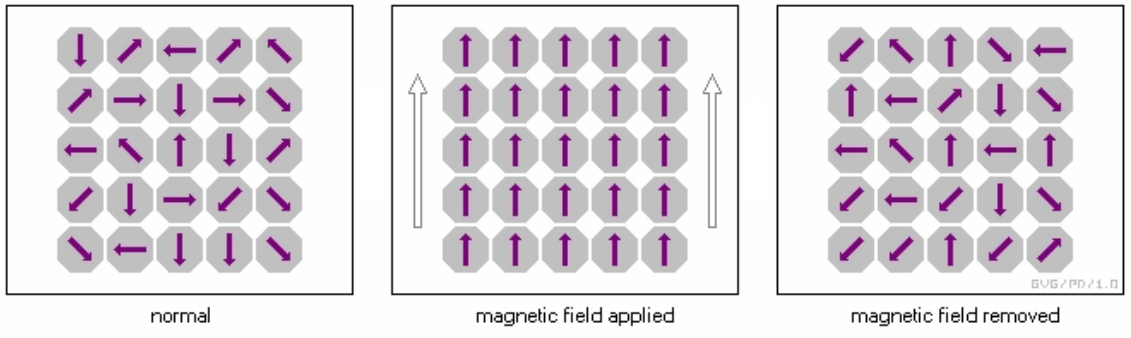


**Figure 1.5**. Magnetic properties of paramagnetic materials [23]

### 1.6.2. Diamagnetism

Diamagnetism is called that the tendency of magnetism in opposite direction to an externally magnetic field and diamagnetic behavior are repelled by the applied magnetic field. Diamagnetic behavior is observed only in purely diamagnetic material. While paramagnetic material has unpaired electrons, diamagnetic material has not unpaired electrons. Due to the absence of unpaired electrons diamagnetic molecules, they are electrically "stable" when exposed to electromagnetic field. The diamagnetic effect of materials is not permanent that is being immediately canceled when the field is removed [24].

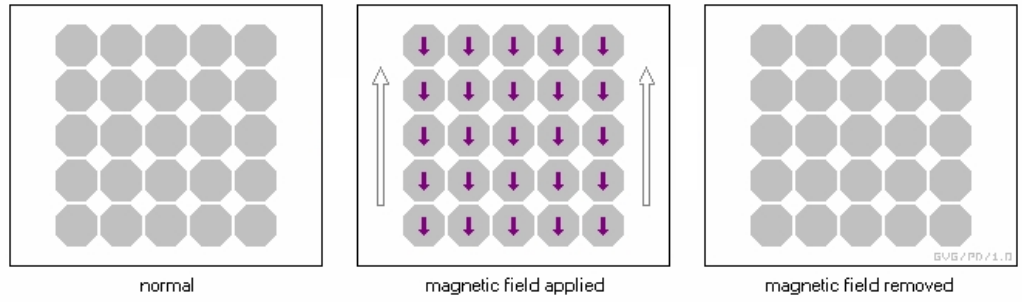


**Figure 1.6**. Magnetic properties of diamagnetic materials [23]

### 1.6.3. Ferromagnetism

Ferromagnetic material that easily form magnets, contains unpaired electrons like paramagnetic substance. These materials contain a tendency to orient parallel with each other to maintain a lowered-energy state. This tendency related to lining up parallel to external magnetic field. Hence, the electrons maintain their parallel orientation, when the applied field is removed. Every ferromagnetic material has itsown critical temperature, known as the Curie point. At this point, the material loses its ferromagnetic properties. Well known ferromagnetic materials are iron, nickel, cobalt and their associated alloys [25].

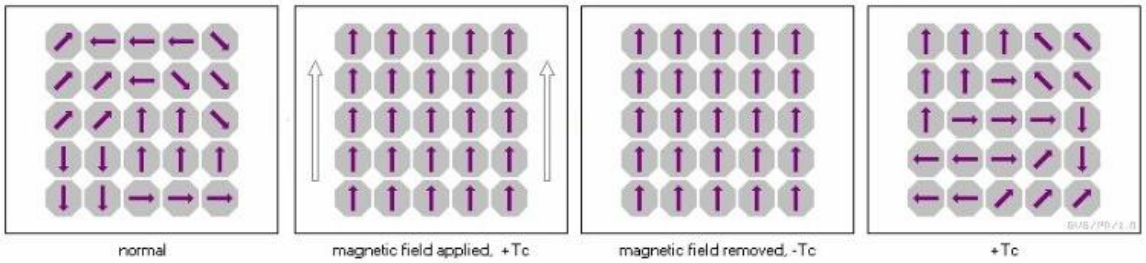


**Figure 1.7**. Magnetic properties of Ferromagnetic materials [23]

### 1.6.4. Antiferromagnetism

Because of magnetic moments of neighboring valence electrons point in opposite directions, antiferromagnetic materials have a zero magnetic moment that generate no magnetic field [25] .

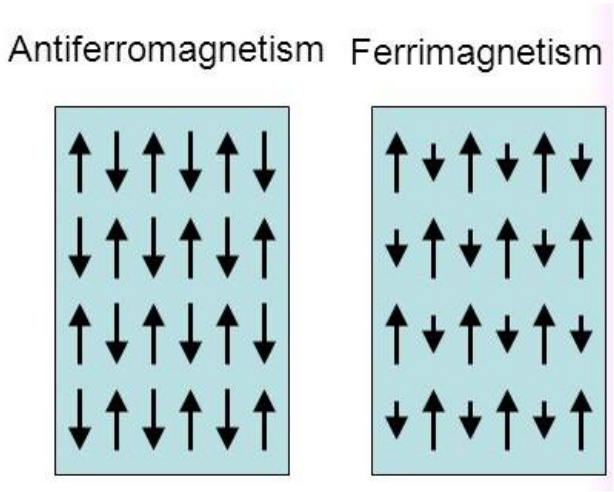


**Figure 1.8**. Magnetic properties of Antiferromagnetism and Ferrimagnetic materials [26]

### 1.6.5. Ferrimagnetism

Ferrimagnetic materials have common properties with ferromagnetic and antiferromagnetic materials. They retain magnetization like ferromagnetic materials when a magnetic field is removed. However, their neighboring electron pairs are similar to antiferromagnetic materials, magnetic moments of neighboring valence electrons point in opposite directions [25]**.**

## 1.7. Magnetic Quantities of Nanomaterials

There are three magnetic vectors. Magnetization or magnetic polarization is expressed as a net magnetic moment per unit volume or mass that is indicated as 'M'. B is called the magnetic induction and H is magnetic field. All parameters related to $B = \mu_0 (H+M)$ equation and $\mu_0$ is shown free space as permeability. M-H loop called hysteresis curve also shows all the magnetic properties including saturation magnetization ($M_s$), remanent magnetization ($M_r$), coercive field ($H_c$) as shown in **Figure 1.9**. The ability of the magnetic material to get easily magnetized and easily demagnetized describes the nature of the magnetic material [27].

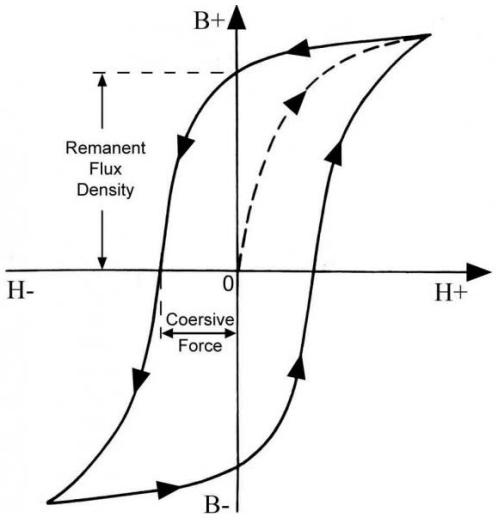


**Figure 1.9**. Hysteresis loop of ferromagnetic materials [28]

Magnetic hysteresis curve also decides soft or hard materials. While hard magnetic materials are permanently magnetized, soft magnetic materials are temporarily magnetized. Coercive field ($H_c$) is smaller for soft materials and larger for hard materials. Hence, hard materials are difficult to magnetize because of larger coercivity. Other important feature is Remanent magnetization ($M_r$) that is the magnetization left when external field is removed [29]. $CoFe_2O_4$ nanoparticles show a relatively large magnetic hysteresis which seperates it from other spinel ferrites [30].

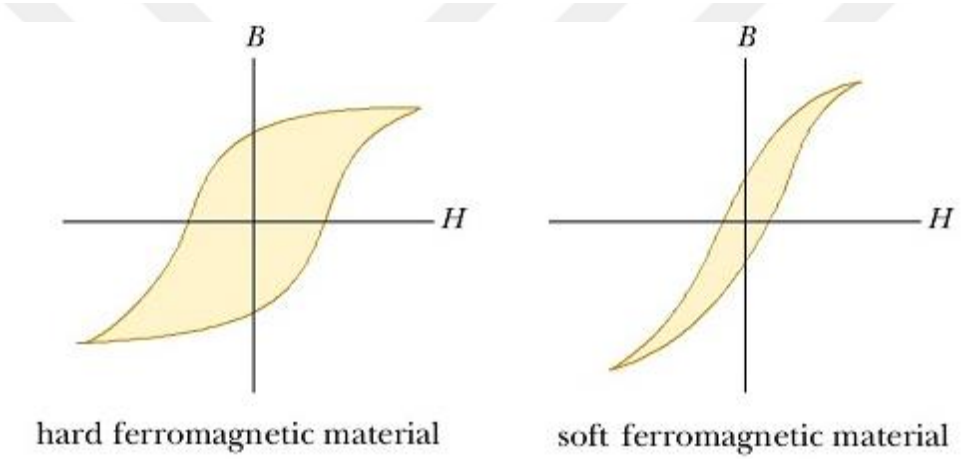


**Figure 1.10.** Hysteresis loops of hard and soft ferromagnetic materials [31]

### 1.8. Curie Temperature

Material's intrinsic magnetic moments are different for ferromagnetic, paramagnetic, ferrimagnetic and anti ferromagnetic materials that depend on temperature. It is the critical temperature that also called Curie point (Tc). At this critical temperature, where a material's permanent magnetism changes to induced magnetism.

| **Below $T_c$** | **Above $T_c$** |
|---|---|
| Ferromagnetic | ↔ Paramagnetic |
| Antiferromagnetic | ↔ Paramagnetic |

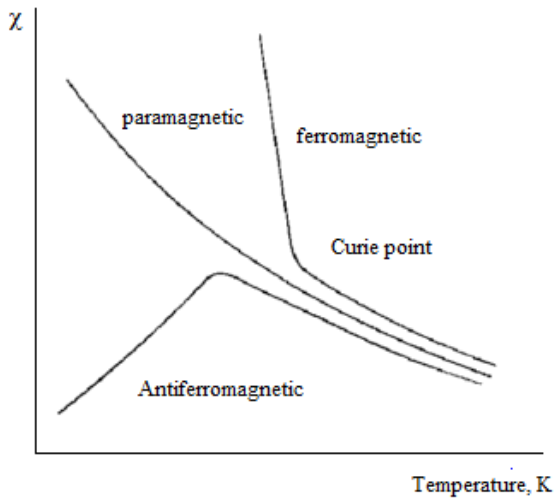


**Figure 1.11** .Curie Point refers to a characteristic property of a magnetic material [32]

In Ferromagnetic materials, the magnetic moments are aligned at random at temperatures above the Curie point, and become ordered below the Curie Point. As the temperature is increased towards the Curie point, the magnetization within each domain decreases. Above the Curie point, the material is purely paramagnetic and there are no magnetized domains of aligned moments [33]. Doping a material can affect its Curie Temperature. Composite materials may have different curie temperatures than a constituent of a composite. The Curie temperature (Tc) of ferromagnetic nanoparticles decreases with decreasing nanoparticle sizes. Nanoparticles shape is also depend on its curie temperature [34]. Curie Temperature of $CoFe_2O_4$ nanoparticles is around 520 $^oC$ [35].

## 1.9. Properties of Cobalt based Ferrites

Ferrite nanoparticles show extraordinary physical and chemical properties. Its properties are changed with the particle size, shape, crystallinity, composition, cation distribution, and synthesis route [36]. General formula of magnetic spinel ferrites is $AO.B_2O_3$ or $AB_2O_4$ where, A is divalent metal ion like $Mn^{2+}$, $Zn^{2+}$, $Ni^{2+}$, $Fe^{2+}$, $Cd^{2+}$, $Cu^{2+}$, $Mg^{2+}$ and $Co^{2+}$ (or a mixture of such ions) and B is trivalent metal iron ion [37].

In magnetic spinel ferrites, both divalent and trivalent cations are distributed among tetrahedral (A) and octahedral (B) sites. The site preference exhibited by cations defines whether the spinel is normal or inverse. In normal spinel, the $A^{2+}$ ions occupy only tetrahedral sites and the $Fe^{3+}$ ions occupy only octahedral sites, for example $ZnFe_2O_4$. In inverse spinel,

all the $A^{2+}$ ions and half the $Fe^{3+}$ ions sit on the octahedral sites; the tetrahedral sites are occupied now by the other half of the $Fe^{3+}$ ions like $NiFe_2O_4$ and $CoFe_2O_4$ nanoparticles [38].

$CoFe_2O_4$ is shown as CFO that is interesting nanoparticles due to its large curie temperature, high effective anisotropy and moderate saturation magnetization [39]. Spinel ferrites are widely used as a material in different applications such as magnetic recordings and storage, catalysis, magnetic resonance imaging, targeted drug delivery and hyperthermia for cancer treatment [40,41]. Recent innovative applications are focused on the use of transition metal nanoparticles like Cobalt ions. $Co^{2+}$ also has a important role as a co-factor for B12 vitamin [42,43].

Cobalt based nanoparticles have the ability to rapidly enter into the cell which attracts attention of the researchers to Cobalt based NPs for biomedical applications [44].

## 1.10. Synthesis of Metal Nanoparticles

Recently, researches argue about several techniques for preparing metal nanoparticles. Various synthesis methods have been designed to obtain optimum sized nanoparticles and they depend upon many different parameters including reaction time, reaction temperature, pH, stirring rate and concentration of reactants. Synthesis methods for nanoparticles can be listed as follows:

### 1.10.1. Sol-Gel Method

The sol-gel process is important method to synthesize nano ferrites. In this method, nanomaterials are fabricated starting from an aqueous solution of salts (sol) to an integrated network of particles (gel) like a polymer. Metal nitrates or chlorides are subjected to hydrolysis and condensation that forms a colloidal suspension.

**Hydrolysis step (sol )** : $M\text{-}O\text{-}R + H_2O \rightarrow M\text{-}OH + R\text{-}OH$

**Condensation step (gel )** : $M\text{-}OH + R\text{-}O\text{-}M \rightarrow M\text{-}O\text{-}M + R\text{-}OH$

Solvent type, reaction temperature, pH, stirring rate, catalysts, additives and precursors are important parameters in a sol–gel process [44]. Low cost, optimum

agglomeration and uniform morphology of the nano particles are the specific advantages of sol-gel synthesis technique [45].

### 1.10.2. Solvothermal Synthesis

High pressures above the boiling points of a liquid solvent in a sealed closed vessel called as autoclave is generally utilized for synthesis of metal nanoparticles in hydrothermal method. Solvents are heated in the autoclave in which pressure is generated. This reaction requires long times (8-72 hrs) at high temperatures generally between 130 $^{o}$C and 200 $^{o}$C. If water is used as a solvent, the reaction is called as hydrothermal synthesis method [46]. Comparing to other syhthesis techniques, easy control of particle size and shape, uniform and narrow size distribution, composition of prepared samples are achieved in this method. Also, there is no requirement of sintering of the precursor samples to form crystallite sizes of the materials [45].

### 1.10.3. Micro-emulsion Method

Micro-emulsion method is ideal techniques for the preparation of metal nanoparticles. Micro- emulsion means a clear, thermodynamically stable, isotropic liquid mixture of water, oil and surfactant [47]. Micro-emulsion is formed when an enough amount of a suitable surfactant is mechanically agitated with the oil phase and water phase. The aqueous phase may contain salt(s) and/or other ingredients, and the oil phase is a mixture of surfactant in a suitable organic solvent. There are two basic types of microemulsion. One of them is normal micelles (oil dispersed in water) and the other is reversed micelles (water dispersed in oil). Small sized particles can be achieved in this method Also, uniform size distribution and morphology is possible by this technique. [45].

### 1.10.4. Chemical co-precipitation

Co-precipitation is a four step mechanism to synthesize nanoparticles at varied temperature that means the co-precipitation of ionic salts such as nitrates, chlorides, sulphates in the presence of a strong base such as NaOH or $NH_4OH$. These four steps include nucleation, growth, ripening and saturation of particles [45]. Nucleation is a key step in this method and many small nuclei are formed that pass the growth step followed by ripening and then stabilization process and a stable insoluble product is formed. The size and magnetic properties of nanoparticles can be varied depending on types of salt, pH and temperature of

reaction, concentration of reagents and mixing of base [48]. Slow mixing can cause a large size nanoparticles formation and a sudden mixing of basic solution can induce growth small particles due to sudden creation of nuclei [45].

### 1.11. Fluorescent Properties of Nanoparticles

Small semiconductor nanoparticles are called quantum dots (QDs) whose sizes are in the range of 1 – 20 nm. Synthesised QDs have great fluorescence properties which can be used in the imaging instead of the organic labels. They can be used to biosensing, biolabelling and delivery of therapeutic agents Quantum dots are used in medicine, food safety control and environment monitoring [49]. Due to quantum confinement, different size quantum dots emit different color light. The smaller quantum dots the bluer its absorption onset and fluorescence spectrum (higher energy). Conversely, The large quantum dots emit redder light (lower energy) [50]. Different color of quantum dots are shown in **Figure 1.12.** The absorbance and fluorescence spectrum of QDs are measured by fluorescence spectrometer.

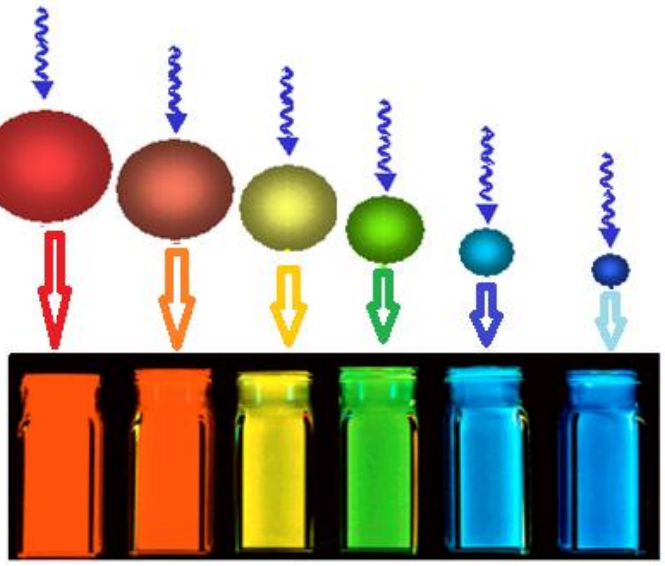

**Figure 1.12.** Six different quantum dots solution are shown excited with a long wave [51].

## 1.12. Cancer and Cancer Therapy

Cancer is a genetic disease that caused by an uncontrolled division of abnormal cells. Thus, abnormal cells could spread all over the body [52]. There are many kinds of cancer that are usually named for the organs or tissues where the cancers form. They all start because of out-of-control growth of abnormal cells. Understanding of DNA, which was found to be the basis of the genetic code that gives orders to all cells, they learned that chemicals, radiation damage to DNA or viruses cause different DNA sequences that often bring about cancer [53].

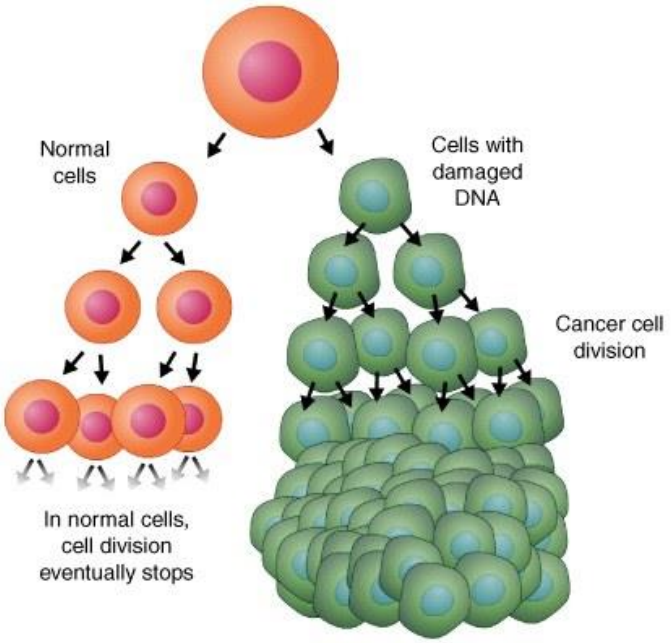


**Figure 1.13**.Cancer cell division [54].

Some cells continue to form new abnormal cells instead of dying. These abnormal changes called hyperplasia and dysplasia are formed before cancer. In hyperplasia, cells within a tissue divide faster than normal cells but the cells look normal under a microscope.

Dysplasia is more serious step in which the cells look abnormal under a microscope but this abnormality is not cancer. Hyperplasia and dysplasia are both the way of cancer and they might be cancer or might be not [55]..

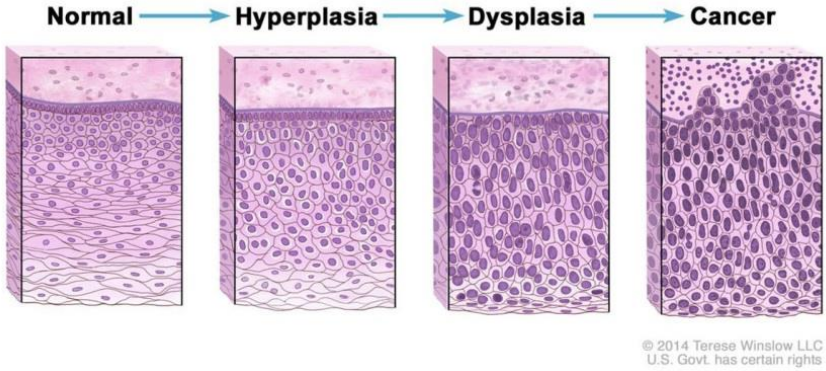


**Figure 1.14.** The loss of normal growth [56].

Cancer cells are dividing continuously due to the ignorance of stop signals. In terms of cell division, cancer cells differ from normal cells. These differences can be arranged as following;

- Normal cell requires growth factors to divide. But, cancer cell has lost the requirement of positive growth factors. Because of this reason, abnormal cells divide whether these factors are present or not.
- Normal cells indicate contact inhibition. It is meant that normal cells respond to contact with other normal cells stopping cell division. That's why, normal cell can divide to fill in an emptiness, until filling the gaps with enough cells. There is not this feature in cancer cells and abnormal cells keep on growing even they touch other cells. This abnormality causes a large mass of cells [57].
- Programmed death of cell is called apoptosis is the normal process for normal cell [58]. According to Hayflick phenomenon, a normal human cell can divide until cell division stops that approximetly divide in a range of 40 to 60 times. Telomere is a region at the end of a strand of DNA that get smaller as the cell divides. The length of the telomere is related to their capability to replicate DNA [59,60]. On the other hand, telomerase is an enzyme that is activated in cancer cells. Due to this enzyme, the length of the telomere is never getting smaller. This property gives infinite replicative potential to cancer cells [61].

- Due to DNA damage or abnormal cell division, normal cells stop to divide and causes apoptosis unlike normal cells. Cancer cells continue to divide when cell division is abnormal. Hence, the more damaged DNA is accumulated in the body [62].

Cancer can be treated by surgery, chemotherapy, radiation therapy, hormonal therapy, and targeted therapy.

### 1.12.1. Surgery Method

Surgery is the oldest type of cancer therapy that is the removal of the tumor and surrounding tissue at an early stage of disease. In surgery, cutting process is painful and take some time to recover. After the discovery of anesthesia (1846), surgery advanced so rapidly that the next 100 years became known as "the century of the surgeon." Anesthesia makes you feel painless during surgery. But, there is some complications such as blood loss and if the cancer later appear elsewhere, it should be a new process. In the 1970s, Clinical tests demonstrated that, the less extensive surgery, the more effective result. Most women that have breast cancer, have the primary tumor removed and then use of radiation to damage cancer cells [63-65].

### 1.12.2. Chemotherapy

Chemotherapy is one of the most effective conventional treatment methods that is therapeutic agents to cure cancer, increase the insufficiency of surgery or radiotherapy and help painless operation. Before surgery or radiation therapy, chemotherapy makes a tumor smaller that is called neo-adjuvant chemotherapy. After surgery or radiation therapy, it destroys cancer cells that is called adjuvant chemotherapy [66]. Chemotherapy therapeutic agents also cause some side effects that affects healthy cells and many chemotherapy drugs may cause birth defects. It is important that a woman should avoid to become pregnant while undergoing chemotherapy [67]. Chemotherapy drugs are metabolized in the liver which might be damaged if liver is not working healthy and the higher doses drugs the greater damage of liver. This damage occurs frequently in elderly people and those that have a history of hepatitis [68].

### 1.12.3. Radiation Therapy

Radiation therapy is a cancer treatment method that uses high-energy radiation to minimize the tumors or destroy cancer cells by damaging the DNA. Types of radiation are X-rays, gamma rays, and charged particles that may be delivered by a machine outside the body, or it may come from radioactive material placed in the body near cancer cells. Radiation therapy not only destroy cancer cells but also may lead to side effects that can damage normal cells [69].

### 1.12.4. Hormonal Therapy

Hormones are natural substances that are body's chemical messengers carried in bloodstream from one part to another of body. Cancer cells are either hormone sensitive or hormone dependent. Some cancer cells need hormones to grow. In hormone therapy for hormone dependent cancer, medicines are used to block the growing effects of hormones. But, this application is not useful for all types of cancer. This type of cancer cells is called hormone sensitive such as breast cancer, prostate cancer. The common side effects of hormone therapy for women and men are tiredness, mood swings and depression, weight gain and effects on bones [70]. Additionally, in almost all patients, resistance develops that initially respond to therapy and result in cancer progression. The molecular causes of resistance are complex, varied and not well understood [71].

## 1.13. Targeted Therapy and Hyperthermia

Targeted anti-cancer therapy is an effective treatment that is a special type of chemotherapy. But, targeted therapy works in a different way unlike standard chemotherapy. Chemotherapy drugs target certain parts of cancer cells that make them different from standard chemotherapy. Instead of chemotherapy, based upon non-toxic inorganic and organic nanoparticles may improve current cancer treatments such as targeted therapy called Hyperthermia. According to National Cancer Institute in the United States of America, hyperthermia is defined as follows; tumor is exposed to high temperatures to damage, kill or to make more sensitive cancer cells for alternative therapies such as radiation and certain anticancer drugs. Hyperthermia is a type of treatment that body tissue is exposed to high temperatures in the range of 41-46 $^{o}$C to damage cancer cells or to make more sensitive for effects of anticancer drugs. Heating is generated by radio frequency, microwave

and laser wavelengths. Cancer cells are considered more susceptible to heat than normal cells due to their higher rates of metabolism. Because of this reason hyperthermia is promising cancer treatment [72]. Hyperthermia application is classified into three categories as localized hyperthermia, regional hyperthermia and whole-body hyperthermia [73–75]. The goals of targeted nanoparticle systems are to increase the nanoparticle concentration in only tumor cells, improve internalization and intracellular delivery [76]. Targeted therapies also work in several ways.

### 1.13.1. Passive Targeting

The control of the size and surface properties of nanoparticles in the treatment of cancer is very critical because of necessity of avoiding uptake by the reticulo-endothelial system (RES), maximizing circulation times and targeting ability [77]. RES recognizes foreign substances and eliminates them from blood circulation. There are some differences between tumor and normal cells. Tumor veins are disorganized and enlarged with a high number of pores that resulting in enlarged gap junctions between endothelial cells. This property is named enhanced permeability and retention (EPR) effect. The EPR effect is an important mechanism for selective solid tumor targeting of nano-scale drug carriers and has been the basis for novel drug carrier design [78-80]. EPR effect might be observed in nearly all human cancers apart from prostate cancer or pancreatic cancer which are a kind of hypovascular tumors [81,82].

Passive targeting consist of the transport of nanocarriers through leaky tumor capillary fenestrations into the tumor cells by convection or passive diffusion. The convection is called the motion of molecules within fluids. As the net filtration rate is zero, convection must be in the majority transport mode for most large molecules. In the contrary, low molecular weight compounds are mostly transported by diffusion. Diffusion is defined as a process of transport of molecules across the cell membrane without cellular energy. At the same time, convection through the tumor cells is poor due to interstitial hypertension, leaving diffusion as the major mode of drug transport [83].

Especially, there are three important nanocarrier properties. They are listed as following;

1. The ideal nanocarrier size should be in the size range of 10-100 nm. EPR effect allows migration of macromolecules up to 400 nm in diameter into the surrounding tumor region. Nanocarriers need to be larger than 10 nm to avoid the filtration from the kidneys nanocarriers need to be smaller than 100 nm.
2. The charge of the nanoparticles should be anionic or neutral for efficient flowing of the renal elimination.
3. The nanocarriers should be hidden from the RES [84,85].

At the same time, there are some limitations to reach tumor on passive targeting. Firstly, it depends on the degree of tumor vascularization and angiogenesis. Secondly, the high interstitial fluid pressure of solid tumors avoids successful uptake and homogenous distribution of drugs in the tumor [86,87].

### 1.13.2. Active Targeting

Active targeting is a new and the most promising method. Specific ligand is attached to the surface of the nanocarrier for targeting cancer cell directly or onto its surface by binding antigens of tumors [77,88,89]. Proteins, glycolipids, peptides, polysaccharides, glycoproteins, and monoclonal antibodies are used as a ligand for surface modification of nanocarriers which principally bind to receptors at the target site [90]. Most of the active targeting conjugates have a structure composed of a ligand and an active chemotherapeutic drug or nanoparticles. The ligand is chosen for attaching to a receptor overexpressed by tumor cells and not expressed by normal cells. The binding affinity of the ligands influences the tumor penetration because of the binding-site barrier. After binding to target cells, internalization occurs via receptor-mediated endocytosis [91]. In the active targeting strategy, two cellular targets can be seperated: first one is the targeting of cancer cell showing in **Figure 1.15 B1** and the second one is the targeting of tumoral endothelium showing in **Figure 1.15 B2**.

| | Passive targeting | Active targeting |
|---|---|---|
| (1) | Utilizes the special deviated conditions prevailing in the diseased portion of the body | Depends on the species that is overexpressed during disease |
| (2) | Less selective | Highly selective |
| (3) | Restricted in use | Very versatile |
| (4) | More likely to produce side effects | Less likely to induce side effects |

**Table 1.1.** The comparison of passive and active targeting [91].

Ligands grafted at the surface of nanocarriers bind to receptors over expressed by (1) cancer cells or (2) angiogenic endothelial cells.

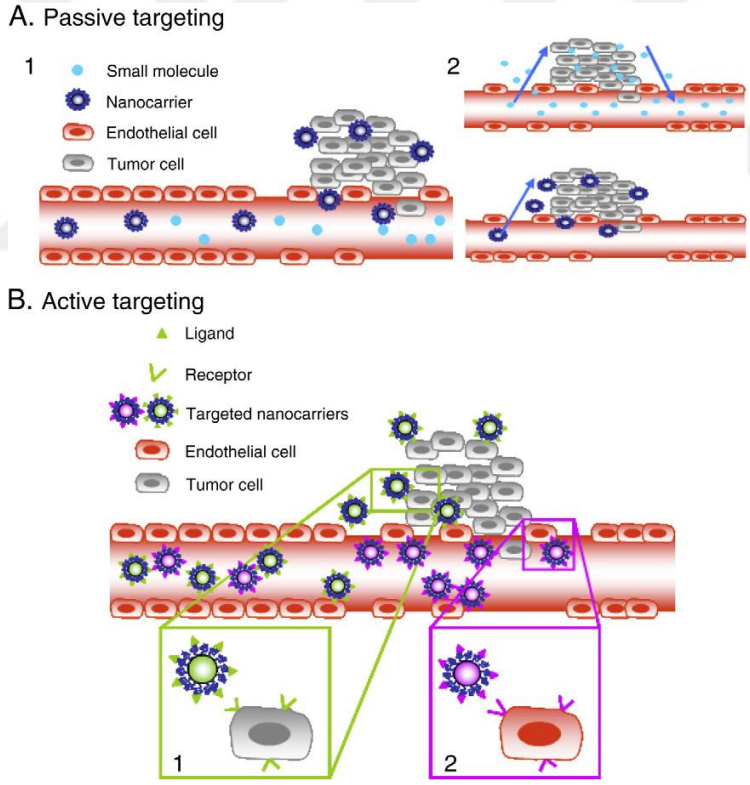


**Figure 1.15.** A. Passive targeting of nanocarriers. B. Active targeting strategies.

## 1.14. Nanoparticle Targets on the Body

There are many factors to the design of active targeting nanoparticles before choosing the target of interest [92]. It is most important that the target receptor should have high density on target cells. It should be overexpressed on the diseased tissue while minimum expressed on the normal tissue. Affinity and specificity are crucial parameters for a targeting ligand [93]. The main targets on the body are shown in **Table 1.2**.

| Target | Description |
|---|---|
| Folate receptor | A folate-binding protein. Folate receptor-tageted epothilone BMS 753493 contains an epothilone moiety linked to a single folate molecule. It delivers the antimitotic epothilone component into cells expressing folic acid receptors, frequently unregulated in tumor cells. |
| Peptide receptor | A cell surface protein that binds peptides with high affinity |
| Cell membrane | Also called the plasma membrane, plasmalemma or "phospholipid bilayer", it is a semipermeable lipid bilayer found in all cells |
| Cell surface antigen | Antigens on surfaces of cells, for example, infectious or foreign cells or viruses; they are usually protein-containing groups on cell membranes or walls |

**Table 1.2.** The main Targets on the Body

## 1.15. Folic Acid as a Targeting Ligand

One of the most significant limitations of cancer therapy is the lack of the specificity of anti cancer nanoparticles delivery. Choosing the suitable ligand is highly important for the proficiency of actively-targeted nanoparticles. There are specific features between cancer and normal cells. Cancer cells frequently express several proteins on the cell surface [94-96]. The Low molecular weight (MW) targeting agents, such as folic acid (FA), and its counterpart, the Folate receptor (FR), have emerged as the most promising way for

selective cancer therapy [52]. The natural characteristics of folic acid and folic acid receptors on cancer cells make them very efficient agents for drug targeting being fixed the severe side effects of free drugs and overcome drug resistance. Normal cells do not express FR. Folate was picked because of folate employed as a targeting moiety of various anticancer agents to avoid their nonspecific attacks on normal tissues as well as to increase their cellular uptake within target cells [97]. Folate conjugates are covalently derivatized via its g-carboxyl moiety and it is well known that they can retain the high affinity ligand binding property of folate, and the kinetics of cellular uptake of conjugated folate compounds by folate receptors are similar to that of free folate. Recycling of folate receptors in target cells can make more accumulation of folate conjugates possible. Other folate conjugates such as protein toxins, radio imaging agents, chemotherapy agents, anti-T-cell receptor antibodies, and gene transfer vectors have also demonstrated receptor-specific delivery properties. Many researchers have used folic acid (FA) as a ligand with cationic liposomes and other polymers such as chitosan, poly(L-lysine), poly(dimethylaminomethyl methacrylate) and PEI [98]. The conjugation of folic acid to therapeutic agents including alkylating agents, taxols, platinum compounds, and fluorouracil has been investigated [99].

Folic acid receptors are two different forms following as;

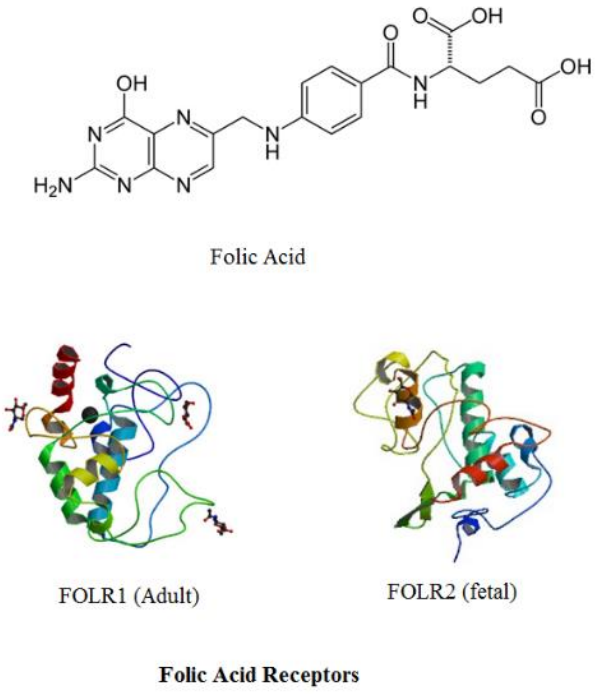


**Figure 1.16**. Folic acid and folate receptor [100].

One of them is FOLR1 that is overexpressed by a number of epithelial-derived tumors including ovarian, breast, renal, lung, colorectal, and brain. The other form of folic acid receptor is FOLR2 that was originally thought to exist only in placenta, but also it is detected in spleen, bone narrow, and thymus [101].

### 1.16. Types of Nanoparticles Used for Active Targeting Systems

Comparing to other cancer therapeutics, advantages of the nano particles have been defined by Heath and Davis based on four important properties as follows;

1. Nanoparticles have therapeutic or diagnostic properties that can transport a complex and extremely concentrated therapeutic agent.
2. Nanoparticles can bind to targeting ligands which yield high affinity and specificity for target cells.
3. Nanoparticles could accommodate multiple drug molecules that allow combinatorial cancer therapy.
4. Nanoparticles can bypass multiple drug resistance mechanisms [102].

Owing to the advantages of nano-scaled size, nanoparticles are able to overcome barriers in human body, reaching specific sites of abnormal cells and remaining there longer to realize higher bioavailability.

Nanoparticles are usually composed of biodegradable polymers and have the advantage of specificity, the ability to escape from multi-drug resistance and efficient drug delivery. Drug delivering nanoparticles are also termed as nanocarriers. Nanocarrier systems increase local drug concentration by carrying drugs to the targets and control releasing when bound to the target abnormal cells. Several nanocarriers such as metallic nanoparticles, liposomes, polymeric nanoparticles, micelles, chitosan nanoparticles, proteins, viruses, carbon nanotubes, gold nanoparticles have been reported for drug targeting. A nanocarrier should have some specific properties such as biocompatible, biodegradable, hydrophilic character and also have potential for surface modification. The most important reasons for this modification are to increase solubility, stability and extended duration of drugs in blood circulation and to add a passive or active targeting groups to these nanocarriers [90,103-105].

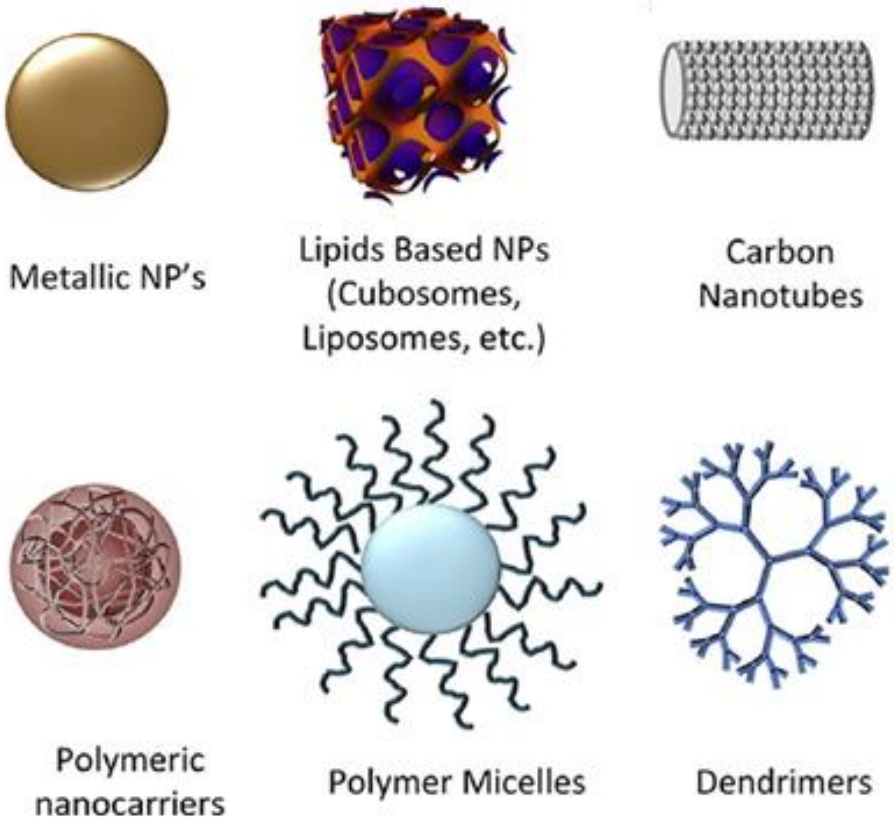


**Figure 1.17.** Types of nanocarriers for drug delivery [106].

Nanoparticles, ranging size of 1 to 100 nm, have been designed as targeting drug delivery vehicles from a variety of materials including lipid based nanoparticles (liposomes, hexasomes, cubosomes), metallic nanoparticles (iron oxide, gold), carbon nanotubes, or polymers based nanoparticles (polymer based micelles, drug carriers, dendrimers) depicted in **Figure 1.17.**

### 1.16.1. Dendrimers

A dendrimer is defined as synthetic polymeric macromolecule in nanometer sizes that has three distinguished architectural components. A central core which is either a single atom or an atomic group, in which branches extended from the core, composed of repeating units and many terminal functional groups generally located in the exterior of the macromolecule. These functional end groups have a large potential for drug attachment. Dendrimers offer various advantages that make these nanocarriers ideal drug delivery vehicles.

- Suitable particle size of dendrimers makes them less susceptible for RES uptake.
- Various functional groups are present on outer surface of dendrimers, which could be used to bind vector devices for targeting to correct site in the body.
- Dendrimers could be modified as stimuli responsive to release drug.
- Dendrimers may show an EPR effect which allow them to target tumour cells more effectively than small molecules.
- They can be synthesized and designed for specific applications. They are ideal drug delivery systems, due to their feasible topology, functionality and dimensions. The easily modifiable surface characteristic of dendrimers has had a promise for biomedical applications, because it enables them to be conjugated with imaging contrast agents, targeting ligands and therapeutic [104,106,107].

Following polymers are using in designing dendrimer that are polyamidoamine (PAMAM), polypropyleneimine (PPI), poly L-glutamic acid (PLG), melamine, PEI, PEG, and Chitin.

Specific molecular structure of dendrimers enables them to carry various drugs via encapsulation or covalent conjugation to the surfaces in the gaps of the cores through hydrogen bond, chemical linkage, or hydrophobic interaction. Despite of the promising feature, dendrimers require many repetitive steps for synthesis for large-scale production and more expensive than other nano carriers [104,109]. There are four important methods for synthesis of dendrimers which are divergent, convergent, double exponential mixed growth and hypercores branched monomers growth.

### 1.16.1.1. Divergent Method

In this method, dendrimer expands outwards from a multifunctional core molecule. The core is reacted with at least two moles of reagent containing two or more protecting branching sites, followed by removal of the protecting groups. This processes are repeated till the dendrimer of the planned size is obtained [110].

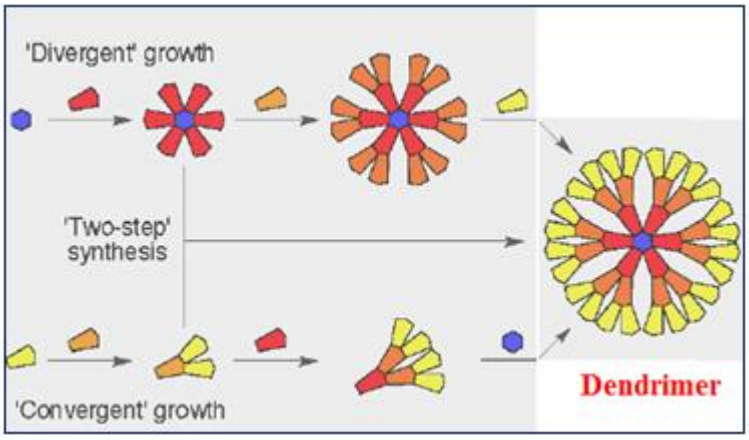


**Figure 1.18.** Divergent and convergent methods for synthesis of dendrimers[111].

### 1.16.1.2. Convergent Method

In the convergent approach, the dendrimer is established stepwise that is starting from the end groups and progressing inwards. When the growing groups are large enough, more branching sites are attached to a suitable core to give a complete dendrimer. There are some advantages in this method like easy to purify the final product, formation of defects in the desired structure is minimised and not allow the formation of high generation dendrimer because stearic problems [112].

### 1.16.1.3. Double Exponential and Mixed Growth

In this method, there are two products (monomers for both convergent and divergent growth) that are reacted together to give an orthogonally protected trimer, which may be used to repeat the growth process again [110,112].

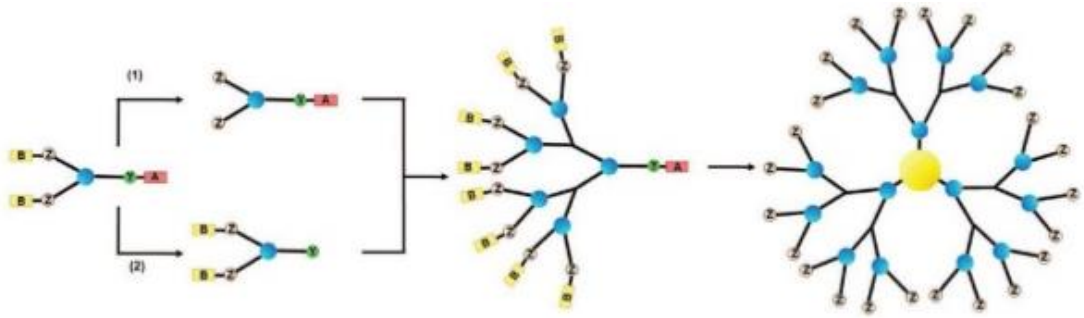

**Figure 1.19.** Double Exponential and Mixed Growth methods for synthesis of dendrimers[113].

#### 1.16.1.4. Hypercores Branched Monomers Growth

Hypercores branched polymers also belong to a class of synthetic tree-like macromolecules that have densely branched structure and a large number of end groups. Hypercores branched polymers which have imperfectly branched or irregular structures whose molecules are composed of repeating units extended from a central core [107].

### 1.16.2. Polymeric Micelles

Polymeric micelles have a great potential as therapeutic nanocarriers that contain a core–shell structure with a versatile drug-loading hydrophobic core and biocompatible hydrophilic shell. This feature of polymeric micelles is preferable to bypass both renal clearance and entrapment by RES. As a result, this is allowed for following accumulation within tumor cells by the EPR effect. Furthermore, polymeric micelles might be designed for enhanced biological performance by modification. According to the characteristics of desired tumor cells, ligand attachment is possible that is called active targeting. Various ligands such as transferrine, folic acid, peptides and some sugars can be attached to polymeric micelles for active targeting [114]. The major factors that influence the performance of polymeric micelles for drug delivery are loading capacity, release kinetics, circulation time, bio distribution, size, and stability and the optimum nanocarriers have some features such as biodegradability, prolonged circulation, high loading capacity, small particle size, and accumulation in tumor cells [115].

### 1.16.3. Polymeric Nanoparticles

Polymeric nanoparticles are in the range of 1-1000 nm that composed of biodegradable polymers such as PLA, PLGA, PEG and polysaccharides include chitosan, clycodextrin, dextrans. Polymers are suitable materials that can be integrated into important nanoparticle constructs with many potential medical applications and polymeric nanoparticles are promising vehicles for drug delivery by effortless manipulation to prepare nanocarriers with the aim of delivering the drugs to specific target. According to preparation method of nanoparticles, two type design could be obtained that are nanocapsules and nanospheres. Nanospheres are also called matrix systems in which the drug is uniformly dispersed, while the drug is covered to a cavity surrounded by a polymer membrane in nanocapsules [115]. Polymeric nanoparticles could be synthesized by various polymerization techniques such as micro-emulsion, surfactant-free emulsion and interfacial polymerization. The choice of preparation technique is based on the basis of a number of factors such as the type of polymeric system, area of application, size requirement and others [107].

There are many advantages of polymeric nanoparticles as follows [116] ;

1. Polymeric nanoparticles are incorporated into other activities related to medical application, such as tissue engineering.
2. Easily and cheaply fabricated in large quantities by various methods.
3. Delivers an optimum concentration of pharmaceutical agent to targeted site
4. Significant improved treatment in terms of efficiency and effectiveness.

### 1.16.4. Carbon nanotubes

Carbon nanotubes (CNTs) are one of the most important materials of nanotechnology. Carbon nanotubes are composed of benzene rings that are unique for their size, shape, and remarkable physical properties. They are hexagonal networks of carbon atoms about 1 nm in diameter and 1–100 nm in length which can essentially be thought of as a layer of graphite rolled up into a cylinder. There are three common techniques for producing CNTs. They are the carbon arc-discharge technique, the laser-ablation technique and the chemical vapor deposition. The resulting products have number of impurities whose type and amount

depend on the technique used. Carbonaceous materials are the most common impurities, whereas the other types of observed impurities are metals. Currently, there are some disadvantages as follows. First, structurally perfect nanotubes is not available at large scale. Second, it is difficult to synthesize defect-free nanotubes continuously to macroscopic lengths. Major drawback of CNTs especially relevant to their compatibility with biological systems is their complete insolubility in all types of solvents [117]. The chemical modifications such as incorporation of carboxylic or ammonium groups to their structures can improve their solubility and make it possible to link and transport of peptides, nucleic acids and other drug molecules. Some examples of performed studies involve the covalent linked antifungal agents and anticancer drugs to carbon nanotubes with a fluorescent agent. An *in vitro* study indicated that drugs bound to carbon nanotubes were more successfully internalized into cells when compared with free drug alone and had potent antifungal activity. The multiple covalent functionalization on the sidewall or tips of carbon nanotubes lets them to carry numerous molecules at once, and this strategy provides an essential benefit in the treatment of cancer [108,109] .

### 1.16.5. Lipid-based drug carriers

These are alternative nanoparticles for therapeutic application made from solid lipids. Solid lipid nanoparticles (SLNs) are also called lipospheres. SLNs formulations are using various application routes such as parenteral administration and brain delivery, ocular delivery, rectal delivery, oral delivery, topical delivery and vaccine delivery systems etc..and thoroughly characterized *in vitro* and *in vivo* [118]. Preparation methods of SLNs are microemulsion, high speed stirring, melt dispersion method, solvent evaporation method and spray congealing. Disadvantages of these nanocarrier systems are their low drug loading capacity, their affinity to polymorphic transition leading to drug expulsion, and the high water content of the SLNs dispersion [119]. Controlled release from lipid based drug delivery systems is a very promising method to overcome barrier associated with the use of approved polymeric systems. Lipid based nanocarrier systems have proofed their capability in terms of biocompatibility, release properties and stabilization of the encapsulated bioactive substances upon preparation and storage.

### 1.16.6. Metallic Nanoparticles

Metallic nanoparticles are highly promising nanocarriers for biomedical application that have many advantages such as easy handling with external magnetic field, the probability of using active and passive targeting strategies, the ability of visualization by MRI, and enhanced uptake resulting in effective treatment at the therapeutically optimal doses [120]. Magnetic nanoparticles have attracted attention on alternative cancer therapy as hyperthermia application [121]. Designing a magnetic drug delivery system requires many factors such as magnetic properties and size of particles, strength of magnetic field, drug loading capacity, the place of accessibility of target tissue. On the other hand, there are some difficulties in achieving these objectives. For example, they tend to aggregate into larger clusters and very difficult for physical handling. Because of the lack of knowledge of the negative effects on the human body, biomedicine applications of MNPs are limited. Iron oxide nanoparticles are the only type of MNPs approved for clinical use by Food and Drug Administration. This feature is achieved by alkaline co-precipitation of $Fe^{2+}$ and $Fe^{3+}$, chemical stability in physiological conditions and possibility of chemical modification by coating the iron oxide cores with various shells such as polymeric, silane , or dendrimeric. In addition, iron oxides – magnetite and maghemite – occur naturally in human heart, spleen and liver, which indicate their biocompatibility and non-toxicity at a physiological concentration. Drug attached to MNP may be achieved by covalent binding, electrostatic interactions, adsorption, or encapsulation process. Targeting of drug-MNPs conjugates to diseased tissues, depending on their size and surface chemistry, can be carried out by passive or active mechanism. Passive targeting is a result of enhanced vascular permeability and retention (EPR) of tumor tissues. Active strategy relies on the attraction of nanoparticle to the affected site by using recognition ligands attached to the surface of MNPs and by handling of an external magnetic field. MNPs coated with long-chain polymers are less cell toxic than MNPs coated with shorter polymer chains of the same type. Magnetic nanoparticles promote activation of phagocytotic and cytokine-release functions of macrophages. In several reports iron oxide was found to accumulate in tissues but without significant histological changes in vital organs [122-132].

It is known that iron oxide NPs can induce oxidative stress by excess of ROS production. The response of defense elements leads to increased expression of antioxidant enzymes, such as heme oxygenase 1 and superoxide dismutase.

## 1.17. Levan and Levan Derivatives

Exopolysaccharides (EPSs) are polymers of sugar residues excreted by microorganisms into the surrounding environment. These macromolecules have long been known to possess a wide range of biological activities, such as antioxidant, anti-mutant, anti-coagulant, immune stimulation, tumor inhibition and stimulation activities depending on their monomer compositions, molecular weights and degree of branching as well as on the presence of functional groups in their structure [134,135]. Besides these structural features, some physical characters such as charge, solubility and conformation of EPSs are also important factors affecting their bioactivities [136]. More importantly, since the chemical and structural features of EPSs are highly determined by the type of the microbial producer and the production conditions. EPSs of each specific microbial system call for individual studies to establish their bioactivities. Due to presence of extreme conditions such as acidity, high temperature, salinity, it is difficult to keep in original function of biopolymer during industrial application. Biopolymers are stable against extreme conditions that are isolated from extremophile microorganisms. Halophilic bacteria is one of them which are capable of living in low water activity environment because of high salt concentration. Hence, levan produced by halophilic bacteria has unique features against extreme conditions [137]. One of the important extremophilic levan producer halophilic bacterium is *Halomonas smyrnensis* AAD6T. Levan is a component of natto whose story has started with it. Natto is a traditional Japanese food that was considered to support healthy and long life. Because of this reason, levan has long attracted the interest of researchers looking for natural products with health benefits. Among the natural polysaccharides, levan is fructose-based polymer which can be excreted by microorganisms as exopolysaccharide or produced in plants for storage that is composed of D-fructo-furanosyl residues joined together by β(2,6) linkages and β(2,1) linkages in core and branch chains, respectively **(Figure1.18)**. Although, different substrates produce similar structured levans, the degree of polymerization and branching of the repeating unit varies from one to another. The reaction conditions also influence the average size and number of branches of the product levan. Relevant reaction factors are enzyme concentration, temperature, ionic strength, and the presence of water-miscible organic solvents [138]. Microbial levan is synthesized by the action of a secreted levansucrase that directly converts sucrose into extracellular polyfructan. Levansucrase catalysed microbial biosynthesis of levan is a step by step process starts with transfer of a hexosyl group from a donor molecule to a growing acceptor molecule. Single fructofuranosyl units are added to the $_{6}$C hydroxyl of the

non-reducing fructose terminal unit of a growing levan polysaccharide chain. Compared to produced levan from plants, microbial levans are more advantageous, economical and industrially feasible with numerous applications. Bacterial levans are much larger than those produced by plants and molecular weights ranging of 2000-100000 kDa. However, produced levans from plants have molecular weights ranging of about 2-33 kDa.

Levan has valuable properties such as high biodegradability, biocompatibility, amphiphilicity, renewability, flexibility, and eco friendly. Moreover, levan offers anti-oxidant, anti-inflammatory, anti-carcinogenic, anti-AIDS, hyperglycaemic inhibitor etc.. Also, It is a natural adhesive and surfactant and widely used in cosmetic industry in the preparation of skin creams, moisturizers etc. The wide range of applications of levan in various industries made it a multipurpose polymer. Large scale production is required for a cost effective process and to meet the demands all over the world [139,140].

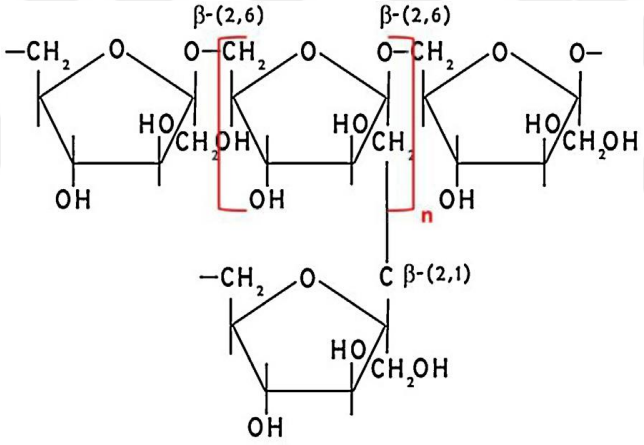


**Figure 1.20**. Structure of the levan [139].

Levan is soluble both in water and oil due to its β(2,6) linkage. Although it has varying solubility in cold water, it is completely soluble in hot water. Unlike other biopolymers, levan does not swell in water. Low intrinsic viscosity and adhesion property make it outstanding polymer compared to other polysaccharides. The furanose ring structure of levan gives enhanced flexibility to the polysaccharide molecule. This outstanding polymer is insoluble in almost all organic solvents such as methanol, ethanol, isopropanol, n-propanol, acetone, methylethylketone, toluene, ethyl lactate, methyl caprylate/caprate,

methylpalmitate/oleate, d-limonene, propylene carbonate, ethylene carbonate, 1-vinyl-2-pyrrolidone, methoxypolyethylene glycol, polyethylene glycol, kerosene, gasoline, dimethyl formamide, ethoxyethyl acetate, acetic anhydride and furfuryl alcohol. Other main features of levan are non-toxic, ocular non-irritant that is heat stable with a melting point temperature of 225 ˚C [141-143]. Also, it is definitely non reducing, not hydrolysed by the action of amylase and invertase.

There are many biomedical applications of levan following as [144-146]. ;

- Obesity and hyperlipidemia are suppressed on laboratory rats by adding levan to the diets
- This outstanding polymer finds many uses in hair fixative products such as a hair holding ingredient.
- Levan-based thin films for healing wounds and burned tissue is one of the most exciting research application.
- Levan enhanced biocompatibility was shown by the increased cell attachment and proliferation.
- Inhibit melanin production by significantly slowing tyrosinase activity, resulting in a "beautifully whitening effect".
- Levan has a role in metalloproteinase activation, a key step in the healing of tissues that have been burned or mechanically damaged.

Polymers obtained from renewable sources have some drawbacks their dominant hydrophilic character, fast degradation rate and, in some cases, unsatisfactory mechanical properties, particularly under wet environments. In order to overcome disadvantages, levan need to be modified to alter their physicochemical properties. Chemical modifications of polysaccharides, such as phosphorylation, sulfonation, oxidation, carboxylation, provide an opportunity to increase their biological activities. Polysaccharides have been chemically modified in various ways to change their physical or biological properties, thus allowing a broader range of applications [147-149]. Modified levan can be a useful material for biomedical industry, as well as being too many application areas as a pure material.

An aqueous solution or gel of levan phosphonate also maintains its gel integrity when frozen and thawed. At the same time, it is still a gel, retains its structure up to 100 $^{o}$C [150]. There are an increasing number of reports on levan and its derivatives. Sulfated linear levan

from *Halomonas* were synthesized and their biocompatibility and anticoagulant activities were investigated. Moreover, Sulfated levan were computationally constructed and docking simulations to understand the effect of sulfation on levan binding to thrombin and antithrombin. Costa et al. (2013) assembled levan-phosphonate and chitosan layer-by-layer to form films on glass slides [151]. They investigated the density of cells adhering to chitosan- phosphonated levan films compared with chitosan-alginate films prepared in a similar manner. Cells adhered greater numbers to the levan-based films as compared to those where the levan was replaced with alginate. Methacrylated with glass nanoparticles showed superior adhesive strength to similar beads prepared with alginate [152]. A carboxymethylated levan was found to increase the tensile strength of chemically damaged hair. Scanning electron micrographs of hair damaged by bleaching showed a decline in the lifting of cuticle layers caused by bleaching after the hair had been treated with derivatized levan [153]. A patent application is claimed that linking the fructosyl moiety to ascorbic acid makes a compound with improved stability to oxidation [154]. Levan or levan phosphonate encapsulated nanoparticles are biocompatible, protein-resistant, non-immunogenic and non-antigenic. Plasma proteins in the blood, attach on the nanoparticles surface and clearance mechanism is activated by the macrophage cells before they cannot reach the target site. A possible approach to prolong the circulation of nanoparticles and achieved to targeting is to functionalize the surface of nanoparticles with a hydrophilic and biocompatible biopolymer such as levan and levan phosphonate [155].

# 2. MATERIALS AND METHODS

## 2.1. Chemicals

The chemicals, solutions and equipments used in this study are given below;

The chemical reagents used in this study are iron (III) nitrate nonahydrate ($Fe(NO_3)_3 \cdot 9H_2O$) (CAS number 7782-61-8), Cobalt(II) nitrate hexahydrate ($Co(NO_3)_2.6H_2O$) (CAS Number 10026-22-9 ) were purchased from Merck Millipore. Phosphorus trichloride ($PCI_3$) (CAS Number 7719-12-2) were purchased from Sigma-Aldrich. Pure *Halomonas* Levan biopolymer was produced at Marmara University Department of Bioengineering as described elsewhere (Poli, Kazak et al. 2009). Sodium carbonate ($Na_2CO_3$) (CAS Number 497-19-8) were supplied from Alfa Aesar. Sodium hydroxide (NaOH) (CAS Number 1310-73-2) and Acetic acid (CAS Number 64-19-7) were supplied from JT Baker. Folic acid (CAS Number 59-30-3) was supplied from Sigma-Aldrich. *N*-(Phosphonomethyl) iminodiacetic acid hydrate (PMIDA) (CAS Number 5994-61-6) and N-(3-Dimethylaminopropyl)-N′-ethylcarbodiimide hydrochloride (EDC) (CAS Number 25952-53-8 ) were purchased from Sigma-Aldrich. Pyridine (CAS No. 110-86-1) and Ethanol CAS No. 64-17-5 were purchased from Merck Millipore. Chloroform ($CHCI_3$) (CAS number 67-66-3,513-35-9) was purchased from Fisher Chemical. Cetrimonium bromide (CTAB) (CAS Number 57-09-0) was supplied from Sigma-Aldrich. Potassium bromide (KBr) (CAS Number 7758-02-3) was supplied from Merck Millipore. All reagents were used without further purification unless otherwise stated.

## 2.2. Equipments and Characterization Techniques

### 2.2.1 Fourier Transform Infrared Spectroscopy

Fourier Transform Infrared spectroscopy is an important technique that is an easy way to identify the presence of certain functional groups in the gas, liquid, and solid samples. FT-IR spectra are obtained by identifying changes in intensity of transmittance or absorption as a function of frequency. Functional groups of molecules absorb at characteristic frequencies of infrared radiation. **Figure 2.1** shows schematic of FT-IR. The beam of light is passed through a series of mirrors that cause the beam's individual wavelengths to hit each other in a way that allows a sample to absorb some wavelengths, while some are blocked. Absorbed light is measured and a computer makes out the absorption rate of each wavelength within the beam [156].

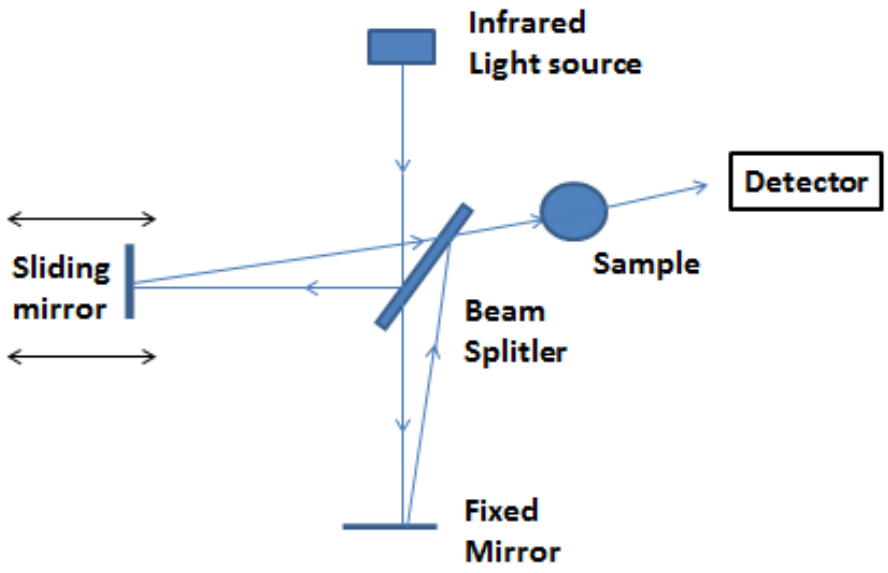


**Figure 2.1** Schematic of FT-IR [157].

### 2.2.2 X-ray powder diffraction (XRD)

X-ray diffraction is a technique that analyses solid materials to find out the crystalline nature and crystallographic information of the materials along with their structure related properties like crystalline or amorhous sizes, lattice parameters. *X*-rays are electromagnetic radiations with characteristic wavelength (λ) and frequency (f) between the visible light and gamma rays. When any electrically charged particle of sufficient kinetic energy decelerates, X-rays are produced as a result of this de-excitation. X-rays used for diffraction has the wave length in the range of 0.5Å-2.5 Å that is comparable to the size of an atom [158]. Diffraction is occurred by the scattering of X-rays with a periodic array with long range order and producing constructive interference at specific angles, which contains information about the atomic arrangement within the crystal pattern. The unit cell is the basic repeating unit that repeats in all dimensions to fill space and produce the macroscopic grains or crystals of the material. The crystal system describes the shape of the unit cell whose size is described by the lattice parameters. Angles and lenghts of the cell edges are the lattice parameters which represent a unit cell. The positions of the atoms inside the unit cell are measured from a lattice point and it is described by the set of atomic positions ($x_i$ , $y_i$, $z_i$) [13]. Amorphous materials do not have a periodic array with long-range order, so they do not produce a diffraction pattern. Crystal structures focus on symmetry elements to define the atomic arrangement. Symmetry elements are used to define seven different crystal systems

| Crystal system | Conventional unit cell |
|---|---|
| Cubic | $a=b=c$, $\alpha=\beta=\gamma=90°$ |
| Tetragonal | $a=b\neq c$, $\alpha=\beta=\gamma=90°$ |
| Orthorhombic | $a\neq b\neq c$, $\alpha=\beta=\gamma=90°$ |
| Hexagonal | $a=b\neq c$, $\alpha=\beta=90°$, $\gamma=120°$ |
| Rhombohedral | $a=b=c$, $\alpha=\beta=\gamma\neq 90°$ |
| Monoclinic | $a\neq b\neq c$, $\alpha=\beta=90°\neq\gamma$ |
| Triclinic | $a\neq b\neq c$, $\alpha\neq\beta\neq\gamma$ |

**Table 2.1**.Crystal systems [159].

Diffraction peaks are associated with planes of atoms. Miller indices (hkl) are used to identify different planes of atoms. Observed diffraction peaks can be related to planes of

atoms to assist in analyzing the atomic structure and microstructure of a sample. The working principle of X-Ray diffraction as suggested by Bragg in 1912 is that the diffracted beam is produced by scattering only when certain conditions are satisfied, the law is given in **Eq. (2.1)** [160] :

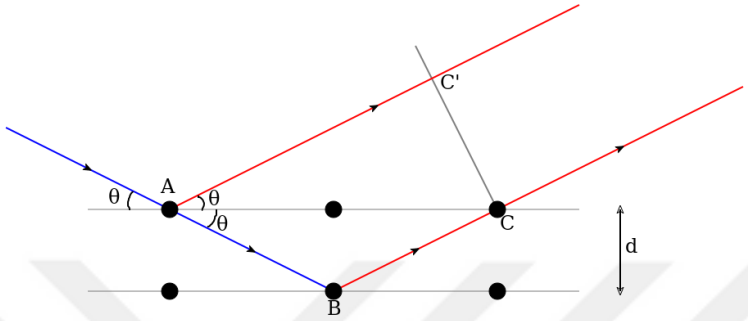


**Figure 2.2** Bragg's law schematics

$$n\lambda = AB+BC \qquad AB = BC \qquad \text{Eq. (2.1)}$$

$$AB = d\sin(\theta)$$

$$n\lambda = 2d\sin(\theta)$$

where, $\lambda$ is the wavelength of X-rays, $\theta$ is the angle between the incident rays and crystal surface, $d$ is the spacing between distinct planes of atoms. The constructive interference occurs when $n$ is an integer. XRD pattern is obtained when a set of parallel and equally spaced atomic planes reflect the incident monochromatic beam of X-ray as per the conditions set by Bragg's Law. Bragg's law provides a simplistic model to understand what conditions are required for diffraction.

### 2.2.3 Scanning Electron Microscope (SEM)

Electron microscopy is a technique that uses a finely focused beam of electrons in order to produce a high resolution image of a sample that are too difficult to analyze by optical microscopes which uses light. Because, the wavelength of the electron beam is much lower than wavelength of the visible light, the magnification of SEM is higher than the magnification of optical microscopes [161]. SEM can magnify above 100,000 times while light microscopes are only able to magnify approximately 1000 times. Besides, resolution of SEM is about 1nm to 20 nm and its images have a three dimensional appearance, which is useful method for examining the surface structure of a sample [162].

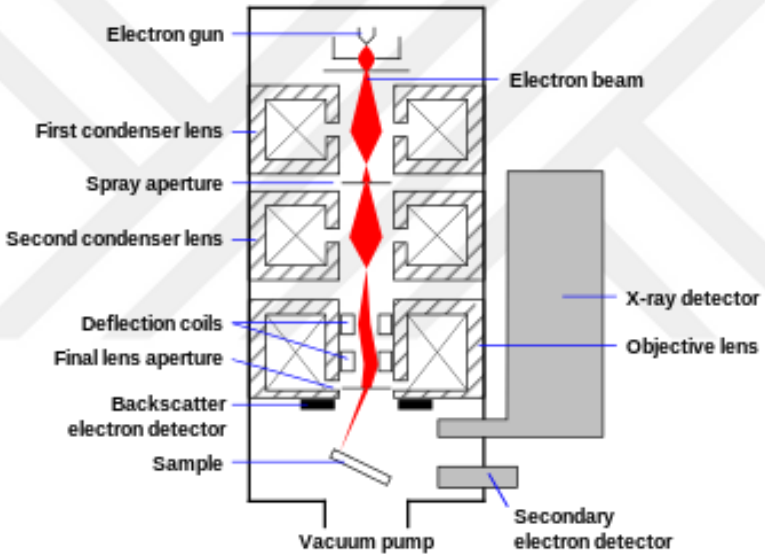


**Figure 2.3**. Schematic of an SEM [163].

The SEM is composed of lenses within a vacuum chamber. The electrons are directed towards the specimen by these lenses in order to maximize efficiency. The incident beam hits a specimen and it emits X-rays and three kinds of electrons which are termed as primary backscattered electrons, secondary electrons and Auger electrons. The more electrons are used, the more powerful the magnification [164].

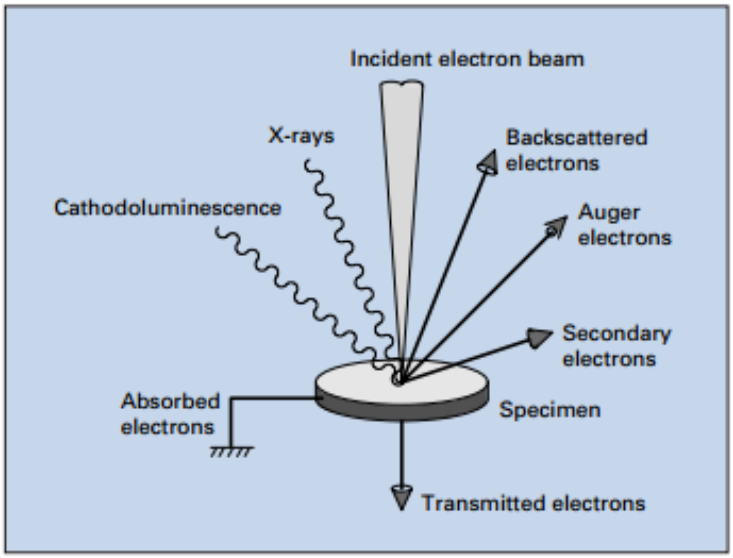


**Figure 2.4** Emission of various electrons and electromagnetic waves from the specimen [165].

Primary backscattered electrons and secondary electrons are used and these rebounding electrons and records their imprint are picked up by an electron recorder. This information is translated onto a screen which allows three-dimensional images to be represented clearly [164].

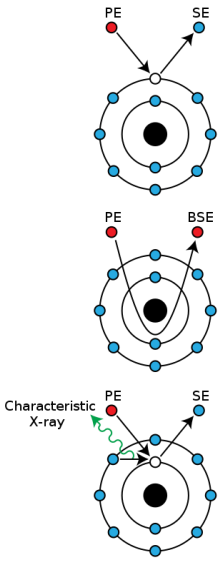


**Figure 2.5** Mechanisms of emission of secondary electrons, backscattered electrons, and characteristic X-rays from atoms of the sample [166].

Traditional SEMs reveal information about the sample's size and topography. But, recent advances in technology have allowed researchers to measure energy marker in the sample's reaction to the incident beam impact. Then, these energy properties are coded with colour and each element producing its own specific marker. Hence, scientists can detect in extreme detail like the borders of each element in the sample by referring to those colors. This process only works for properly prepared specimen. Metals don't require preparation because of their electric conductor properties. However, non-metal specimens need to be preparation with an instrument known as a sputter coater. Sputter coaters provide the specimen with a thin layer of conductive material using noble metals such as Au, Pt, Pd, Pt-Pd, Au-Pd. Because noble metals are stable and has a high secondary-electron yield. In general, thickness of the coated film should be a few thickness to 10 nm [167]. Moreover, coating procedure includes the removal of all water. Water molecules evaporate in a vacuum, creating obstacles for the clarity of the image. The SEM uses Energy-Dispersive X-Ray Spectroscopy (EDS) in the production of elemental maps, which accurately represent the distribution of elements within samples. EDS makes use of the X-ray spectrum emitted by a solid sample bombarded with a focused beam of electrons to obtain a chemical analysis [168].

### 2.2.4 Transmission Electron Microscopy (TEM)

Transmission electron microscopy (TEM) is a technique of electron microscopy where relatively thin specimens can be analyzed as compared to SEM. Transmission electron microscope is a very powerful insrument for material science in which a high energy beam of electrons is shone through a very thin specimen and the interactions between the electrons and the atoms can be used to observe properties such as the crystal structure, features in the structure like dislocations and grain boundaries. TEM also can perform chemical analysis that its high resolution properties can be used to analyze the quality, shape, size and density of quantum wells, wires and dots. TEM contains four parts to be electron source, electromagnetic lens system, sample holder, and imaging system as shown in **Figure 2.6.**

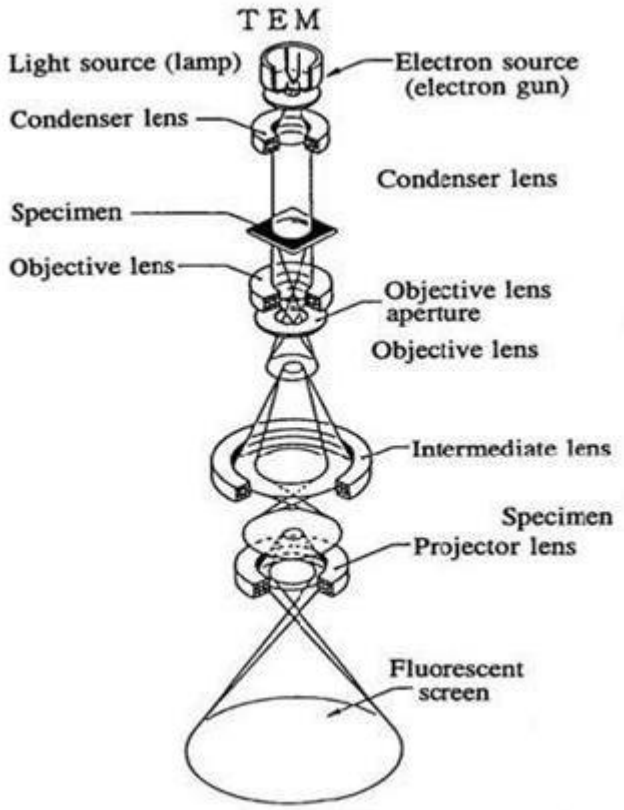


**Figure 2.6.** The schematic outline of a TEM [169].

.

TEM is same as the light microscope that uses electrons instead of light. Because the wavelength of electrons is much smaller than that of light, the optimal resolution accessible for TEM images is many orders of magnitude better than that from a light microscope [170]. Thus, TEMs can reveal the finest details of internal structure in some cases as small as individual atoms. Also, difference from the SEM, relatively thin specimens can be analyzed . TEM has a complex imaging system that contains electromagnetic lens system and screen in order to form the highly fine structural details. The electromagnetic lens system consist of two lens systems where first one refocuses the electrons after they pass through the specimen, the second one enlarges the image and projects it onto the screen. The screen has a phosphorescent plate which shines as electrons hit it. Image is usually recorded on photographic film [171].

### 2.2.5 Thermogravimetric-Differential Thermal Analyzer (TG-DTA)

The Diamond Thermogravimetric-Differential Thermal Analyzer (TG/DTA) uses for thermal analysis of organic and inorganic materials that allows one to determine whether an endothermic or exothermic transition is associated with weight loss in contrast to a melting or crystallization process. Equipment combines the high flexibility of the differential temperature analysis (DTA) property with proven capabilities of the Thermogravimetric (TG) measurement technology. TG/DTA with a high temperature range of ambient temperature to 1500˚C and vacuum capable furnace with forced air cooling. Diamond TG/DTA uses a simultaneous thermos analytical technique measuring weight loss/gain with a horizontal differential balance and change in temperature or heat flow as a function of temperature or time. The heating rate is programmable from 0.01 to 100˚C/min and can operate with various purge gasses and flow rates**. Figure 2.7** shows the schematic outline of TG-DTA instruments [172,173].

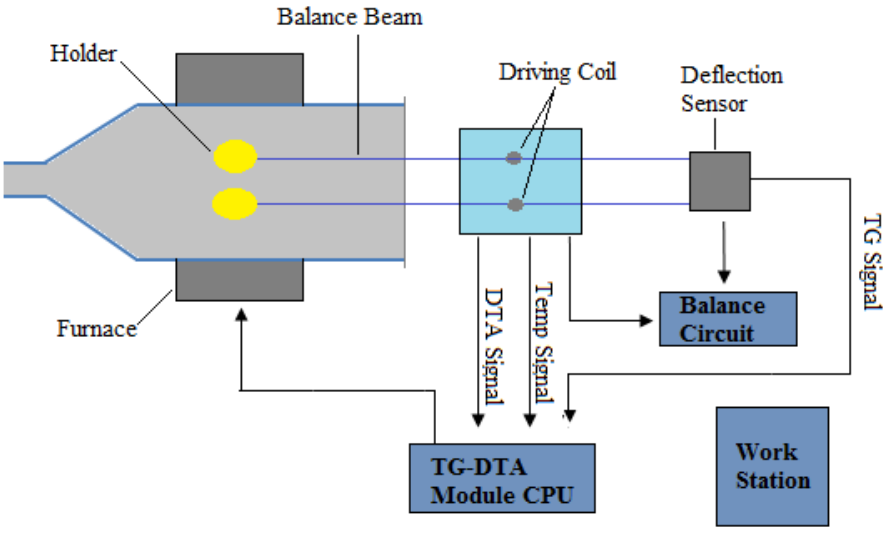


**Figure 2.7.** The schematic outline of TG-DTA instruments

### 2.2.6 UV Spectrophotometer

UV/Vis spectroscopy is used for the quantitative determination of different analytes that use monochromatic dispersion elements to vary the wavelengths. These instrument operates into the near-infrared region as well. Visible region 400-700 nm spectrophotometry is used extensively in colorimetry science. UV/Vis spectroscopic analysis refers to absorption spectroscopy or reflectance spectroscopy in the ultraviolet-visible spectral region [174].

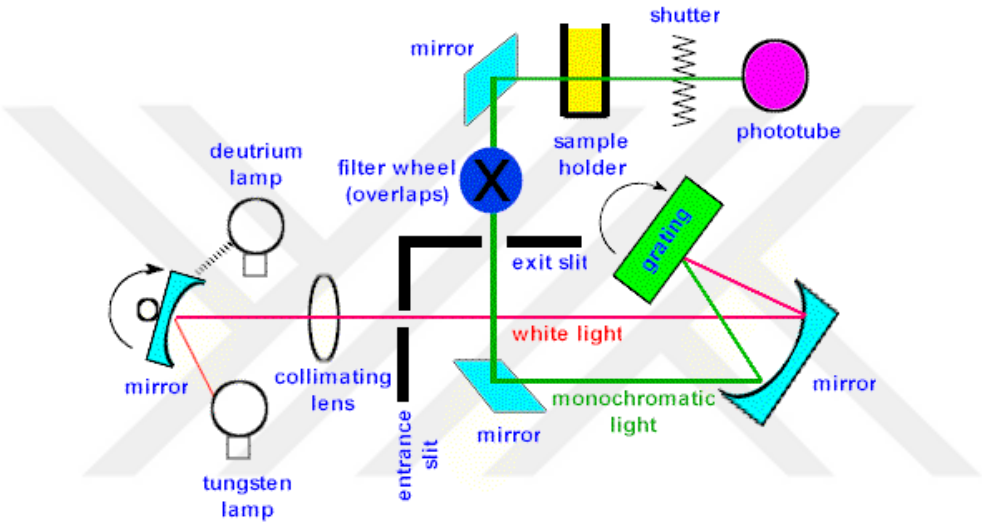


**Figure 2.8.** Single beam spectrophotometers [175].

The absorption or reflectance in the visible range directly affects the perceived color of the chemicals involved that is generally carried out in solutions but solids and gases can be studied as well. Scientists use spectrophotometer to measure the amount of compounds in a sample. The Beer-Lambert law states that the absorbance of a solution is directly proportional to the concentration of the absorbing species in the solution and the path length. If the compound is more concentrated more light will be absorbed by the sample. It measures the intensity of light passing through a sample and compares it to the intensity of light before it passes through the sample. The ratio $I/I_o$ is called the transmittance (%T), the absorbance (A) is based on the transmittance,

The Beer-Lambert law;

$$\mathbf{A = \log10(I/Io) = \varepsilon cL} \qquad \textbf{Eq. (2.2)}$$

where "*A*" is absorbance, "$I_o$" is the intensity of the incident light at a given wavelength, "*I*" is the transmitted intensity, *L* the path length through the sample, and *c* the concentration of the absorbing specimen, ε is a constant known as the molar absorptivity for each specimen and wavelength. According to the region of interest, samples are performed in cuvettes. They can be made of glass, plastic or quartz [174].

### 2.2.7 Atomic-force microscopy (AFM)

Atomic force microscopy (AFM) is a type of high resolution microscope which is capable of measuring images with a nanometer resolution that follows up the topography of samples by recording the interaction forces between the surface and a sharp tip mounted on a cantilever. AFM images are in the range of few nanometers for lateral resolution and less than 1 nm for vertical resolution. AFM produces images from the nonconductors without any special preparation as required in SEM and TEM. Also AFM gives direct to 3D images of surface structure of the samples. AFM was invented by Binnig *et al.* in 1986 and first commercially AFM was introduced in 1989 [176-178].

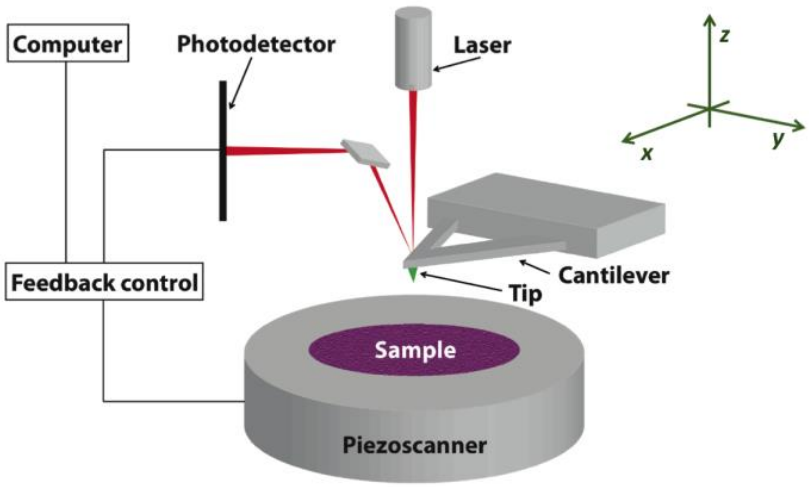


**Figure 2.9.** Schematic of Atomic Force Microscopy [176].

AFM is based on the principle that a tip, integrated to the end of the cantilever, is brought in the interatomic separation between the tip and sample. As the tip moves acros the surface, the interatomic potentials, force the cantilever to jump up and down with the changes in shapes of the surface. Consequently, topography of the images can be mapped out by measuring the deflection of the surface[176].

### 2.2.8 LCR Meter

LCR meter is a type of electronic test equipment used to measure the inductance (L), capacitance (C), and resistance (R) of an electronic component. Inductance (L) is the property of an electric conductor or circuit that causes an electromotive force to be generated by a change in the current flowing. Capacitance (C) is the ability of a system to store an electric charge. Resistance (R) is a measure of the difficulty to pass an electric current through that conductor. The capacitance can be increased by inserting a dielectric. If a dielectric material is inserted between the plates, the microscopic dipole moments of the material will shield the charges on the plates and alter the relation. Dielectric permittivity decreases with increase in the frequency and this phenomenon is called as dielectric relaxation or dielectric dispersion. The dielectric permittivity has two parts known as real and imaginary parts represented as **έ** and ε″, respectively. As imaginary part (ε″) of the permittivity represents the losses while energy being stored, real part (έ) of permittivity represents the energy stored in the nanomaterials and its capability to store energy.

A dielectric material behaves as insulator in between the plates of a parallel plate capacitor which could be polarized on the application of external electric field. Real part of permittivity can be represented as;

$$\acute{\varepsilon} = Cd / a \varepsilon_o \qquad \text{Eq. (2.3)}$$

where C is the capacitance of the pellet in farad, d the thickness of pellet in meter, A the cross-sectional area of the flat surface of the pellet and e0 the constant of permittivity of free space.

Dielectric losses are accurately similar to the friction losses in the mechanical movement. When the mobile charges align themselves on the application of AC electric field the resistance to this polarization is called dielectric losses and is associated with loss of

energy. The dielectric loss factor ($\varepsilon''$) is measured in terms of tangent loss factor ($\tan\delta$) defined by the relation ;

$$\varepsilon'' = \tan\delta \, . \, \acute{\varepsilon} \qquad \text{Eq. (2.4)}$$

The tangent of dielectric loss angle can be calculated using the relation

$$\tan \delta = 1 / 2\pi f R_s C_s \qquad \text{Eq. (2.5)}$$

where $\delta$ is the loss angle, $f$ is the frequency, $R_s$ is the equivalent series resistance and $C_s$ is the equivalent series capacitance [179,180] .

### 2.2.9 Vibrating Sample Magnetometer (VSM)

Vibrating sample magnetometer (VSM) is an instrument which is used to measure the change of the magnetic properties of materials with the applied magnetic field in terms of hysteresis loop. The VSM was first described by Foner [181]. The instrument displays the magnetic moment in e.m.u. units. Powders, solids, liquids, single crystals, and thin films are able to perform with a VSM. The VSM operation is easy like that magnetic sample is placed on a long rod and operated by a mechanical vibrator. The rod is positioned between the pole parts of an electromagnet on which detection coils have been mounted. The oscillatory motion of the magnetized sample will stimulate a voltage in the detection coils. The induced voltage is proportional to the sample's magnetization which can be varied by changing the magnetic field produced by the electromagnet [182].

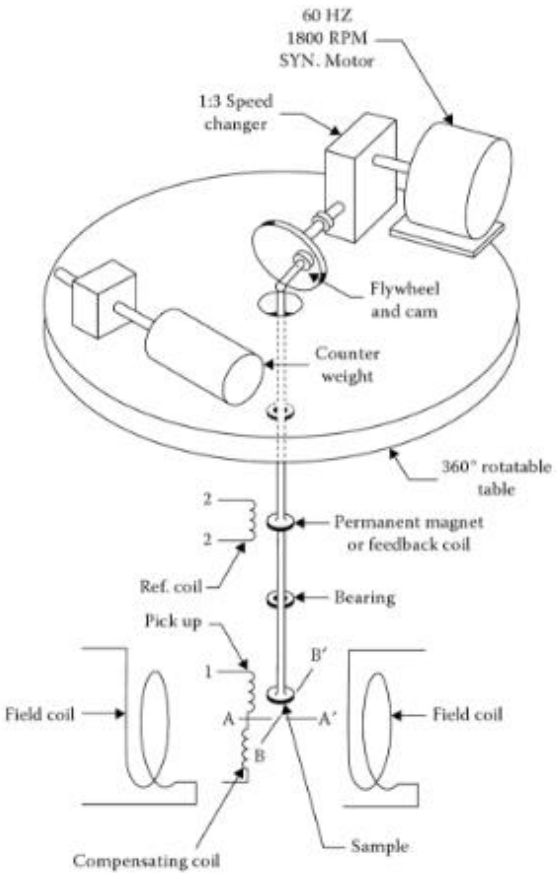


**Figure 2.10.** The schematic outline of VSM [183].

### 2.2.10 Fluorescence Spectrofotometer

Fluorescence spectrometer is a fast and simple instrument to determine the concentration of an analyte in solution based on its fluorescent properties [184].The sample is first excited by absorbing a photon from its ground electronic state to one of the various vibrational states in the excited electronic state. Collisions with molecules cause the excited molecule to lose vibrational energy until it reaches the lowest vibrational state of the excited electronic state. Then, the sample drops down to the ground electronic state and emitting a photon in the process. The emitted photons have different energies and frequencies. Therefore, in fluorescent spectroscopy, the different frequencies and relative intensities of emitted light, the structure of the different vibrational levels can be determined. The concentration of the analyte is directly proportional with the intensity of the emission [185].

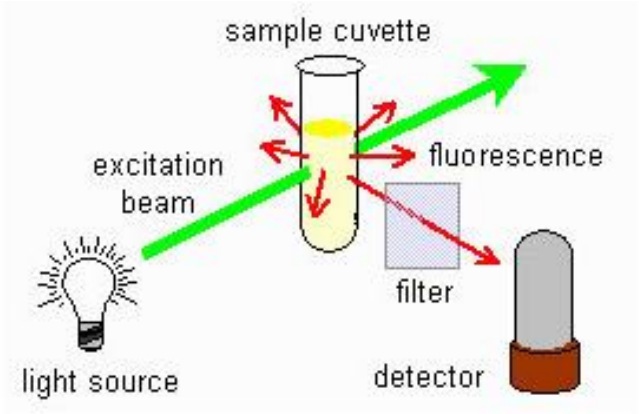


**Figure 2.11.** Scheme of fluorimeter

The **Figure 2.11** shows scheme of fluorimeter. The sample is located at the intersection of the two beam paths and the light source is in 90$^{o}$ angle with the detector [184].

### 2.2.11 Contact Angle Goniometer

Goniometer is an instrument that measures the contact angle. First commercial goniometer was designed by W.A. Zisman in the early 1960. The most widely used contact angle measurement technique is a direct measurement of the tangent angle at the three-phase contact point on a sessile drop profile. The contact angle is a quantitative measure of the wettability of the surface, represented by the angle at which a liquid or vapor interface makes with a solid surface. The angle is specific and determined by the interactions across the three interfaces. Wettability studies usually involve the measurement of contact angles as the primary data, which indicates the degree of wetting when a solid and liquid interact.Typically, the contact angle is illustrated by a drop of liquid on the surface. Contact angle values yield an important parameter, which quantifies the wetting characteristics of a solid material. Small contact angles ( 90°) correspond to high wettability, while large contact angles ( 90°) correspond to low wettability. **Figure 2.12.** shows quantitative measure of the wettability of the surface [187,188].

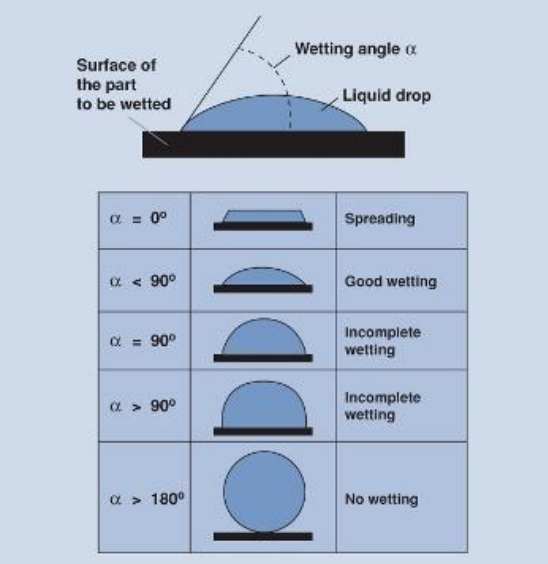


**Figure 2.12.** Contact angle range from 0º to 180º

## 2.3 Synthesis of Levan Phosphonate

For the production of phosphonated levan, 4 g of levan was be dissolved in 100 mL of pyridine by vigorously mixing on a magnetic stirrer for 48 hours at ambient conditions and then the solution was cooled down to 0 ºC in ice bath. 4 mL of $PCl_3$ was added slowly in a drop wise manner to the well-stirred solution at 0 ºC. After stirring for 30 min under ambient conditions, 100 mL of saturated $Na_2CO_3$ was added. The aqueous phase containing the modified polymer was separated and freed from pyridine and then subjected to dialysis using Spectra Por ®Dialysis Membrane cut of: 2 kDa against distilled water for at least four consecutive days with frequent exchanges of the solvent (3-5 times per day) [151]. Final samples are freeze dried and characterized by FT-IR, SEM- EDS and AFM.

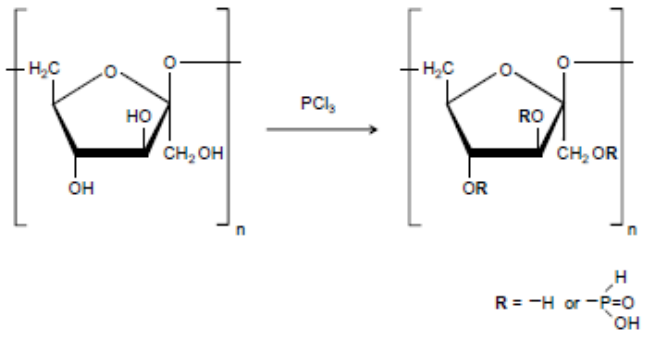


**Figure 2.13** Reaction scheme of phosphorylated levan

## 2.4. Synthesis of $CoFe_2O_4$ Nanoparticles

### 2.4.1 Temperature effect of $CoFe_2O_4$ Synthesis

Nano ferrites were synthesized by co-precipitation method. For this purpose, stoichiometric amounts of $Co(NO_3)_2.6H_2O$ and $Fe(NO_3)_3.9H_2O$ were dissolved in 100 mL deionized water seperately and then mixed together. While stirring the mixture, it was heated to 75$^o$C. At 75$^o$C, 100 mL of 1.5M NaOH solution was added for first sample. The stirring continued further for another 45 minutes at 75$^o$C to get narrow size distribution and chemically homogeneous ferrite particles. The pH was also maintained at around 12. Subsequently, precipitates were washed with distilled water, for removing salt. The products were dried in an electric oven and then sintered at 600$^o$C for 6 hours. For $2^{nd}$, $3^{rd}$, and $4^{th}$, samples, this process was performed at 80$^o$C, 85 $^o$C, and 90 $^o$C, respectively. The method is known to produce ferrite particles in nano range successfully [189]. The final products were characterized by using XRD, FT-IR, SEM-EDS, AFM, VSM, and LCR meter to determine for morphology, topography, crystal structure, particle sizes, elemental composition and magnetic properties.

### 2.4.2 pH Effect of $CoFe_2O_4$ Synthesis

To analyze the effect of pH, first, stoichiometric amounts of $Co(NO_3)_2$ $.6H_2O$ and $Fe(NO_3)_3$ $.9H_2O$ were dissolved in 100 mL deionized water seperately and then mixed together. While stirring the mixture, it was heated to 85$^o$C. At 85$^o$C, 12 mL of 1.5M NaOH solution was added for first sample. The stirring continued further for another 45 minutes at 85$^o$C to get narrow size distribution and chemically homogeneous of ferrite particles. The pH was also maintained around 6. Subsequently, precipitates were washed with distilled water for removing salt. The product was dried in an electric oven and then sintered at 600$^o$C for 6 hours. For $2^{nd}$ , $3^{rd}$ , and $4^{th}$ samples, this process was performed at 85 $^o$C, added 14mL, 16mL, and 18mL NaOH respectively. The end of process, pH of 1st, 2nd, 3rd, 4th samples were 6, 8, 10, and 12, respectively [189]. Finally, all products were characterized by using XRD, FT-IR, SEM-EDS, AFM, VSM and LCR Meter to determine for morphology, topography, crystal structure, particle sizes, elemental composition and magnetic properties.

### 2.4.3 Determination of Annealing Temperature of $CoFe_2O_4$

Annealing is heating a material above crystallization temperature, maintaining a suitable temperature and then cooling to ambient temperature which alters the physical and sometimes chemical properties of a material. Because crystal size is related to annealing factor, it is important to find out optimum annealing temperature range. TG-DTA analyses of $CoFe_2O_4$ nanoparticles were conducted to get optimum annealing temperature using Perkin Elmer Diamond TG-DTA anaylzer System. TG-DTA measurements were performed at a 10˚C heating rate from 25˚C to 900˚C under nitrogen atmosphere.

## 2.5 Attachment of Functioanal Groups

### 2.5.1 –COOH modification of $CoFe_2O_4$ Nanoparticle Surfaces

$CoFe_2O_4$ nanoparticles were synthesized according to our reported procedure. Successfully produced $CoFe_2O_4$ nanoparticles were dispersed in distilled water. For surface modification of nanoparticles, 0.23 gr $CoFe_2O_4$ was suspended in 30 ml $dH_2O$ for 30 minutes by using Labsonic M ultrasonic homogenizer and 0.23 gr N-phosphonomethyl iminodiacetic acid (PMIDA) was dissolved in 30mL $dH_2O$ at pH 10. Suspended $CoFe_2O_4$ and dissolved PMIDA were mixed with each other and then sonicated for 60 minutes at pH 8.2. Suspension was dried at 50 °C till all solvent was removed. Modified nanoparticles were seperated from excessive chemicals by using magnet. Modified nanoparticles were analyzed using FT-IR, UV and Floro spectrophotometer to determine funtional groups and floresance properties [190]. Reaction scheme is shown in **Figure 2.14**.

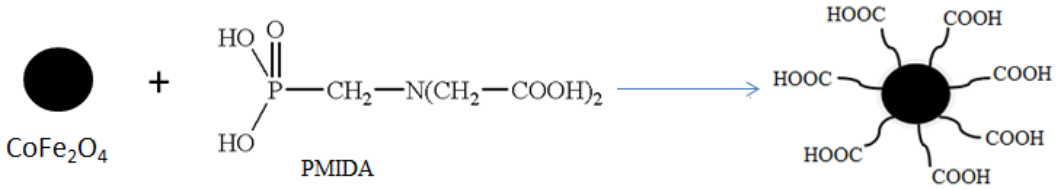


**Figure 2.14.** $CoFe_2O_4$–PMIDA nanoparticles

### 2.5.2 Activation of -COOH Modified $CoFe_2O_4$ Nanoparticles

PMIDA attached $CoFe_2O_4$ were suspended in deionized water by using sonicator. Sonicated nanoparticles in water were acidified with 1.5 M acetic acid and pH was maintained between at 4 and 5. $CoFe_2O_4$-PMIDA was activated by EDC and then the reaction mixture was stirred for 3–4 h. The EDC activated magnetic nanoparticles were washed a few times with $dH_2O$ in order to remove unreacted EDC. Activated nanoparticles were recovered by magnetic separation with magnet [190].

## 2.6. Conjugation of Folic Acid on Activated Magnetite Nanoparticles

For conjugation of Folic Acid on magnetite nanoparticles, 20 mg of a EDC activated magnetic nanoparticles were treated with 4 mg Folic Acid in 20 ml $dH_2O$ and the resulting solution was stirred overnight at room temperature. After overnight, Folic acid tagged magnetic nanoparticles were centrifuged and precipitated, washed few times with $dH_2O$ [190]. Washed precipitates were freeze-dried for further process. Modified nanoparticles were analyzed for functional groups present by FT-IR . Reaction scheme is shown in **Figure 2.15.**

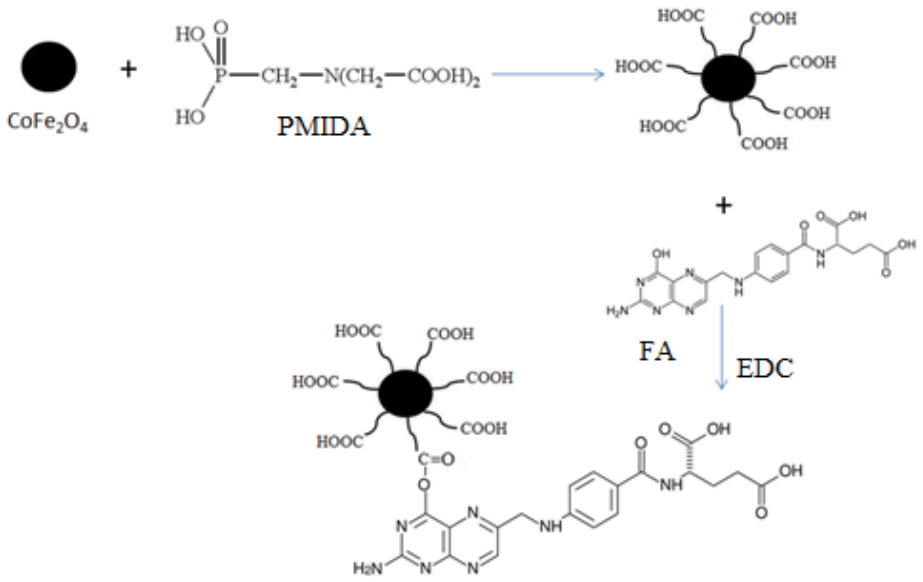


**Figure 2.15.** Synthesis of nanoparticles $CoFe_2O_4$-PMIDA-FA

## 2.7 Encapsulation of $CoFe_2O_4$- Folic Acid

Organic and aqueous solutions were formed for encapsulation of nanoparticles. 100 mg CTAB was dissolved in 100 mL chloroform and stirred with mechanical stirrer vigorously. And then, aqueous solution was formed as follows; 100mg Levan Phosphonate and 100mg $CoFe_2O_4$ - Folic Acid were dispersed in 100 mL $dH_2O$ and this suspension was added into the organic phase dropwise while organic phase was stirring vigorously. Black samples were formed at organic-aqueous interface at the two phase equilibrium. These black samples were the encapsulated nanoparticles that were separated from organic and aqueous phases. At last, Separated samples were freeze-dried and chacterized by using FT-IR, TEM, SEM.

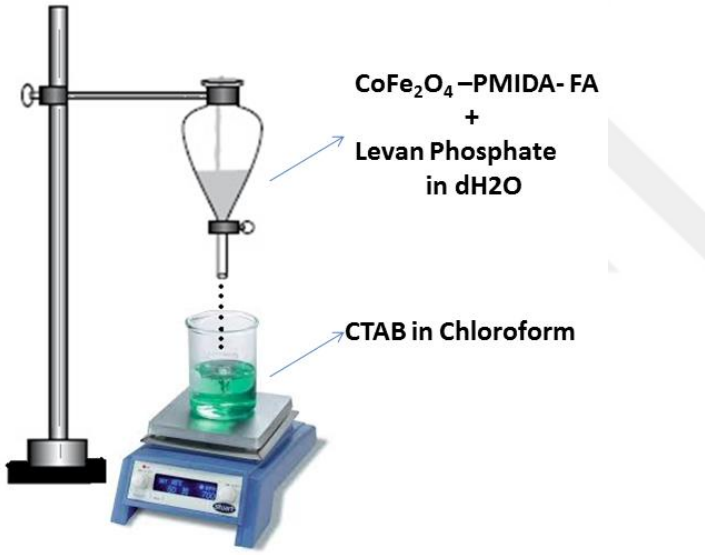


**Figure 2.16.** Encapsulation of nanoparticles $CoFe_2O_4$-PMIDA-FA

# 3. RESULTS AND DISCUSSION

## 3.1. Characterization of Levan phosphonate

### 3.1.1. FT-IR comparison between Levan and Levan Phosphonate

Levan has industrial importance, which proposes a variety of industrial applications in the fields of pharmaceuticals, cosmetics and foods. Modified levan can be a useful material for biomedical industry, as well as being too many application areas as a pure material. The FT-IR spectrum (**Figure 3.1**) showed that several stretching vibration bands were detected: the hydroxyl (OH) stretching vibration bands around 3200 $cm^{-1}$, two bands around 2900 $cm^{-1}$ - 2930 $cm^{-1}$ corresponding to carbon-hydrogen (C-H) stretching vibration of fructose residues, bands in the region of 1430 $cm^{-1}$ that were assigned to C-H plan deformation vibration combined with aromatic skeletal vibrations, bands at 1120 $cm^{-1}$ and 1000 $cm^{-1}$ that were dominated by the stretching vibrations of the glycosidic linkage contributions of C-O-C and C-O-H, as well as the 920 $cm^{-1}$ band resulting from the stretching vibration of pyran ring. These bands are all characteristic of levan polysaccharides reported earlier [191]. By comparison, in the FT-IR spectrum of Ph-levan, more bands could be identified: a band at 2360 $cm^{-1}$ corresponding to the P–H bond, another one at 1200 - 1100 $cm^{-1}$ corresponding to the P=O bond, a shoulder at 1045 $cm^{-1}$ attributable to the P–OH bond and bands around 875 $cm^{-1}$ corresponding to the P–O–C bonds [192-194]. The bands respective to phosphate groups are highlighted with grey background in which augmented spectra is between 700 and 1000 $cm^{-1}$.

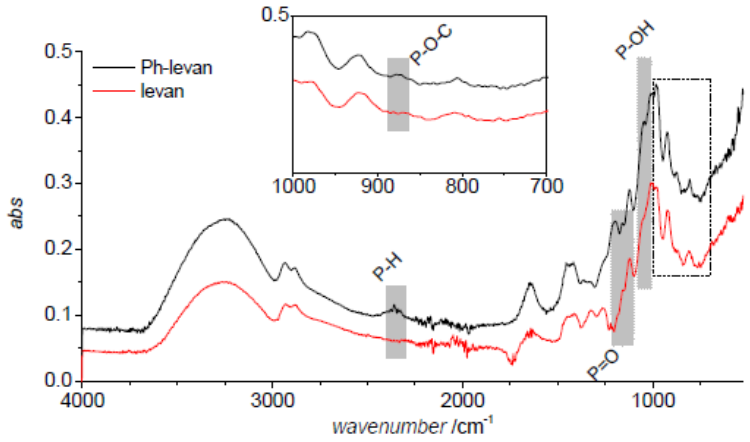


**Figure 3.1** FT-IR spectra of levan samples (red line) and phosphonated levan (black line).

### 3.1.2. EDS results of Levan-phosphonate

EDS was performed to check elemental composition for further evaluate the efficiency of the modification . **Table 3.1** showed atomic ratio of levan phosphonate. A peak of phosphorus was detected in **Fig. 3.2** and the EDS analysis resulted in an atomic ratio of C:O:P = 41:55:4. Costa et all. also reported that synthesized levan phosphonate EDS analyses was 44:51:3 [151]. Elementel ratio are different from each other. These difference may be caused from reaction conditions, chosen analyses area or using different instrument . Because levan is a microbial biopolymer and it is difficult to control its molecular weight and branching parameters. Hence, FT-IR and EDS results both showed that phosphonate modification of levan was achieved.

Fitting Coefficient : 0.8899

| Element | (keV) | Mass% | Error% | Atom% | K |
|---|---|---|---|---|---|
| C K | 0.277 | 32.96 | 1.70 | 41.03 | 16.0652 |
| O K | 0.525 | 58.92 | 4.15 | 55.05 | 68.8509 |
| P K | 2.013 | 8.12 | 1.80 | 3.92 | 15.0839 |
| Total | | 100.00 | 100.00 | | |

**Table 3.1.** Atomic ratio of levan phosphonate

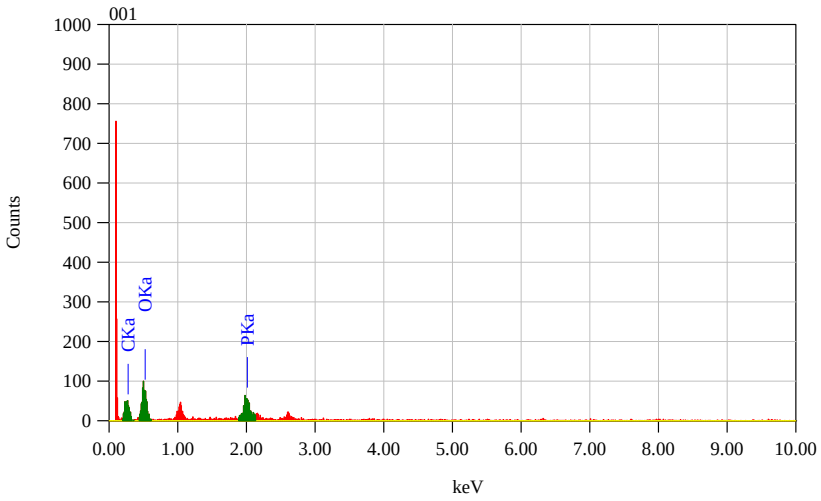


**Figure. 3.2.** ZAF Method Standardless Quantitative Analysis

### 3.1.3. AFM and Contact Angle Analyses of Levan- phosphonate

Nanoparticles have unique properties that are directly correlated to their size, shape and size distribution. AFM has been broadly applied to material surface inspections including topography survey, roughness analysis and structural research. AFM imaging was measured by JEOL, JSPM-5200 microscope at room temperature. Samples were made suspension with $dH_2O$. Two drops of the suspended sample solutions was immediately spread on 10 x 10 mm glass slide`s surfaces. The sample was then allowed to dry under the 250 watt bulb for 15 minutes. AFM measures the nanometer-scale topography of surfaces through direct contact between a sample surface and a probe tip mounted on the end of a cantilever microbeam. The cantilever peak frequency was 183.798 kHz and the image resolution was 512 x 512 pixels. AFM image of the levan phosphonate is shown in **Figure 3.3**. The measured surface roughness is represented by two-dimensional (A) and three-dimensional images (B). The detailed roughness parameters of the below mention films are summarized in **Table 3.2**.

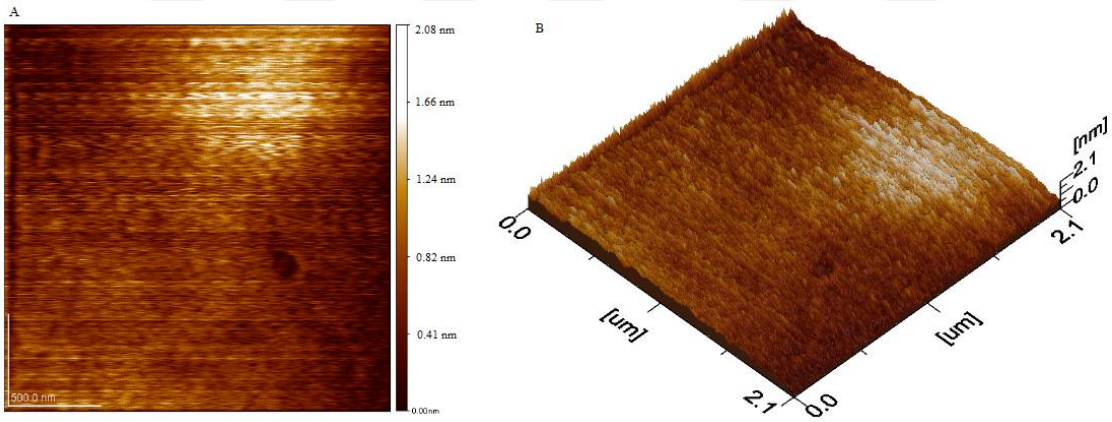


**Figure 3.3.** AFM image Levan Phosphonate

Rq parameter (The root-mean-square roughness) and average roughness ($R_a$) of thin film surface are important parameters to evaluate the topography of surface features. Paramaters from **Table 3.2** and 3D images showed that levan phosphonate films roughness biopolymer. The morphology of levan phosphonate is quite similar with levan thin films obtained by MAPLE exhibiting a spatial orientation [195]. Changes of surface roughness and

chemical composition can effect the values of contact angle and as a result also wettability. Determination of wettability is based on the measurement of the material surface contact angle. Static water contact angle was measured by sessile drop analysis (DSA 10, KRÜSS gmBH) to investigate the wettabilities of the film samples. To get film samples, LPh was dissolved in the solvent. Homogen LPh solutions was dropped on the clean polished surface. As the solvent evaporated thin film LPh was obtained. A drop of water was placed by a microsyringe on the surface of the dry levan phosphonate and its image was captured by a video camera. 3 measurements were taken for each sample. Small contact angles (less than 90°) correspond to high wettability, while large contact angles (equal or larger than 90°) correspond to low wettability [187]. Levan phosphonate contact angle image was shown in **Figure 3.4**. It is shown that levan phosphonate's contact angle is 60° which is smaller than 90° corresponding to high wettability

| Image information | |
|---|---|
| Ra = 0.251 nm | Rq = 0.316 nm |
| Rzjis = 1.99 nm | Rz = 2.06 nm |
| S = 4.38 $um^2$ | S ratio = 1.00 |

**Table 3.2** Roughness parameters of levan phosphonate

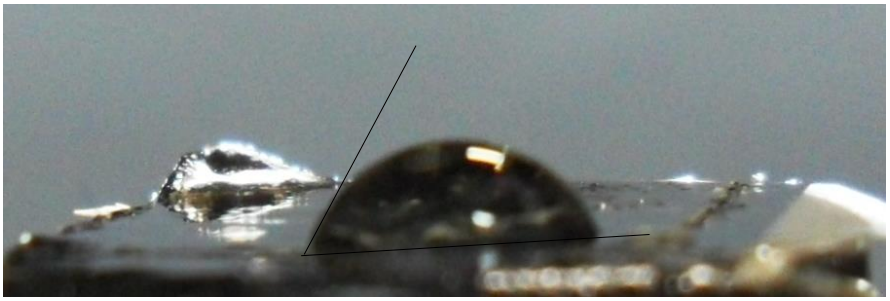

**Figure 3.4.** Contact Angle of Levan Phosphonate

## 3.2. Characterization of $CoFe_2O_4$

### 3.2.1. Characterization of Temperature Effect

#### 3.2.1.1. Structural analyses by FT-IR and XRD

FT-IR spectra of the samples were recorded on a FT-IR, Perkin Elmer 100 series spectroscopy measurements were conducted between 350 and 4000 $cm^{-1}$. The samples were prepared by compaction of small amount of nano composite powder with KBr powder in a hydraulic press that analyzed for functional groups present.

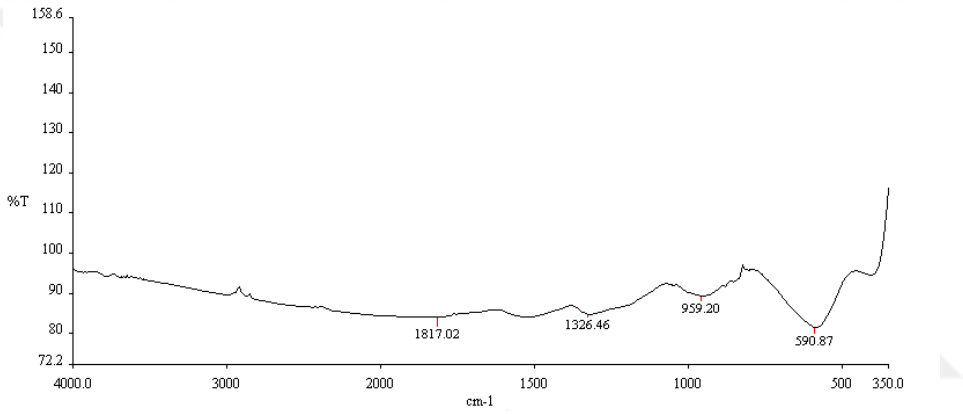


**Figure 3.5.** $CoFe_2O_4$ nanoparticles synthesized at 85 $^oC$ at pH12

According to the geometrical configuration of the oxygen nearest neighbors, the metal ions are usually situated in two different sublattices in ferrites, designated as the tetrahedral and octahedral sites [196]. Two main broad metal–oxygen bands are seen in the FT-IR spectra of studied pattern that are 590 $cm^{-1}$ large band and 400 $cm^{-1}$ bands. These two bands attributed the band around 590 $cm^{-1}$ to the intrinsic vibration of tetrahedral metal–oxygen complexes and the band around 400 $cm^{-1}$ to the intrinsic vibration of octahedral metal–oxygen complexes. The 590 $cm^{-1}$ band is high frequency that is caused by stretching vibrations of tetrahedral metal–oxygen band and 400 $cm^{-1}$ band is low frequency absorption band that is caused by the metal–oxygen vibrations in octahedral sites [197]. The difference in frequencies of high and low frequency bands is due to changes in the bond length $Fe^{3+}$ – $O^{2-}$ at tetrahedral and octahedral sites [198]. Gabal et al. also reported that two characteristic ferrite bands appeared in 400 $cm^{-1}$ and 590 $cm^{-1}$ [199].

The XRD patterns were taken using CuKα (λ= 1.5406A˚) radiation in 2θ range 20–80˚ at room temperature. Chemical co-precipitation seems to be convenient for the synthesis of nanoparticles because of its simplicity and better control over crystallite size and other properties of the materials. **Figure 3.6** shows the XRD peaks of Cobalt Ferrites. XRD patterns of $CoFe_2O_4$ nanocrystals show the specific crystallographic plane of $CoFe_2O_4$, (220), (311), (400), (422), (511), (440). The crystalline sizes were calculated using Scherrer formula considering the most intense peak (3 1 1) [200]. Analysis of the diffraction pattern of all the samples confirmed the formation of spinel cubic structure. Crystallographic planes of SE80 and SE85 patterns are noisier than SE75 and SE90. The values of crystallite size are tabulated in **Table 3.3** which shows average crystal size of $CoFe_2O_4$ and SE75, SE80, SE85, SE90 are corresponding to synthesized nanoparticles at 75ºC, 80ºC, 85ºC, 90ºC, respectively. All the samples were prepared under identical conditions, the crystallite size varied with reaction temperature. The above observation tells us that crystal size was 20nm at 75 ºC. Increased process temperature made crystal size 13 nm with 5ºC temperature difference. So, Crystal size was 11 nm at 85 ºC. At 90 ºC, its crystal size again increased that was 18nm. As a result, the crystal size growth of the particles is affected by the reaction temperature. Prabhakaran et al. also show that the reaction temperature plays a critical role in controlling the rate of nucleation. But, they are reported crystallite size were calculated by using the Rietveld method and sizes are increased with increasing temperature unlike our results [201]. The crystalline sizes were calculated and SE85 was chosen as the optimum process conditions for $CoFe_2O_4$ synthesis for XRD results.

| Sample Name | Process Temperature | Average Crystal Size (nm) |
|---|---|---|
| SE75 | 75 ºC | 20 nm |
| SE80 | 80 ºC | 13 nm |
| SE85 | 85 ºC | 11nm |
| SE90 | 90 ºC | 18 nm |

**Table 3.3.** Average Crystal Size of $CoFe_2O_4$ at varied temperatures at pH12.

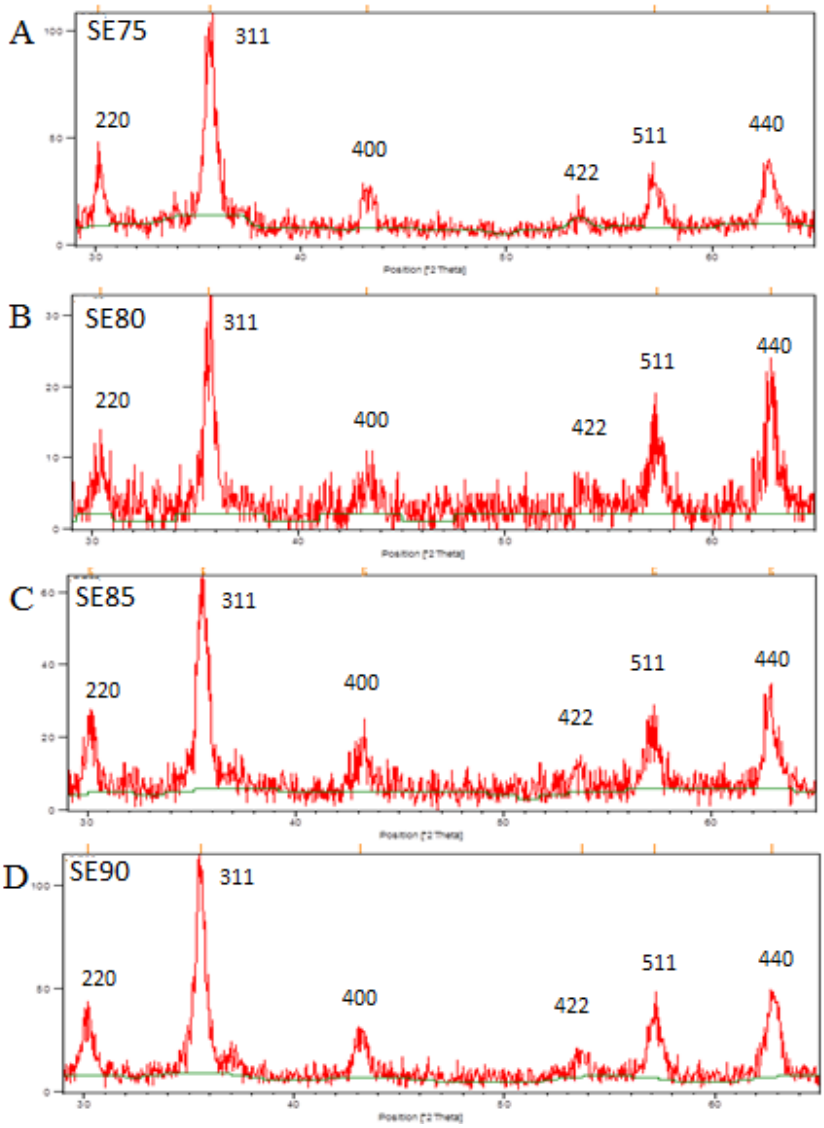


**Figure 3.6** XRD peaks of $CoFe_2O_4$ synthesized at varied temperature.

### 3.2.1.2. AFM Analyses

Metal nanoparticles properties are directly correlated to their size, shape and size distribution. Atomic Force Microscopy has been widely applied to particle size determination and surface roughness analysis. AFM imaging was measured by JEOL, JSPM-5200 microscope at room temperature. Samples were made suspension with ethanol. Two drops of the suspended sample solutions were immediately spread on 10 x 10 mm glass slide`s surfaces. The sample was then allowed to dry under the 250 watt bulb for 15 minutes. AFM measures the nanometer-scale topography of surfaces through direct contact between a sample surface and a probe tip mounted on the end of a cantilever microbeam. The cantilever peak frequency was 169.544 kHz and the image resolution was 256 x 256 pixels.

All the samples were prepared under identical conditions except process temperature. **Figure 3.7** shows the topography of $CoFe_2O_4$ at varied temperature. The information about the surface microstructure of the cobalt ferrite is obtained from the three dimensional (3D) AFM images and histograms. It can be seen from the figure and histogram that particles are spherical with average size less than 30 nm. Spherical nanoparticles were also confirmed by using AFM image by Srivastava et al.[202]. This images show that the samples under investigation have uniform morphology and nanoparticule size is around 20nm, 10nm, 3nm, 8nm for reaction temperature at 75$^{o}$C, 80$^{o}$C, 85$^{o}$C, 90$^{o}$C, respectively. AFM results have in good agreement with XRD data within experimental errors. As a result, AFM images showed that SE85 was optimum process conditions for $CoFe_2O_4$ synthesis.

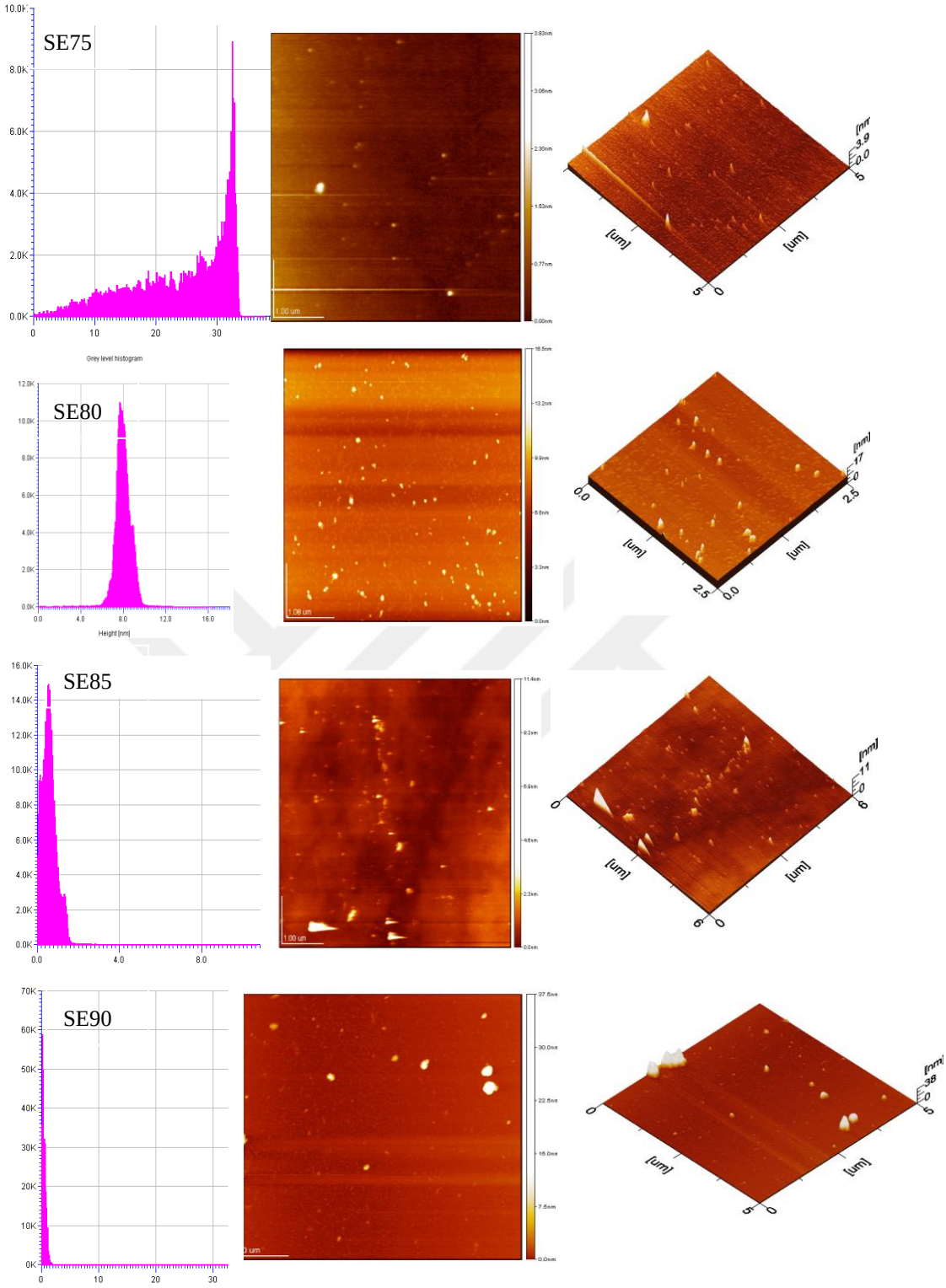


**Figure 3.7** Topography of $CoFe_2O_4$ synthesized at varied temperature

### 3.2.1.3. SEM – EDS Analyses

The morphology and the particle size of the samples, prepared by co-precipitation technique, influence the morphologic structure and elemental ratio properties of the materials that were determined by scanning electron microscopy (SEM). SEM analysis was performed on a JEOL Model JSM6490A using secondary electrons at 20kV with X50k and X100k magnificence to investigate the homogenity, morphology and the particle size of nanoparticles. Samples were made suspension with ethanol. Two drops of the suspended sample solutions was immediately spread on 10*10 mm glass slide`s surfaces. The sample was then allowed to dry under the 250 watt bulb for 15 minutes. The last step, slides were prepared by sputter coating with gold to ~$5\times10^{-6}$ cm in thickness using SC7640 sputter coater (QuorumTechnologies, Newhaven, UK) under high vacuum, 0.1 Torr, 1.2 kV, and 50mA at 25ºC. **Figure 3.8** shows morphology of $CoFe_2O_4$ prepared under identical conditions except reaction temperature . All figures indicate that the nano-sized $CoFe_2O_4$ are spherical in shape. At the same time, SE75, SE80, SE85 exhibited homogeneous distribution, while SE90 exhibited particle agglomeration. The values of particle size are tabulated in **Table 3.4.** Nanoparticules size of $CoFe_2O_4$ are around 16nm, 17nm, 20nm, 21nm for process temperature at 75ºC, 80ºC, 85ºC, 90ºC, respectively. R. Safi et al. also reported $CoFe_2O_4$ nanoparticles show spherical, homogeneous distribution and average particle sizes are approximately within the range of 34–40 nm [203] .

| Sample Name | Process Temperature (ºC) | Average Particle Size |
|---|---|---|
| **SE75** | 75 ºC | 16 nm |
| **SE80** | 80 ºC | 17 nm |
| **SE85** | 85 ºC | 20 nm |
| **SE90** | 90 ºC | 21 nm |

**Table 3.4.** Average particle size of $CoFe_2O_4$ at varied temperatures

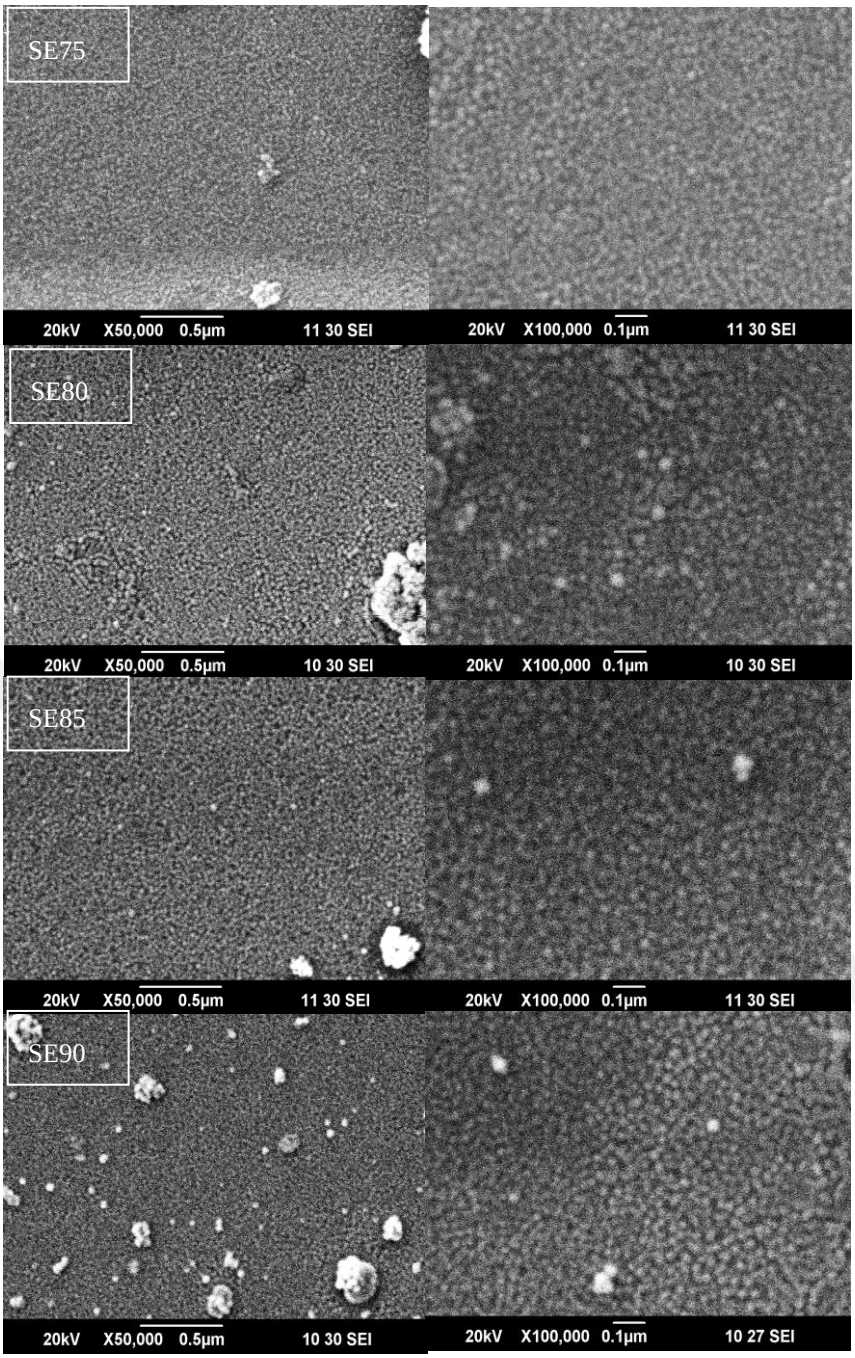


**Figure 3.8** Morphology of $CoFe_2O_4$ synthesized varied temperature at pH12

Elemental analysis of the $CoFe_2O_4$ materials synthesized varied process temperature was estimated by Energy Dispersive Spectroskopy (EDS). EDS analysis was performed on a JEOL Model JSM6490A using secondary electrons at 20kV with 50X magnification to investigate the quantitative ratio of elements. The values of atomic ratio are tabulated in **Table 3.5.** The EDS analysis resulted in atomic ratio of Co:Fe:O = 13:24:63 for SE75; Co:Fe:O = 14:28:58 for SE80; Co:Fe:O = 13:24:63 for SE85; Co:Fe:O = 16:29:55 for SE90. Elementel ratios are almost same with each other. These small differences may be caused

from fitting coefficient of samples. Hence, EDS results showed that $CoFe_2O_4$ nanoparticles synthesized varied temperature were achieved. R. Safi et al. also reported that the EDS spectra of the synthesized $CoFe_2O_4$ ferrite nanoparticles results proved the existence of the main elements in all samples whose Co:Fe:O atomic ratio is 12:19:69 [203] .

| **Element** | **SE75** Fitting Coefficient : 0.6942 | | **SE80** Fitting Coefficient : 0.6981 | | **SE85** Fitting Coefficient : 0.7161 | | **SE90** Fitting Coefficient: 0.6883 | |
|---|---|---|---|---|---|---|---|---|
| | Mass % | Atom% | Mass % | Atom% | Mass % | Atom% | Mass % | Atom% |
| **O** | 31.89 | 62.49 | 27.49 | 57.42 | 32.04 | 62.66 | 25.54 | 54.97 |
| **Fe** | 43.56 | 24.45 | 47.03 | 28.13 | 43.05 | 24.12 | 47.16 | 29.08 |
| **Co** | 24.55 | 13.06 | 25.48 | 14.45 | 24.91 | 13.22 | 27.3 | 15.95 |

**Table 3.5** Quantitative Analysis of $CoFe_2O_4$

### 3.2.1.4. Dielectric Permittivity and Dielectric Losses

The dielectric constant, dielectric loss and tangent loss factor for all the cobalt ferrites nanoparticles have been studied as a function of frequency in the range 100 Hz to 5 MHz at room temperature using Wayne Kerr 6500B LCR Meter Bridge. The room temperature dielectric constant as a function of frequency from 100 Hz to 5 MHz for Co ferrite nanoparticles synthesized at different temperature is shown in **Figure. 3.9** that was determined using **Eq. (2.3).** The dielectric constant has lowest value at 75$^{o}$C while the highest value is at 80 $^{o}$C. The dielectric constant performed at 90 $^{o}$C, is lower than at 85 $^{o}$C. Dielectric constant highly depends on frequency that decreases with increase of frequency for every samples which is a characteristic behaviour of most of the ferrite materials [208].

At 5MHz frequency it is very small and becomes independent of frequency. The change in the dielectric constant of ferrites is mostly attributed to the variations in the concentration of $Fe^{2+}$ [204]. A dielectric material consists of two different layers in which the well conducting grains are separated by poorly conducting grain boundaries. The high value of dielectric constant at lower frequency emerges from the grain boundaries since grain boundaries are dominant at lower frequency region whereas the grains are dominant at high frequency region [205]. The observed variation in dielectric constant may be understood on the basis of space charge polarization. The space-charge polarization occurs due to the diffusion of ions, along the external field direction, so it is giving rise to redistribution of charges in the dielectric substances. The subsequent charge build-up at the insulating grain boundary is a major contributor to the dielectric constant in ferrites. Hence, the more $Fe^{2+}$ ions in the ferrite the more, space charge polarization expected due to the ease of electron transfer between 2+ and 3+ charged ions. Thus, the dielectric constant is expected to decrease with the higher reaction temperature effect as a result of the space charge polarization [206]. Manikandan et al. are also reported that has a same result with earlier observations of other researchers about ferrites [204].

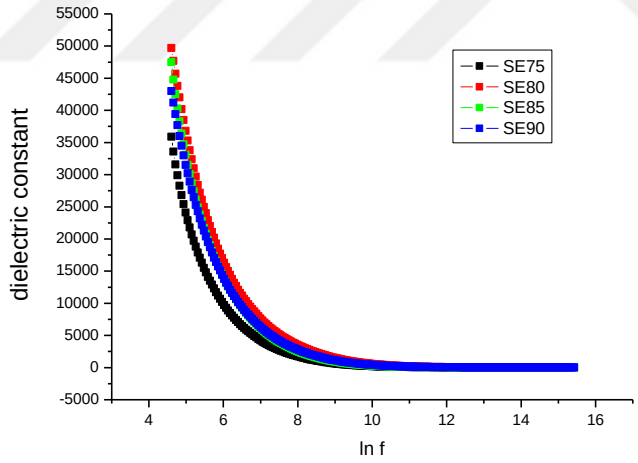


**Figure 3.9** Variation of dielectric constant with ln f of $CoFe_2O_4$ nanoparticles at room temperature.

Dielectric loss is an important part of the total core loss in ferrite nanoparticles. The low dielectric losses are desirable for low core loss. The room temperature dielectric loss as a function of frequency from 100 Hz to 5 MHz for Co ferrite nanoparticles synthesized at different temperature is shown in **Figure. 3.10** that was determined using **Eq. (2.4)**. The dielectric loss profiles are similar to dielectric constant. The increase in hoping electrons

result in a local displacement in the direction of the extent electric field that causing an increase in electric polarization enhances dielectric loss. Hudson [207] shows that the dielectric losses in ferrite is reflected in the conductivity measurements where the materials of high conductivity exhibiting high losses [212].

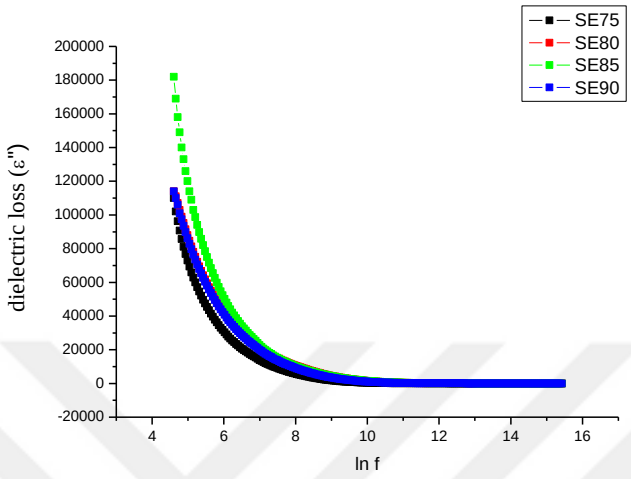


**Figure 3.10** Variation of dielectric loss with lnf of $CoFe_2O_4$ nanoparticles

### 3.2.2. Characterization of pH Effect

#### 3.2.2.1. Structural analyses by FT-IR and XRD

FT-IR spectra of the samples were recorded on a FT-IR, Perkin Elmer 100 series spectroscopy measurements were conducted between 350 and 4000 $cm^{-1}$. The samples were prepared by compaction of small amount of nano composite powder with KBr powder in a hydraulic press and pellets were made which were analyzed for functional groups present.

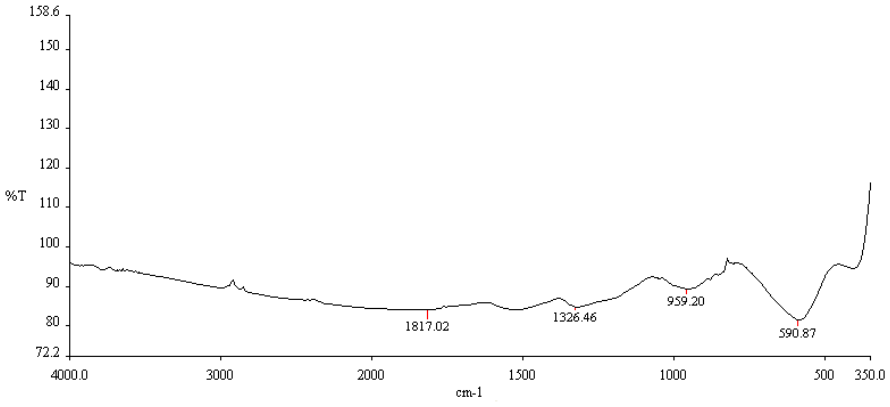


**Figure 3.11.** $CoFe_2O_4$ nanoparticles synthesized at 85 $^oC$

The XRD patterns were taken using CuKα (λ= 1.5406A˚) radiation in 2θ range 20–80˚ at room temperature. **Figure 3.12** shows the XRD peaks of cobalt ferrites. XRD patterns of $CoFe_2O_4$ nanocrystal shows the specific crystallographic plane of $CoFe_2O_4$ , (220), (311), (400), (422), (511), (440). The crystalline sizes were calculated using Scherrer formula considering the most intense peak (3 1 1) [200]. Prabhakaran et al. also reported same results that all samples can be indexed as the single-phase cubic spinel structure and no additional phase was detected [201]. The noisy of crystallographic plane of samples are getting decrease with increasing pH. As a result, analysis of the diffraction pattern of all the samples confirmed the formation of spinel cubic structure. Chemical co-precipitation seems to be convenient for the synthesis of nanoparticles because of its simplicity and better control over crystallite size and other properties of the materials. All the samples were prepared under identical conditions, the crystallite size varied with increased pH. The values of crystallite size are also tabulated in **Table 3.6** . Average crystal size of $CoFe_2O_4$ are 14, 10, 14, 13 for at pH 6, pH 8, pH 10, pH 12, respectively. **Figure 3.12** show that sample PH12 has sharp crystal peak as compared other pH values. Crystal size of nanoparticles samples around 13-14 nm. As a result, the crystal size and crystal structure of the particles is affected by the pH difference. K. Praveena et al. reported that the reaction pH plays a critical role for synthesizing nanoparticles. But, they reported that crystallite sizes are increased with increasing pH value unlike our results [209]. In crystalline materials atoms are periodically arranged but in amorphous materials atoms are randomly arranged. Diffraction pattern with sharp peaks are related to crystalline nanoparticles. Hence, sample pH12 has sharper peak and smaller crystal size compared to other pH values that is optimum process conditions for nano size $CoFe_2O_4$ synthesis.

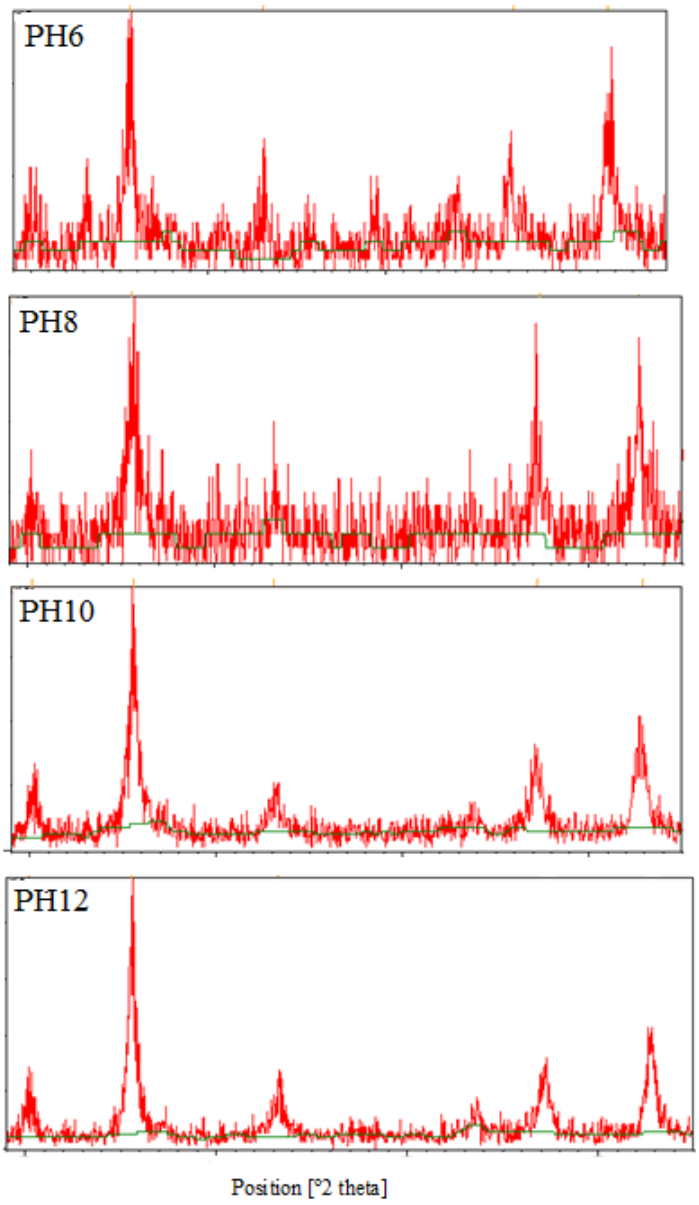


**Figure 3.12** XRD peaks of $CoFe_2O_4$ synthesized at varied pH at 85°C

| Sample Name | pH (aproximately) | Average Crystal Size |
|---|---|---|
| PH6 | 6 | 14 nm |
| PH8 | 8 | 10 nm |
| PH10 | 10 | 14 nm |
| PH12 | 12 | 13 nm |

**Table 3.6** Average Crystal Size of $CoFe_2O_4$ for varied pH at 85°C

### 3.2.2.2. AFM Analyses

AFM measures the nanometer-scale topography of surfaces through direct contact between a sample surface and a probe tip mounted on the end of a cantilever microbeam. The cantilever peak frequency was 169.544 kHz and the image resolution was 256 x 256 pixels. Although, all the samples were prepared under identical conditions except pH parameter. **Figure 3.13** shows that topography of $CoFe_2O_4$ at at varied pH. Metal nanoparticles properties directly correlate to their size, shape and size distribution. Atomic Force Microscopy has been widely applied to particle size determination and surface roughness analysis. AFM imaging was measured by JEOL, JSPM-5200 microscope at room temperature. Samples were made suspension with ethanol. Two drops of the suspended sample solutions was immediately spread on 10 x 10 mm glass slide`s surfaces. The sample was then allowed to dry under the 250 watt bulb for 15 minutes. Complimentary information about the surface nanostructure of the cobalt ferrite is obtained from the 2D dimensional, 3D dimensional AFM images and histograms. It can be seen from the figure and histogram that particles are spherical with average size less than 10 nm. These images show that the samples under investigation have uniform morphology and nanoparticule size is around 8 nm, 8 nm, 5 nm, 2 nm at pH6, pH8, pH10, and pH12, respectively. Jagminas A. et al. also reported that the nanoparticles made in all investigated solutions are spherical and usually ultra small [210]. As a result, all AFM images and histograms showed homogen dispersion and spherical nanoparticles. The higher pH value samples, the easier and rapidly separation from supernatant. pH 12 sample has smaller particle size compared to other pH values that can be regarded as optimum process conditions for $CoFe_2O_4$ synthesis.

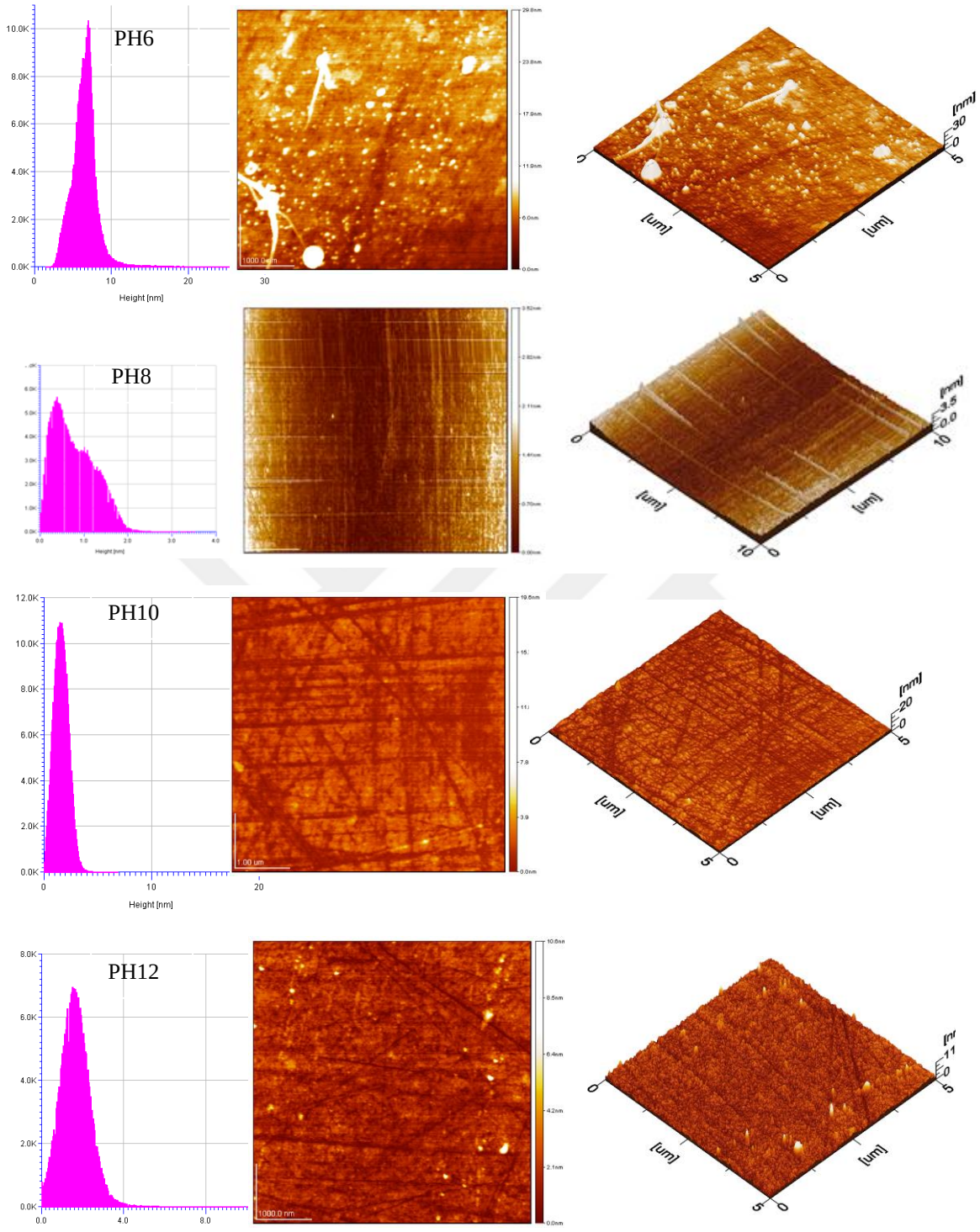


**Figure 3.13** Topography and histograms of $CoFe_2O_4$ synthesized at varied pH.

### 3.2.2.3. SEM-EDS analyses

All samples were synthesized under identical conditions except pH parameter by using co-precipitation method. All samples were made suspension with ethanol. Two drops of the suspended sample solutions was immediately spread on 10*10 mm glass slide`s surfaces. The sample was then allowed to dry under the 250 watt bulb for 15 minutes. The last step, slides were prepared by sputter coating with gold to ~$5\times10^{-6}$ cm in thickness using SC7640 sputter coater (QuorumTechnologies, Newhaven, UK) under high vacuum, 0.1 Torr, 1.2 kV, and 50mA at 25$^{o}$C. SEM analysis was performed on a JEOL Model JSM6490A using secondary electrons at 20kV with 50000X and 100000X magnification to investigate the homogenity, morphology and the particle size of nanoparticles which **Figure 3.14** shows morphology of $CoFe_2O_4$ nanoparticles at varied pH. All figures indicate that the nano-sized $CoFe_2O_4$ are spherical in shape and homogeneous distribution. The values of particle size are tabulated in **Table 3.7.** Nanoparticules size of $CoFe_2O_4$ are around 17nm, 17nm, 18nm, 19nm for pH 6, pH 8, pH 10, pH 12, respectively. R. Safi et al. also reported $CoFe_2O_4$ nanoparticles show spherical, homogeneous distribution at pH 12 [203].

| Sample Name | pH (approximately) | Average Particle Size |
|---|---|---|
| **PH6** | 6 | 17nm |
| **PH8** | 8 | 17 nm |
| **PH10** | 10 | 18 nm |
| **PH12** | 12 | 19 nm |

**Table 3.7.** Average particle size of $CoFe_2O_4$ for varied pH

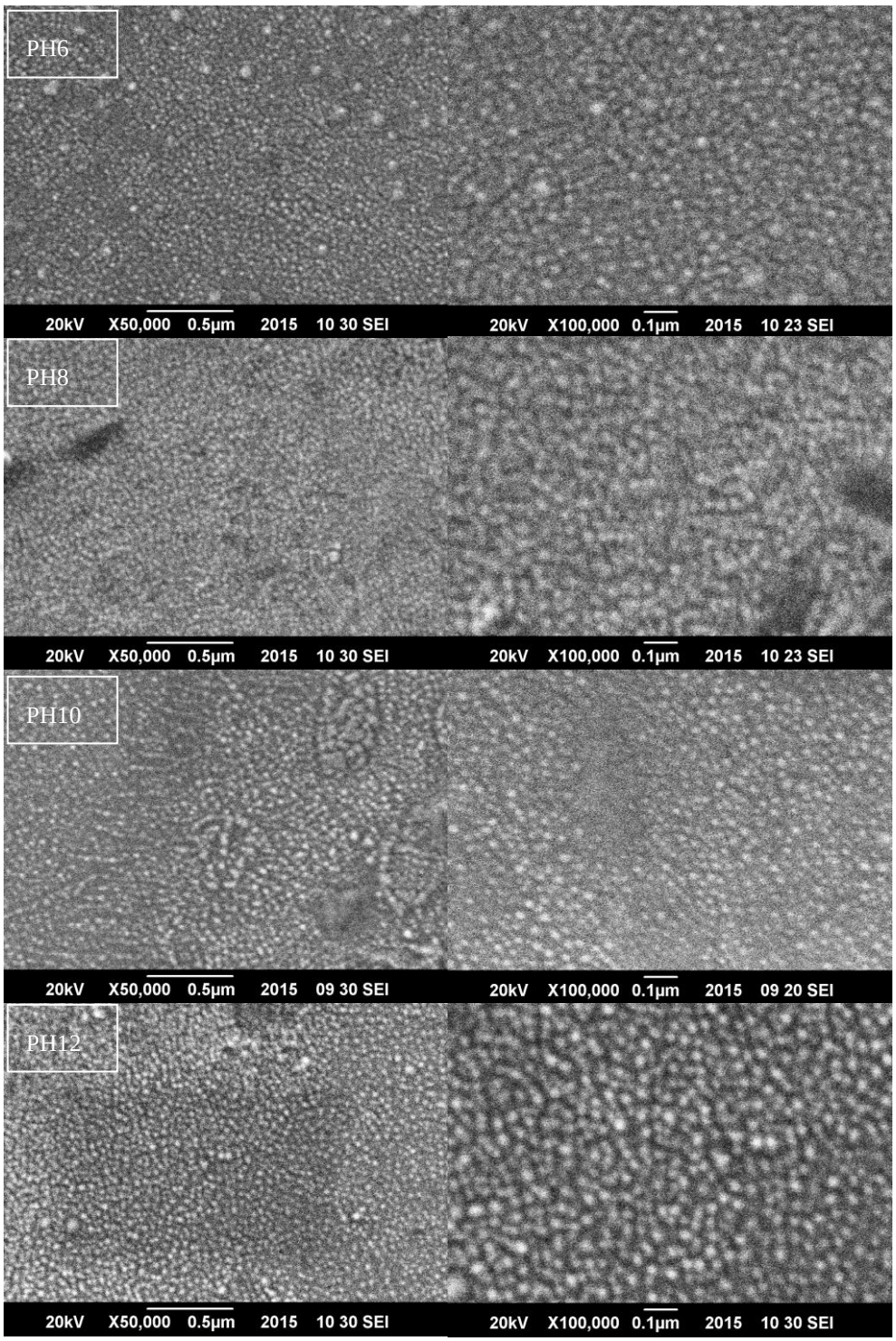


**Figure 3.14** Morphology of $CoFe_2O_4$ synthesized at varied pH.

EDS analysis was performed on a JEOL Model JSM6490A using secondary electrons at 20kV with 50X magnification to investigate the quantitative ratio of elements. The values of atomic ratio are tabulated in **Table 3.8.** The EDS analysis resulted in atomic ratio of Co:Fe:O = 8:25:67 for pH 6; Co:Fe:O = 12:24:64 for pH 8; Co:Fe:O = 15:27:58 for pH10; Co:Fe:O = 15:27:58 for pH12. Cobalt ratios were increasing while pH value increasing. While cobalt ratio is 8% at pH6, this ratio is almost two times increased at pH12 that is 15% value. R. Safi et al. also reported that the EDS spectra of the synthesized (pH 12) $CoFe_2O_4$ ferrite nanoparticles' result proved the existence of the main elements samples whose Co:Fe:O atomic ratio is 12:19:69 [203]. Hence, SEM images and EDS analyses showed that optimum pH parameter was pH12 for $CoFe_2O_4$ synthesis by using co-precipitation method.

| **Element** | **PH6** Fitting Coefficient : 0.7182 | | **PH8** Fitting Coefficient : 0.7740 | | **PH10** Fitting Coefficient : 0.7196 | | **PH12** Fitting Coefficient: 0.7120 | |
|---|---|---|---|---|---|---|---|---|
| | Mass % | Atom% | Mass % | Atom% | Mass % | Atom% | Mass % | Atom% |
| **O** | 36.43 | 66.96 | 33.11 | 63.78 | 27.75 | 57.75 | 27.51 | 57.46 |
| **Fe** | 47.52 | 25.02 | 43.21 | 23.84 | 45.84 | 27.33 | 45.72 | 27.36 |
| **Co** | 16.06 | 8.01 | 23.68 | 12.38 | 26.41 | 14.92 | 26.77 | 15.18 |

**Table 3.8**. Quantitative Analysis of $CoFe_2O_4$ at varied pH

### 3.2.2.4. Dielectric Permittivity and Dielectric Losses

The room temperature dielectric constant as a function of frequency from 100 Hz to 5 MHz for Co ferrite nanoparticles synthesized at different pH are shown in **Figure. 3.15** that was determined using **Eq. (2.3).**

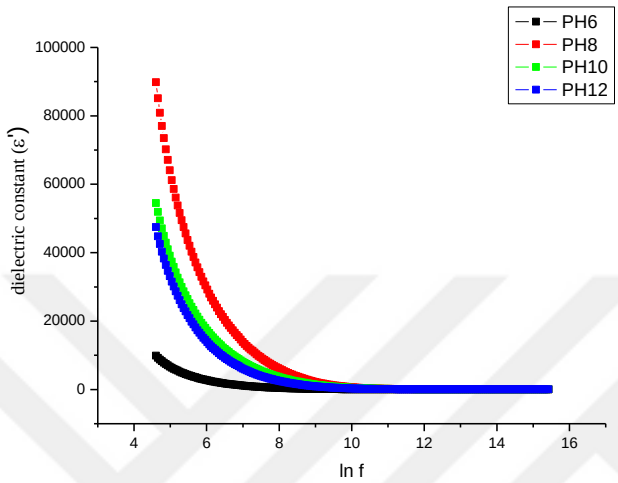


**Figure 3.15** Variation of dielectric constant with ln f of $CoFe_2O_4$ nanoparticles at room temperature.

The dielectric constant is lowest value at pH 6 while the highest value is at pH8 and pH12 value is lower than PH10 value . Dielectric constant highly depends on frequency that decreases with increase of frequency for every samples which is a characteristic behaviour of most of the ferrite materials [204]. At 5MHz frequency it is very small and becomes independent of frequency. The change in the dielectric constant of ferrites is mostly attributed to the variations in the concentration of $Fe^{2+}$[204]. A dielectric material consists of two different layers in which the well conducting grains are separated by poorly conducting grain boundaries. The high value of dielectric constant at lower frequency emerges from the grain boundaries since grain boundaries are dominant at lower frequency region whereas the grains are dominant at high frequency region [205]. The observed variation in dielectric constant may be understood on the basis of space charge polarization. The space-charge polarization occurs due to the diffusion of ions, along the external field direction, so it is giving rise to redistribution of charges in the dielectric substances. The subsequent charge build-up at the insulating grain boundary is a major contributor to the dielectric constant in ferrites. Hence, the more $Fe^{2+}$ ions in the ferrite, the more space charge polarization expected due to the

ease of electron transfer between 2+ and 3+ charged ions and afterwards higher the dielectric constant. The increased DC electrical resistivity obstructs the flow of space charge carriers and therefore impedes the build-up of space charge polarization. Since the DC electrical resistivity is monitored to increase with the higher reaction temperature in the present Co ferrites, thus the dielectric constant is expected to decrease with the higher reaction temperature effect as a result of the space charge polarization [206]. Manikandan et al. are also reported that has a same result with other researchers observations about ferrites [204].

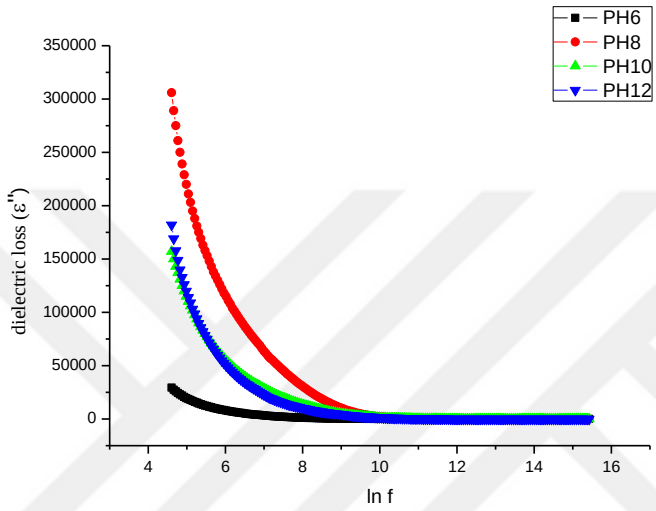


**Figure 3.16** Variation of dielectric loss with lnf of $CoFe_2O_4$ nanoparticles

Dielectric loss is an important part of the total core loss in ferrite nanoparticles [195]. The low dielectric losses are desirable for low core loss. The room temperature dielectric loss as a function of frequency from 100 Hz to 5 MHz for Co ferrite nanoparticles synthesized at different temperature is shown in **Figure. 3.16** that was determined using **Eq. (2.4)**. The dielectric loss profiles are similar to dielectric constant. The increase in hoping electrons result in a local displacement in the direction of the extent electric field that causing an increase in electric polarization enhances dielectric loss. Hudson [207] shows that the dielectric losses in ferrite is reflected in the conductivity measurements where the materials of high conductivity exhibiting high losses. [208].

### 3.2.3. Determination of Annealing Temperature of $CoFe_2O_4$

#### 3.2.3.1. TG-DTA Analyses

It is important to find out optimum annealing temperature range, because crystal size is also related to annealing factor. Thermal Gravimetric Analyses and Differential Thermal Analysis (TG-DTA) of the nanoparticles were conducted using Perkin Elmer Diamond TG-DTA system. TG-DTA measurements were performed at a 10˚C heating rate from 25˚C to 900˚C under nitrogen atmosphere. **Figure 3.17** shows TG-DTA results of $CoFe_2O_4$. TGA result indicates that the calcination of the $CoFe_2O_4$ nanoparticles took place in two steps The first step in the range between 25-500˚C was attributed to moisture removal, loss of bound water, elimination of organic residue and initiate the crystallization step. The weight loss after thermal treatment was around 20%. DTA curve indicates that endothermic peak between 50˚C and 100˚C which can be ascribed to vaporization of moisture. Calcination of $CoFe_2O_4$ occurred in a single stage, applying a heating rate of 10˚C /min; $CoFe_2O_4$ was calcined for 1h. Fernándeza C. P. et al. also reported TG-DTA result of nanoparticles, which nanoparticles % weight stayed stable after 500˚C [211].

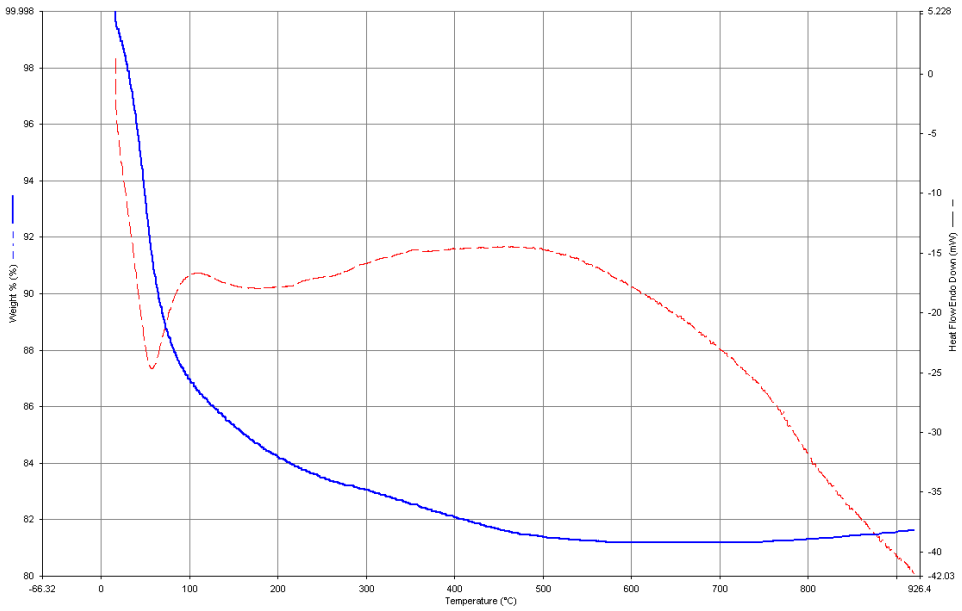


**Figure 3.17** TG-DTA results of $CoFe_2O_4$

### 3.2.3.2. XRD Analyses

XRD analyses were performed at 500˚C and 600 ˚C. The XRD patterns were taken using CuKα (λ= 1.5406A˚) radiation in 2θ range 20–80˚ at room temperature.. **Figure 3.18** show the XRD peaks of cobalt ferrite. XRD patterns of $CoFe_2O_4$ nanocrystal shows the specific crystallographic planes of $CoFe_2O_4$ are (220), (311), (400), (422), (511), and (440). Both samples can be indexed as the single-phase cubic spinel structure and no additional phase was detected. Prabhakaran et al. also reported same results that all samples can be indexed as the single-phase cubic spinel structure and no additional phase was detected [201]. The crystalline sizes were calculated using Scherrer formula [200]. **Table 3.9** describes the crystal size values of $CoFe_2O_4$ nanopowders at both calcination temperature. There is an increase in surface area and a decrease in particle size at the higher calcination temperature. XRD results show that values of crystal size are around 18nm and 11nm at 500 ˚C and 600 ˚C, respectively and first sample is noiser than second sample. Nadir S.E et al also reported effect of annealing temperature of nanoparticles crystallinity. The higher annealing temperature, the better crystallinity [212]. As a result, optimum annealing temperature is at 600 ˚C to make $CoFe_2O_4$ nanoparicles crystal structure and crystal size that is also optimum for further biomedical application.

| Annealing Temperature (ºC) | pH (approximately) | Process Temperature (ºC) | Avarege Crystall Size (nm) |
|---|---|---|---|
| 500 | 12 | 85 | 18 nm |
| 600 | 12 | 85 | 11 nm |

**Table 3.9**. Crystal size of $CoFe_2O_4$ at 500ºC and 600 ºC

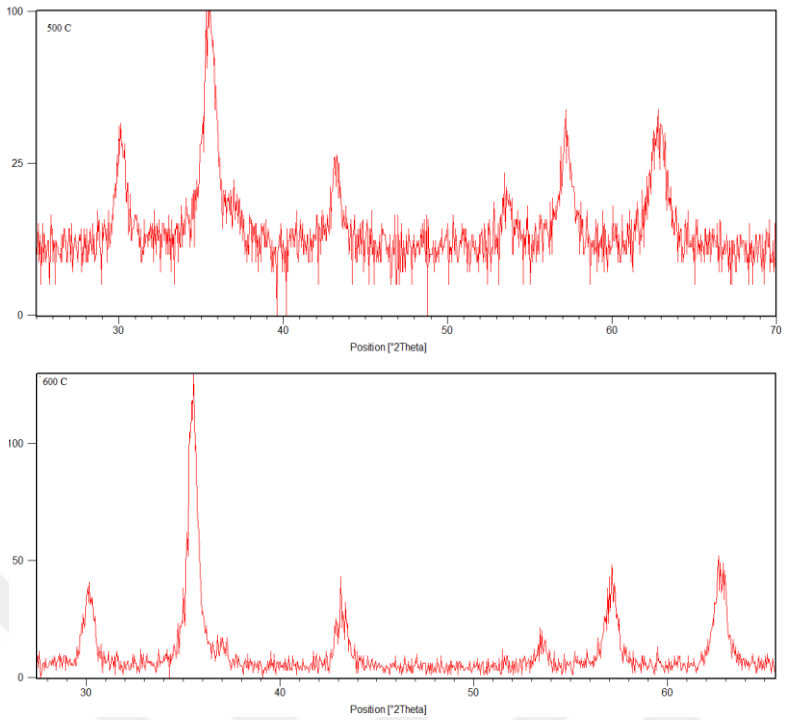


**Figure 3.18** XRD peaks of $CoFe_2O_4$ annealed at 500°C and 600 °C

### 3.2.3.3. AFM Analyses

AFM imaging was measured by JEOL, JSPM-5200 microscope at room temperature. Samples were made suspension with ethanol. Two drops of the suspended sample solutions was immediately spread on 10 x 10 mm glass slide`s surfaces. The samples were then allowed to dry under the 250 watt bulb for 15 minutes. **Figure 3.19** show 2D and 3D AFM images of $CoFe_2O_4$ at 500 ˚C and 600 ˚C to find out optimum annealing temperature. AFM images shows that both samples have good nanoparticle distrubutions. While average nanoparticle size is 14nm at 500˚C, average nanoparticle size is 9 nm at 600 ˚C. And maximum nanoparticle sizes are 22nm and 15nm for 500 ˚C and 600 ˚C, respectively. Bin Zhu et al. reported effects of annealing temperature on the structure and magnetic properties of $CoFe_2O_4$ that nanoparticle size increases with annealing temperature unlike our study [213]. AFM results also show that process performed at 600˚C is better choice for further process compared to performed at 500 ˚C.

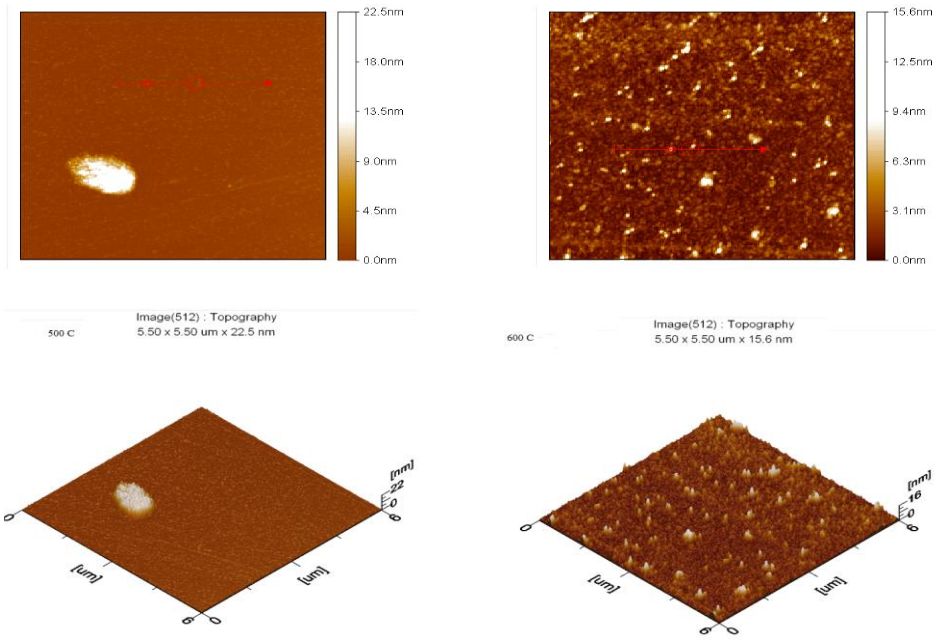


**Figure 3.19** Topography $CoFe_2O_4$ annealed at 500ºC and 600ºC

### 3.2.3.4. Magnetic Heating Test for Hyperthermia Application

$CoFe_2O_4$ nanoparticles were exposed to a 214 kHz alternating magnetic field of amplitude 22 Oe and a significant heating effect was observed in samples, which suggests potential for use in magnetic hyperthermia. Nanoparticle samples were placed in at thermally insulated vial and the heating curves were measured using a Neoptix fiber optic temperature sensor. Magnetic heating was performed by dispersing $CoFe_2O_4$ nanoparticles in phosphate buffer and subjecting to alternating magnetic field of 14A/m and frequency 214 kHz for 50 seconds. **Figure 3.20** shows that temperature variation with time of magnetic treatment. Initial temperature of fluid was at 18 ºC. Temperature of magnetic fluid increased to 200 ºC in 50 seconds. Temperature of nanoparticles fluid rose to at 45 ºC in about 19 seconds, which is an efficient temperature for hyperthermia treatment of cancer. T.E. Torres et al. are reported the magnetic properties of $CoFe_2O_4$ nanoparticles for magnetic hyperthermia that used four different magnetic field. At 229 kHz, temperature reached to 33 ºC in 60 seconds. At 444 kHz, temperature reached to 40 ºC in 30seconds. At 580 kHz, temperature reached to 37 ºC in 15 seconds. At 828 kHz temperature reached to 38 ºC in 10 seconds [214]. Hence, heat-generation of magnetic $CoFe_2O_4$ can be tailored by changing more suitable magnetic parameters like field strength, frequency of applied field and concentration of magnetic particles.

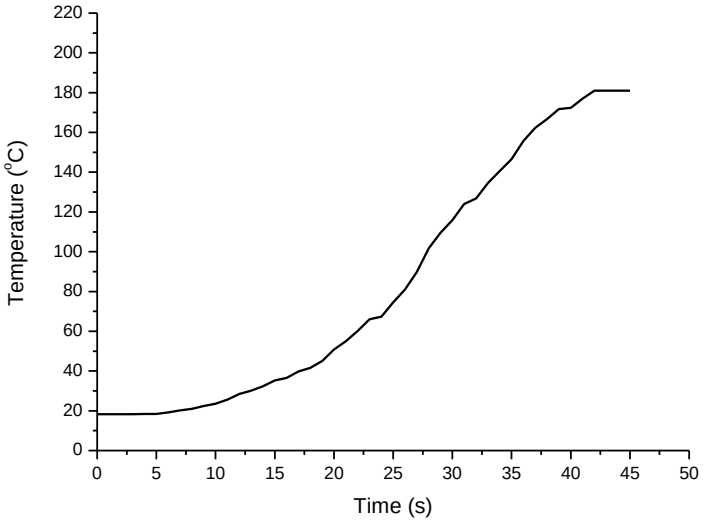


**Figure 3.20** Temperature variation with time of magnetic treatment.

### 3.2.3.5. Vibrating Sample Magnetometer (VSM)

**Figure 3.21** shows that performed at room temperature M(H) loops of the $CoFe_2O_4$ nanoparticles prepared at 85 $^oC$ and around pH 12 . The inset of **Figure 3.21** shows the changes in the saturation magnetization ($M_s$) values. It is clear that the value of saturation magnetization comes out to be **66** emu/g at room temperature for $CoFe_2O_4$ nanoparticles, which is significantly smaller than the bulk value (74.08 emu/g) [215]. Furthermore, the $H_c$ value and $M_r$ value are 150 Oe and 3,87 emu/gr, respectively. In the spinel ferrites, the magnetic order is mainly due to a super exchange interaction mechanism occurring between the metal ions in the A and B sublattices. M. Vadivel et al. , R.Safi et al., A. Manikandan et al. are also reported that hysteris curves are typical for a soft magnetic material and indicate hysteresis ferromagnetism [203,216,217].

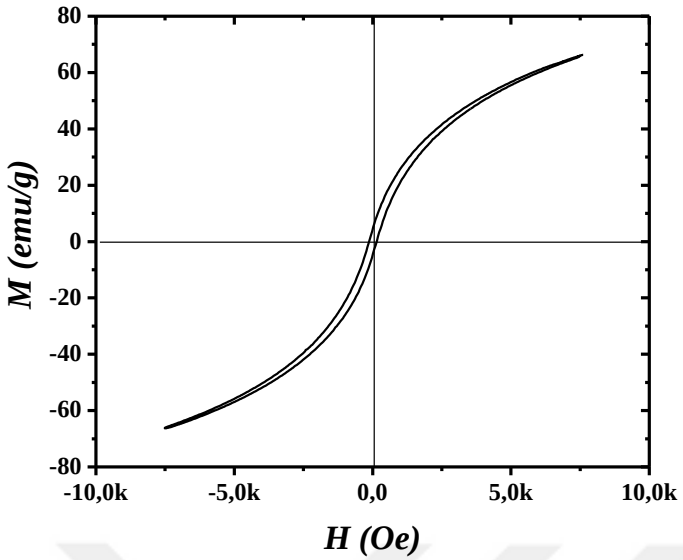


**Figure 3.21.** Hysterisis loop of $CoFe_2O_4$

## 3.3. Attachment of Functional Groups

### 3.3.1. Fourier Transform Infrared Spectroscopy (FT-IR)

Magnetic nanoparticles are synthesized by co-precipitation from $Co^{2+}$ and $Fe^{3+}$ using NaOH alkali solution. Nanoparticles were modified with PMIDA. PMIDA is an effective coupling agent which is containing one phosphonate and two carboxyl functions per molecule. FT-IR spectra of samples surface were recorded on a FT-IR, Perkin Elmer 100 series spectroscopy measurements were conducted between 350 and 4000 $cm^{-1}$. The samples were prepared by compaction of small amount of nano composite powder with KBr powder in a hydraulic press and pellets were made which were analyzed for functional groups present. The comparison of FT-IR spectrum of $CoFe_2O_4$ nanoparticles, PMIDA modified magnetic nanoparticles ($CoFe_2O_4$–PMIDA) was shown in **Figure 3.22.**

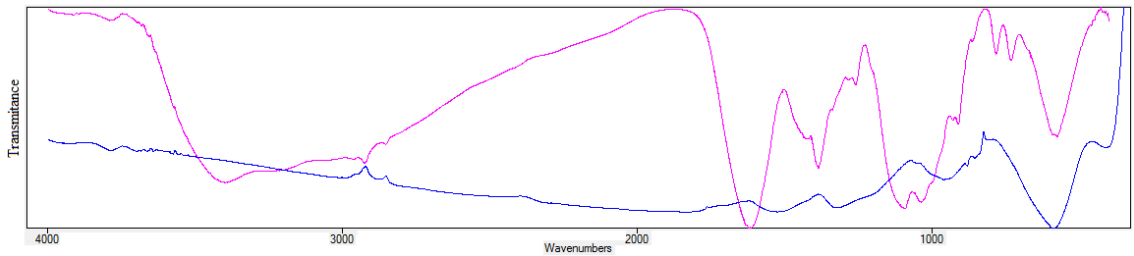


**Figure 3.22.** PMIDA modified magnetic nanoparticles, $CoFe_2O_4$ (blue) and $CoFe_2O_4$ -COOH (pink)

According to the geometrical configuration of the oxygen nearest neighbors, the metal ions are usually situated in two different sublattices in ferrites, designated as the tetrahedral and octahedral sites. The vibration spectra of spinel ferrites at the high frequency band (600–580 $cm^{-1}$) and the low-frequency band (440–400 $cm^{-1}$) are attributed to the intrinsic vibration of the tetrahedral sites and the octahedral sites, respectively [196]. Two main broad metal–oxygen bands are seen in the FT-IR spectra of studied pattern that are 590 $cm^{-1}$ large band and 400 $cm^{-1}$ band. The band around 590 $cm^{-1}$ is attributed to the intrinsic vibration of tetrahedral metal–oxygen complexes and the band around 400 $cm^{-1}$ to the intrinsic vibration of octahedral metal–oxygen complexes. The 590 $cm^{-1}$ band is high frequency that caused by stretching vibrations of tetrahedral metal–oxygen band and 400 $cm^{-1}$ band is low frequency absorption band that is caused by the metal–oxygen vibrations in octahedral sites. Gabal et al. also reported that two characteristic ferrite bands are appeared in 400 $cm^{-1}$ and 590 $cm^{-1}$[199]. Both bands are specific for $CoFe_2O_4$ magnetic nanoparticles.

By comparison, in the FT-IR spectrum of modified PMIDA, more bands could be identified: A band at 1200 - 1100 $cm^{-1}$ is corresponding to the P=O bond and the peak at 950-1040 $cm^{-1}$ is owing to the presence of M–O–P. The aliphatic C-N absorptions are found in 1250 $cm^{-1}$. The band 950–910 $cm^{-1}$ were attributed to O–H bend carboxylic acids. The Carboxylic Acids absorptions were found in 1650-1700 $cm^{-1}$. A significant difference of in the intensity of the band at 580 $cm^{-1}$ is observed which indicates the interaction of PMIDA on the $CoFe_2O_4$ surface. Sahoo B. et al. are also reported FTIR result of successfully achieved PMIDA modified magnetic nanoparticles [218]. All specific peaks confirm that $CoFe_2O_4$-PMIDA was successfully synthesized.

### 3.3.2. Fluorescence Spectrofotometer

Fluorescent spectra were performed by Hitachi F-4500 fluorescence spectrophotometer (Japan). Measurements were carried out between 240 nm and 400 nm (excitation and emission) by 150 W continuous Xenon Lamp using quartz cell. Wavelength Scan Speed is 2400 $nm.min^{-1}$. Fluorescence spectrum and image of PMIDA modified magnetic nanoparticles ($CoFe_2O_4$–PMIDA) was shown in **Figure 3.23.** The excitation and emission wavelengths used for measuring $CoFe_2O_4$-PMIDA is shown in **Table 3.10**. It shows the possibility of two band gap modalities with responsible for excitation and emission and

electron transfer between them. The loss during the electron transfer is considered to be the reason of distinct excitation and emission peak location with Stokes shift. In this hypothetical diagram, excitation occurs between 230-265nm wavelenghth and the emission process occurs in the right side between 265-300 nm wavelenght. Lee, C et al are also reported the 2,2 nm gold nanoparticle solution shows bright red emission with the excitation on UV plate[219].

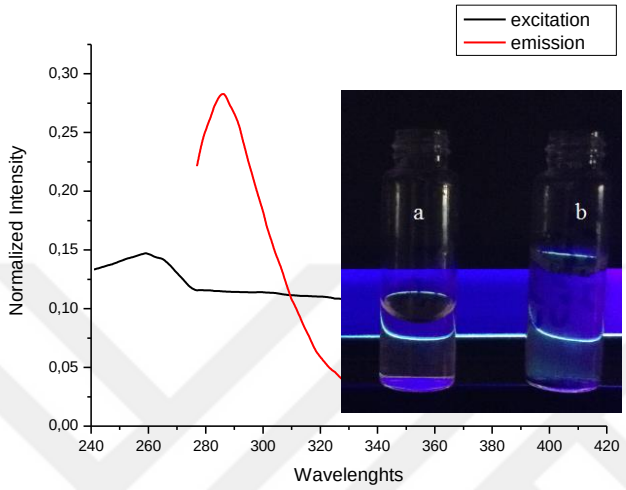


**Figure 3.23** Fluorescent properties of $CoFe_2O_4$-PMIDA, Photograph of blank sample (a) and CoFe2O4-PMIDA (b) under 254 nm UV light.

| Fluorescent properties | | |
|---|---|---|
| | Wavelenght(nm) | |
| $CoFe_2O_4$-PMIDA | Excitation | Emission |
| | 230- 265nm | 265-300nm |

**Table 3.10**. Fluorescent properties of modified $CoFe_2O_4$

## 3.4. Characterization of Folic Acid Attachment and Encapsulated Nanoparticle

### 3.4.1. Fourier Transform Infrared Spectroscopy (FT-IR)

Magnetic nanoparticles are synthesized by co-precipitation from $Co^{2+}$ and $Fe^{3+}$ using NaOH alkali solution. Nanoparticles were modified with PMIDA. PMIDA is an effective coupling agent which is containing one phosphonate and two carboxyl functions per molecule FT-IR spectra of the samples were recorded on a FT-IR, Thermo Nicolet 6700 FT-IR spectrophotometer equipped with a Smart Orbit high performance diamond attenuated total reflectance (ATR) accessories. Measurements were conducted between 400 and 4000 $cm^{-1}$. The comparison of FT-IR spectrum of $CoFe_2O_4$ nanoparticles, PMIDA modified magnetic nanoparticles ($CoFe_2O_4$–PMIDA) and conjugation of Folic Acid on activated magnetite nanoparticles were shown in **Fig. 3.24**.

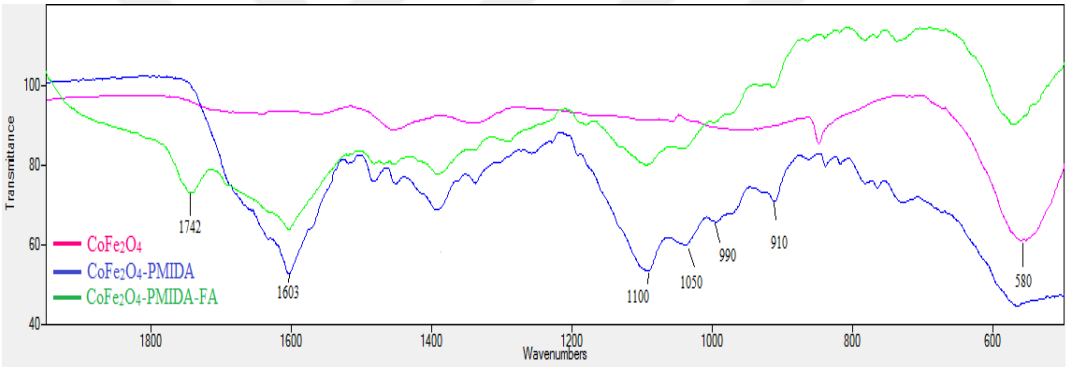


**Fig. 3.24** $CoFe_2O_4$ (pink), $CoFe_2O_4$ – PMIDA (blue) and $CoFe_2O_4$ – PMIDA-FA (green)

According to the geometrical configuration of the oxygen nearest neighbors, the metal ions are usually situated in two different sublattices in ferrites, designated as the tetrahedral and octahedral sites [196]. By comparison, in the FT-IR spectrum of modified PMIDA, more bands could be identified: A band at 1200 - 1100 $cm^{-1}$ is corresponding to the P=O bond and the peak at 950-1040 $cm^{-1}$ is owing to the presence of M–O–P. The aliphatic C-N absorptions are found in 1250 $cm^{-1}$. The band 950–910 $cm^{-1}$ were attributed to O–H bend carboxylic acids. The Carboxylic Acids absorptions were found in 1650-1700 $cm^{-1}$. A significant difference of in the intensity of the band at 580 $cm^{-1}$ is observed which indicates the interaction of PMIDA on the $CoFe_2O_4$ surface. Sahoo B. et al. are also reported FTIR result of successfully achieved PMIDA modified magnetic nanoparticles[218]. All specific

peaks confirm that $CoFe_2O_4$-PMIDA was successfully synthesized. The green colour FT-IR spectrum is conjugation of folic acid on activated magnetite nanoparticles which is successfully achieved. A band at 1740 $cm^{-1}$ is corresponding to the C=O stretch and represent of ester funtional groups. Monika Szymanska-Chargot et al. also showed characteristic ester peak at 1740$cm^{-1}$ in their application [220].

### 3.4.2. AFM Analyses

AFM imaging was measured by JEOL, JSPM-5200 microscope at room temperature. Samples were made suspension with $dH_2O$. Two drops of the suspended sample solutions were immediately spread on 10 x 10 mm glass slide`s surfaces. The sample was then allowed to dry under the 250 watt bulb for 15 minutes. AFM measures the nanometer-scale topography of surfaces through direct contact between a sample surface and a probe tip mounted on the end of a cantilever microbeam. The cantilever peak frequency was 169.534 kHz and the image resolution was 512 x 512 pixels. **Figure 3.25** shows topography of encapsulation of magnetic nanoparticles and **Figure 3.26** shows histogram of encapsulated nanoparticles. Atomic force microscopy (AFM) measurements showed an increment of surface roughness with encapsulation. AFM image shows encapsulated nanoparticles have homogen distributions and average encapsulated nanoparticle size is around 40nm. Nandakumar et al are also fabricated fibrous three-dimensional scaffolds made of a poly (ethylene oxide terephthalate)/poly (butylene terephthalate) copolymer to mimic the physical microenvironment of extracellular matrix and they are reported that AFM measurements determined an exponential increase of surface roughness [221].

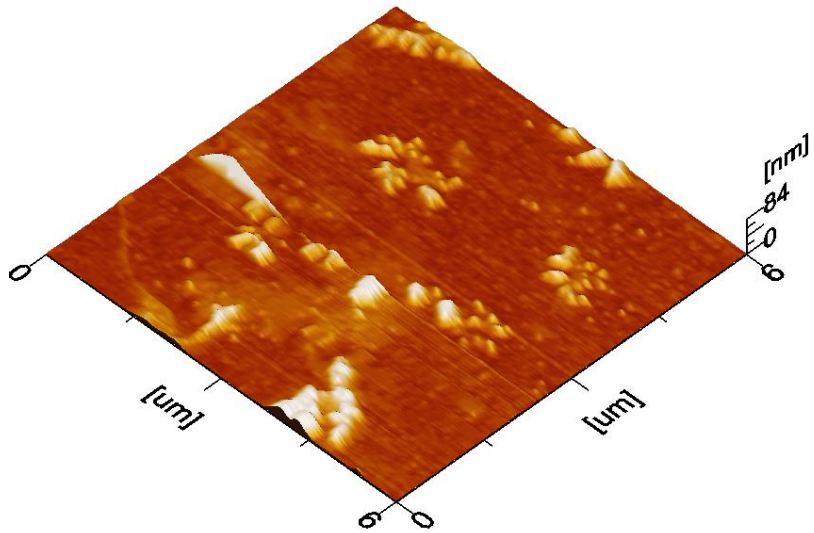


**Figure 3.25** Topography of Encapsulated Nanoparticle

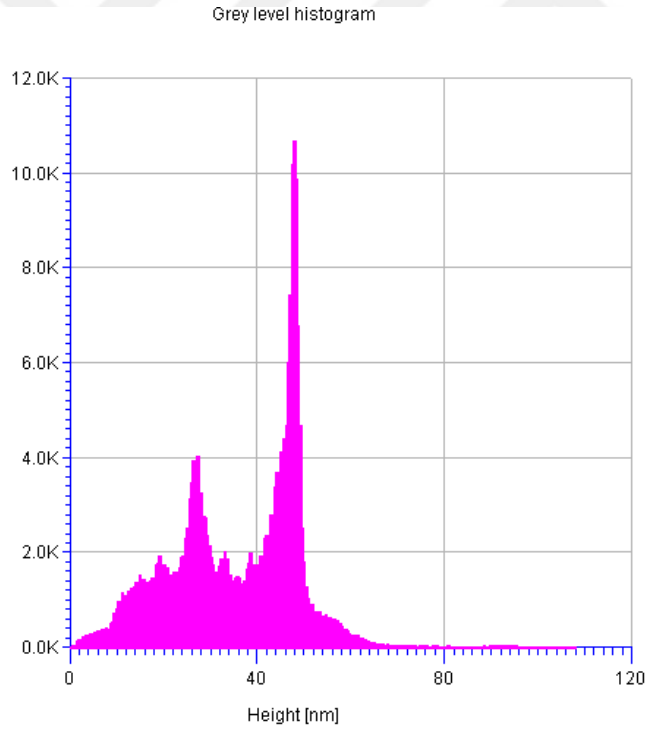


**Figure 3.26** Histogram of Encapsulated Nanoparticle

### 3.4.3. SEM Mapping

SEM analysis was performed on a JEOL Model JSM6490A using secondary electrons at 20kV with 70000X and 100000X magnifica to investigate the homogenity of nanoparticles. Samples were made suspension with dH2O. Two drops of the suspended sample solutions was immediately spread on 10*10 mm glass slide`s surfaces. The sample was then allowed to dry under the 250 watt bulb for 15 minutes. The last step, slides were prepared by sputter coating with gold. **Figure 3.28** shows morphology of nanoparticles that both images analysed two different magnificence are both spherical and homogen dispersity. **Figure 3.27** shows elemental mapping on the fracture surface of the encapsulated modified nanoparticles. Mapping images show that main elements of the sample such as Cobalt, Ferrite, and phosphorus have detected during analysis. It means encapsulation of modified nanoparticles might be achieved. K.Nadeem et al. also reported silica coated cobalt ferrite nanoparticles that morphology of nanoparticles are spherical and homogen dispersity [222].

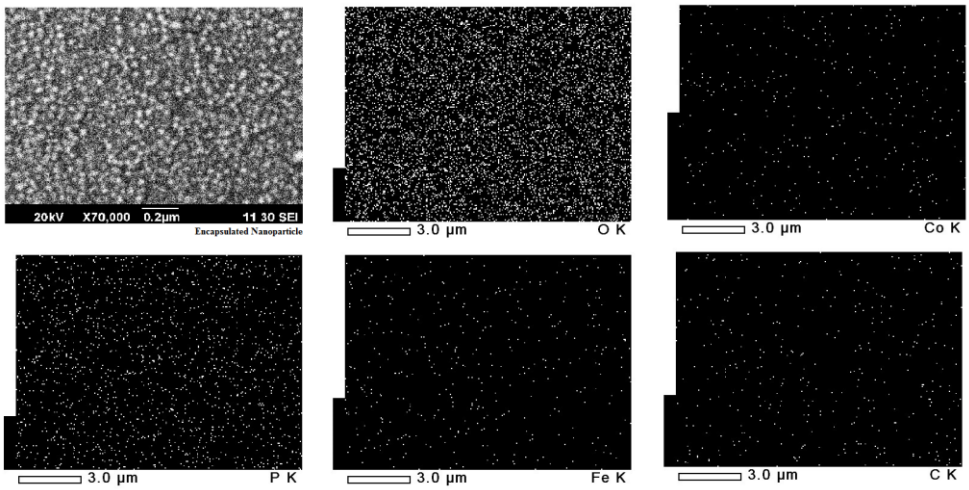


**Figure 3.27** Elemental Mapping on the Fracture Surface of the Encapsulated Nanoparticle

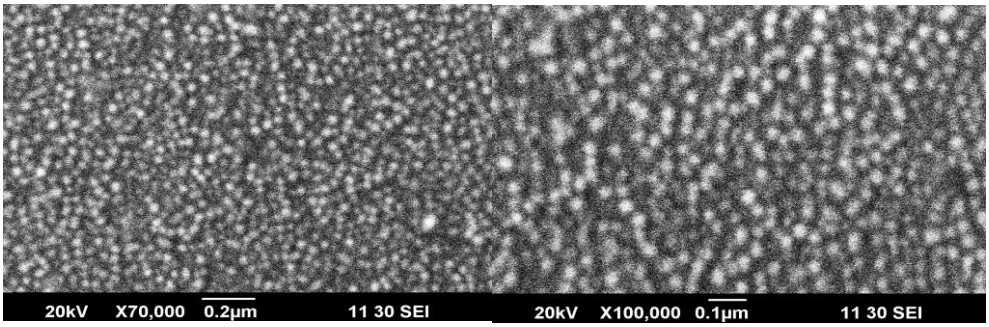


**Figure 3.28** Morphology of Encapsulated Nanoparticle

### 3.4.4. TEM (Transmission Electron Microscopy)

The morphology and the particle size of encapsulated $CoFe_2O_4$ were determined by Transmission Electron Microscopy (TEM). TEM analysis was performed on a Philips CM-200 using field emission gun. **Figure 3.29** show TEM images of the encapsulated nanoparticles. The TEM images show spherical morphology for $CoFe_2O_4$ with uniform particle sizes. These observations confirm the results of XRD, SEM, AFM analyses.

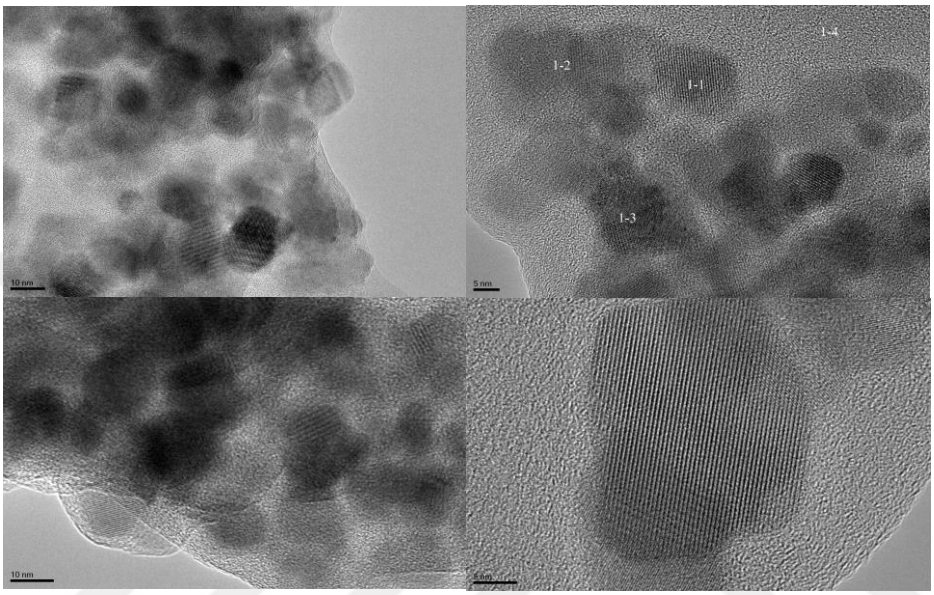


**Figure 3.29** TEM image of the Encapsulated Nanoparticles

## 3.5. Cell Culture Studies

### 3.5.1. Equipment sterilization

All equipments used in cell culture is sterilized. Micropipette, eppendorf, metal tools and glass equipments are autoclaved at 1-06 bar for 20 minutes in 121 ºC.

### 3.5.2. Preparation and Sterilization of Samples

Encapsulated and nonencapsulated samples are sterilized by UV radiation of 2 hr prior to use in cell culture experiments. 200µg/ ml stock solution of encapsulated and nonencapsulated nanoparticles are prepared in phosphate buffer saline (PBS).

### 3.5.3. *In vitro* Cell Culture Experiments

Each step of cell culture experiments are performed under steirle conditions with sterilie media. Cells are cultivated in sterile laminar air flow cabin to prevent yeast, bacteria or fungi contamination and incubated at 37 ºC with 5% $CO_2$ humid environment.

### 3.5.4. Cell Line

Adherent cell lines are used for in-vitro cell culture experiments. L929 murine fibroblast cell line is used for biocompatibility experiments.

### 3.5.5. In vitro Biocompatibility Test

To investigate biocompatibility of phosphonated levan encapsulated nanoparticles WST1 (4-[3-(4-iodophenyl)-2-(4-nitrophenyl)-2H-5-tetrazolio]-1,3benzenedisulfonate) cell proliferation and viability assay is performed L929 cell line. Cells grown in 10 ml complete DMEM (PAN Biotech) in 75 $cm^2$ tissue culture flask in humid atmosphere. When cells become confluent (70%) medium is sucked away and cells washed with 1 X PBS solution and trypsinized with 2 ml trypsin-EDTA (PAN BIOTECH) for 2-3 minute in 5% $CO_2$ at 37 ºC to detach adherent cells. After detachment cells are centrifugated at 1000 rpm for 5 minute to get rid of the trypsin which effect cellular viability. After centrifugation cells counted and 1.5 $10^4$ cell per well seeded into sterile 96 well culture plates and incubated at 5% $CO_2$ at 37 ºC overnight for cellular attachment. After steriliztion of nanoparticles cells incubated with 1, 10, 100 µg/ml of nanoparticle solutions for 24 h. At the end of incubation period 10 µl of WST1 solution was added to each well and the final product of WST-1 reaction were allowed

to incubate at 37 °C, in a 5% $CO_2$ humidified incubator for 2h. After incubation, absorbance of WST-1 was measured spectrophotometrically in a Promega GloMax®-Multi+ detection system at 460 nm. Each experiment was carried out three times in triplicate.

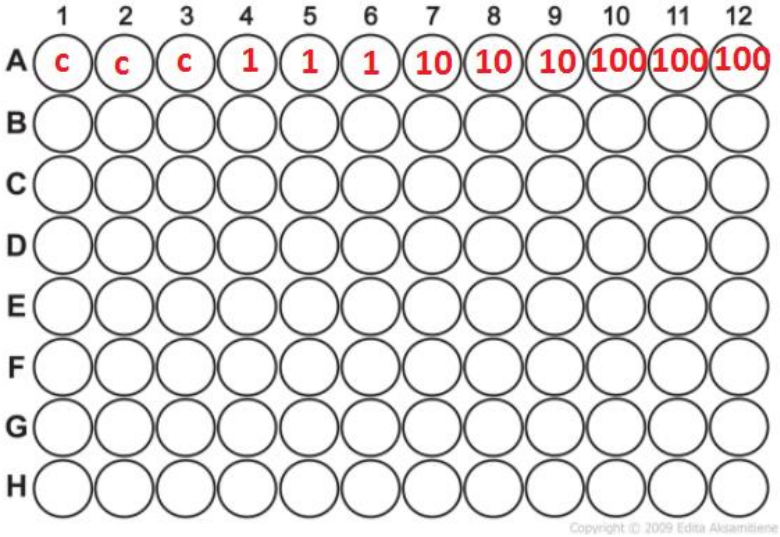


**Figure 3.30** schematic sketch for 96 well plate organization for biocompatibility test. C stands for control while 1, 10 and 100 is concentration of samples being incubated with L929 cells (µg/ml).

### 3.5.6. Statistical analysis

One-way ANOVA is used for statistical analyses followed by the Tukey test for multiple comparisons using the Prism analysis program (Graphpad, V 5.0). Data were presented as means and 95% confidence interval. A p-value of less than 0.05 was considered statistically significant.

### 3.5.7. Results

Biocompatibility results of L929 being incubated with encapsulated and native nanoparticle samples showed increased biocompatibility. Dose dependent increase is observed in noncapsulated samples while encapsulated ones showed decreased viability at the highest concentration which is 100 µg/ml. (**Figure 3.31**).

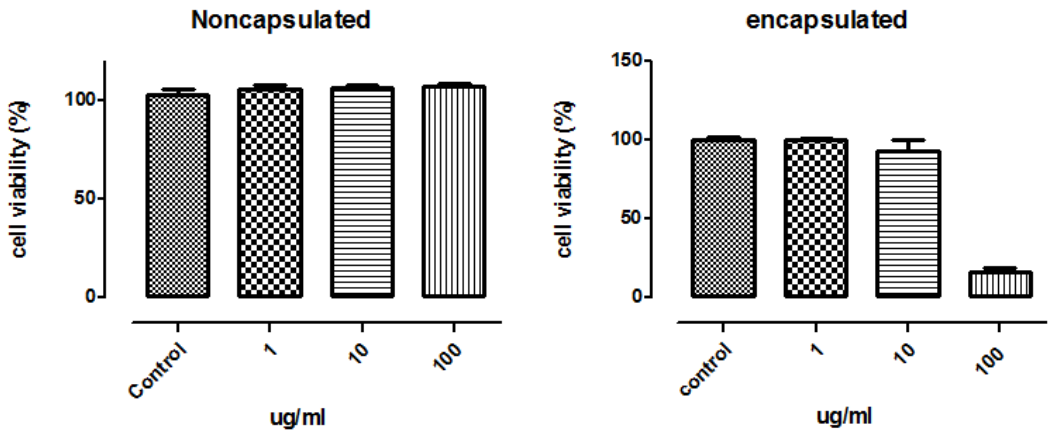


**Figure 3.31.** Biocompatibility results of samples after 24h cultivation with L929 cells.

Zhu et al. [223] investigated biocompatibility of 5-fluoroacyl carrier chitosan coated $Fe_2O_3$ magnetic nanoparticles with K-562 (human leukemia cells) and increased cellular apoptosis rate is observed at the concentration of 5 µg/ml which is the highest. Mushtag et al [224] investigated cytotoxicity of polymer coated $CoFe_2O_4$ magnetic nanoparticles with CHO (Chinese Hamster Ovarian)and Huh-7 (Human Hepatocarcinoma) cells with the concentration range of 0 to 0.18 mg/ml and cellular viability is observed above 80 % even at the highest concentration. Hathout et al [225] investigated cytotoxic properties of $CoFe_2O_4$ magnetic nanoparticles with MCF-7 (Human Breast Cancer) Cell line with varying concentrations and after 1 mg/ml cellular viability is reduced below 67%.

This unexpected result might be related with dissolving problems of samples observed during treatment. Phosphonated levan encapsulated samples took much effort and time to dissolve and none of the samples could fully dissolved this problem may result inadequate accumulation of samples on cells and this may result reduced cellular viability.

Biocompatibility studies with encapsulate samples need to be repeated after optimization of homogenous dissolving of nanoparticles. Anticancer activity studies of samples need to performed with folate receptor containing and folate receptor deficient cancer cells. Hyperthermia studies need to be performed with health and those cancer cell line. Preliminary experiments show promising results depending on nontoxic features of samples. Phosphonated levan is reported as biocompatible polymer in previous studies [151] improving features of nanoparticles with folic acid and phosphonated levan could increase uptake of magnetic nanoparticles into cancer cells and hyperthermia studies could open a new era in cancer therapy with non toxic, highly anticancer activities.

## 4. CONCLUSIONS AND RECOMMENDATIONS

In this study, the main goal was to to obtain nanoparticles suitable for hyperthermia applications, which is an alternative to cancer treatments. For Hyperthermia application, $CoFe_2O_4$ nanoparticles were obtained using the co-precipitation method. The co-precipitation method can achieve fast results and does not leave toxic by-products and hence preferred for biomedical applications. The shape and dimensions of nanoparticles are important parameters for hyperthermia application. During the synthesis of nanoparticles, parameters such as pH, reaction temperature, mixing speed and sintering temperature affect the size of the nanoparticles. The nanoparticles should be at optimum size to allow circulation for longer periods in the bloodstream. Optimum nanoparticles were tried to be obtained at different temperatures and pH ranges and at different temperatures of sintering. With reference to the fact that the co- precipitation method on many articles gives a positive result over pH 12. Synthesizes were carried out at with reference to the positive results above pH 12 at the temperatures of 75$^o$C, 80$^o$C, 85$^o$C, 90$^o$C. The reaction temperature increases with NaOH by 1-2 $^o$C. It is necessary to increase the reaction temperature in a controlled manner to prevent the increase of the reaction temperature after NaOH addition. To control this, the base solution at the same temperature should be added after a slight decrease in the temperature before adding the base solution and the temperature control adjusted to the desired temperature. The thermometer must be continuously checked during the reaction as the temperature is easily changed. All experiments were carried out using a mechanical stirrer at 300 rpm. AFM, XRD, SEM, EDS, FTIR analysis showed that homogeneously dispersed spherical particles were obtained at optimum size at 85$^o$C. Afterwards, the formation of nanoparticles was observed at pH 6 -8-10-12 while the temperature was kept constant at 85 ° C. After the addition of NaOH, it was observed that pH 6 samples were in pink tones, pH 8 samples in orange tones, pH 10 and pH 12 samples were black. It was observed that the pH 10 and pH 12 samples were separated from the supernatant more rapidly during their purification compared to the pH 6 and pH 8 samples. The AFM, XRD, SEM, EDS, FTIR analysis results of the pH parameters showed that the ideal result was around pH 12 as written in the literature.

Sintering studies used nanoparticles synthesized at 85 ° C and pH 12. Due to the constant TGA data remaining after 500 °C of the TG-DTA analysis nanoparticles, the shape and size of the nanoparticles were observed at 500°C and at 600°C. XRD and AFM results

showed that the ideal result are at 600°C. The size of the obtained nanoparticles is around 20 nm. Firstly, the functionalized groups were attached to the obtained CoFe2O4 nanoparticles and then the folic acid compound was attached as a ligand. Folate receptors are present only in cancer cells while are not found in healthy cells. Thus, Folic acid-bound nanoparticles can be targeted to cancer cells without affecting normal cells. The modified $CoFe_2O_4$ nanoparticles showed fluorescence at around 265 nm. This fluorescent properties demonstrate that the effect on the cancer cells can be followed without attaching any fluorescence groups to the nanoparticles.

Levan is a polymer that speaks of his name in the world of science with its characteristic formation process and positive results as biopolymer. There are areas of use in cosmetics, food and pharmaceuticals fields and as antitumor agents. Levan derivatives such as phosphate, sulfate and acetate have been reported in the field of medicine as anti-aids, food additives. It has been observed that there are not too many literatures in relation to levan phosphonate, but in the our experiments showed that it is more sticky than the pure levan and it is a hydrophilic biopolymer.

It is reported that OH groups are more sensitive to RES cells and that hydrophilic biopolymers have greater ability to escape from macrophages in the RES mechanism. Because of this reason, levan was phosphonated using PCI3 compound to reduce -OH groups on the structure. In light of these properties, it is predicted that when nanoparticles are encapsulated with levan phosphonate, they will stay longer in the bloodstream. Due to stay longer in the bloodstream, nanoparticles efficiency is expected to increase. The SEM-EDS and mapping results showed that the main elements such as P, Co, Fe, C, O was found in the structure. Furthermore, the TEM results indicate that the encapsulation has taken place successfully. AFM result showed that the particle size was measured to be about 40 nm after encapsulation. Nanoparticles at this size are the suitable size for hyperthermia application. During exposure to $CoFe_2O_4$ magnetic field, temperature increased to 45$^{o}$C in the 19 sec time. Result showed that the desired temperature range could be obtained in a very short time which might be ideal for hyperhermia application. The future plans of the study will keep on *in vivo* experiment. By the Co-Fe ratios of magnetic materials can be changed to improve the magnetic properties to get the stable temperatures and the exposure time. Also, heat-generation of magnetic $CoFe_2O_4$ can be tailored by changing more suitable magnetic parameters like field strength, frequency of applied field and concentration of magnetic particles. VSM analysis gave consistent results with earlier studies. Due to the fact that

$CoFe_2O_4$ is a soft ferromagnetic material, it exhibits a little bit permanent magnetic property. For biomedical studies, more effective results can be obtained *in vivo* and *in vitro* studies with improving the nanoparticle to be fully paramagnetic.

# References


[1] http://www.nano.gov/nanotech-101/what/nano-size [accessed Feb 15, 2016].

[2] Garimella R. ; Eltorai A.E.M. (2017). "Nanotechnology in orthopedic". Journal of Orthopaedics 14, 30–33 review

[3] Feynman R. (1960). "There's plenty of room at the bottom". Eng Sci, 23, pp. 22–36.

[4] Gribbin J., Gribbin M. ,Richard Feynman (1997). "A Life in Science". p. 170. ISBN 0-452-27631-4.

[5] Taniguchi, N. (1974)."On the Basic Concept of 'Nano-Technology" Proceedings of the International Conference on Production Engineering, Tokyo, , Part II, Japan Society of Precision Engineering.

[6] Wang J., Ren F., Yi R., Yan A., Qiu G.,Liu X. (2009). "Solvothermal synthesis and magnetic properties of size-controlled nickel ferrite nanoparticles", Journal of Alloys and Compounds 479, 791–796.

[7] Mathew D.S., Juang R. S. (2007). "An overview of the structure and magnetism of spinel ferrite nanoparticles and their synthesis in microemulsions", Chemical Engineering Journal 129, 51–65.

[8] Roduner E: "Size matters: why nanomaterials are different", Chem. Soc. Rev. 35 583- 592.

[9] Buzea C., Blandino Pacheco I., Robbie K. (2007), "Nanomaterials and nanoparticles: Sources and toxicity", Biointerphases vol. 2, issue 4, pages MR17 - MR172

[10] Ekimov, A. I. (1981). "Onushchenko", A. A. JETP Lett., 34, 345–349.

[11] http://www.amercrystalassn.org/content/pages/main-careers [accessed Feb 16, 2017].

[12] J.R. Hook, H.E. Hall, John Wiley and Sons, (2010). "Solid State Physics" (2nd Edition), Manchester Physics Series, , ISBN 978-0-471-92804-1.

[13] International Tables for Crystallography (2006). Volume A, Space-group symmetry.

[14] http://chemed.chem.purdue.edu/genchem/topicreview/bp/ch13/unitcell.php#top [accessed Feb 15, 2017].

[15] Suryanarayana C., Grant Norton M. (1998). "X-Ray Diffraction: A Practical Approach", 26.

[16] Daniel L. Reger., Goode S.R., Ball D.W. (2009). Chemistry: Principles and Practice, chapter 11, page 452,

[17] http://spaceflight.esa.int/impress/text/education/Glossary/Glossary_B.html

[18] Whittaker E. J. W. (2013). "Crystallography: An Introduction for Earth Science", chapter 4, page 30,

[19] http://www.diracdelta.co.uk/science/source/m/i/miller%20indices/image001.gif [accessed Feb 15, 2017].

[20] Massimi M. (2005). "Pauli's Exclusion Principle: The Origin and Validation of a Scientific Principle", Cambridge University Press.

[21] Buschow K.H.J, Boe F.R. (2003). "Physics of Magnetism and Magnetic Materials", page 171.

[22] Fahlman B. (2011). "Materials Chemistry, Second edition", page 221.

[23] https://www.linkedin.com/pulse/measuring-principle-oxygen-through-paramagnetic-property-fontes

[24] Winn W. (2010). "Introduction to Understandable Physics: Electricity, Magnetism and Light", vol 3, page 23-36.

[25] Brown T. L., H. May E., Bursten B.E., Murphy C., Woodward P., Langford S., Sagatys D., George A. (2013). "Chemistry: The Central Science", Pearson Higher Education AU, page 855,

[26] https://www.slideshare.net/belalelnagar3/mag-prop [accessed Feb 20, 2017].

[27] Bertotti G. (1998). "Hysteresis in Magnetism: For Physicists, Materials Scientists, and Engineers", page 11.

[28] http://www.itacanet.org/wp-content/uploads/2011/06/hyst-587x600.jpg [accessed March 2, 2017].

[29] Murray G., White C.V., Weis W. (1993). "Introduction to Engineering Materials: Behavior: Properties, and Selection", page 511.

[30] C. Behera , R. N. P. Choudhary , Piyush R. Das, (2015). "Size effect on electrical and magnetic properties of mechanically alloyed $CoFe_2O_4$ nanoferrite",Journal of Materials Science: Materials in Electronics, Volume 26, Issue 4, pp 2343-2356.

[31] http://www.kshitij-iitjee.com/Study/Physics/Part6/Chapter30/65.jpg [accessed March 2, 2017].

[32] http://electrons.wdfiles.com/local--files/magnetism-iron-oxide-magnetite/magtypes.gif [accessed March 2, 2017].

[33] Mark J. E. (2007). "Physical Properties of Polymers Handbook", page 791,

[34] "Size and shape effects on Curie temperature of ferromagnetic nanoparticles", Trans. Nonferrous Met. SOC. China 17 (2007) 1451-1455

[35] C. Behera , R. N. P. Choudhary , Piyush R. Das, (2015). "Size effect on electrical and magnetic properties of mechanically alloyed $CoFe_2O_4$ nanoferrite",Journal of Materials Science: Materials in Electronics, Volume 26, Issue 4, pp 2343-2356.

[36] Nadeem K., Ali L., Gul I., Rizwan S., Mumtaz M. (2014). "Effect of silica coating on the structural, dielectric, and magnetic properties of maghemite nanoparticles", Journal of Non-Crystalline Solids 404 72–77.

[37] Warnes L.A.A. (2012). "Electronic Material", page 190,

[38] S. Kumar, T.J. Shinde, P.N. Vasambekar, J. (2015) "Magn. Magn. Mater". 379, 179.

[39] E. C. Mendonça, M. A. Tenório, S. G. Mecena, B. Zucolotto, L. S. Silva, C. B. R. Jesus, C. T. Meneses, and J. G. S. Duque, (2015). "J. Magn. Magn. Mater", 395, 345.

[40] Q.A. Pankhurst, N.K.T. Thanh, S.K. Jones, J. Dobson, (2009). "Progress in applications of magnetic nanoparticles in biomedicine", J. Phys. D: Appl. Phys. 42, 224001.

[41] C.C. Berry, (2009). "Progress in functionalization of magnetic nanoferrites for applications in biomedicine", J. Phys. D: Appl. Phys. 42 224003.

[42] Papis E, Rossi F, Raspanti M, Isabella DD, Colombo G, Milzani A, (2009). "Engineered cobalt oxide nanoparticles readily enter cells", Toxicol Lett,189:253–9.

[43] Parkes LM, Hodgson R, Lu LT, Tung LD, Robinson I, Fernig DG, (2008). "Cobalt nanoparticles as a novel magnetic resonance contrast agent" , Contrast Media Mol Imaging, 3:150–6.

[44]. Chattopadhyay S, Dasha K.S, Mandala D., Dasa B., Tripathya S., Deya A., Pramanik P., Roya S.(2016).“ Metal based nanoparticles as cancer antigen delivery vehicles formacrophage based antitumor vaccine” Vaccine,34, 957–967.

[44] D. H. Chen and X. R. He, Mater. Resea (2001). Bullet. 36 1369.

[45] Pervaiz E. (2013). "Synthesis and Characterization of Cobalt and Nickel Based Spinel Ferrites by Wet Chemical Methods" ,PhD thesis, National University of Sciences and Technology (NUST),

[46] Byrappa K., Adschiri T., (2007). "Progress in Crystal Growth and Characterization of Materials" 53, 117.

[47] D. Langevin, (1992). Annu. Rev. Phys. Chem. 43 341.

[48 ] Bee A., Massart R., Neveu S. (1995). J. Magn. Magn. Mater. 149, 6.

[49] Šmerková K., Blažková I. , Chudobová, D., Vaculovičová M., Kopel P., Adam V., Kizek R. (2013). "Fluorescence Properties of Quantum Dots", Mendel Net, 934-939,

[50] Brkić S. (2016). "Optical Properties of Quantum Dots", European International Journal of Science and Technology Vol. 5 No. 9.

[51] http://www.nanotech-now.com/images/QDot-nanocrystal.jpg [accessed March 3, 2017].

[52] Mandal, S. (2010)."Polyelectrolyte based NANO-approaches for Cancer therapy or diagnostics".

[53] Lodish H, Berk A, Zipursky SL, et al. New York,W. H. Freeman, (2000). "Molecular Cell Biology", 4th edition.

[54] http://www.mynutrilosophy.com/images/cancer-cells.jpg [accessed March 3, 2017].

[55] Blows W. T.: The Biological Basis of Nursing: Cancer, Routledge, Jul 13, 2006.

[56] https://www.cancer.gov/images/cdr/live/CDR761240-750.jpg

[57] Elaine A. Moore, Samantha W. "The Promise of Low Dose Naltrexone Therapy: Potential Benefits in Cancer" Page 82.

[58] Green, D. (2011). "Means to an End: Apoptosis and other Cell Death Mechanisms", Cold Spring Harbor, NY: Cold Spring Harbor Laboratory Press. ISBN 978-0-87969-888-1.

[59] Hayflick L, Moorhead P.S.(1961). "The serial cultivation of human diploid cell strains", Exp Cell Res. 25 (3): 585–621. doi:10.1016/0014-4827(61)90192-6.PMID 13905658.

[60] Hayflick L. (1965). "The limited in vitro lifetime of human diploid cell strains". Exp. Cell Res. 37 (3): 614–636.doi:10.1016/0014-4827(65)90211-9. PMID 14315085.

[61] Feng F.et al.(1995). "The RNA component of human telomerase", Science, 269 (5228): 1236–1241.doi:10.1126/science.7544491. PMID 7544491.

[62] Ainsley C. (2016). "The Physical Body, the Spiritual Body: Physical and Spiritual Bodies Compared", Balboa Press, Nov 21.

[63] Isaac L. (2011). "21st Century Cancer Treatment".

[64] William S., Elizabeth A. M. Frost. (2014). "Surgery Before and After the Discovery of Anesthesia, The Wondrous Story of Anesthesia" pp 163-183.

[65] Kirby I. Bland, Edward M. Copeland. (2009). "The Breast: Comprehensive Management of Benign and Malignant Diseases", Elsevier Health Sciences, Volume 2.

[66] Neo-adjuvant chemotherapy: proceedings of the First International Congress on Neo-Adjuvant Chemotherapy held in Paris (France), 6-9 November, 1985.

[67] Nordqvist C. (2015). "Chemotherapy: Types, Uses, Side Effects".

[68] Camp-Sorrell(2011). "D. Chemotherapy toxicities and management". Yarbro, CH, Wujcki D, Holmes Gobel B. Cancer Nursing: Principles and Practice. (7th Edition). Sudbury, MA: Jones and Bartlett. 17: pp. 458-503.

[69] Lawrence TS, Ten Haken RK, Giaccia A. (2008). "Principles of Radiation Oncology", In: DeVita VT Jr., Lawrence TS, Rosenberg SA, editors. Cancer: Principles and Practice of Oncology. 8th edition, Philadelphia: Lippincott Williams and Wilkins.

[70] http://www.cancerresearchuk.org/about-cancer/cancers-in-general/treatment/hormone/general-side-effects-of-hormone-therapy#7CihMzzXpCZ753Ty.99. [accessed March 3, 2017].

[71] Abraham J, Staffurth J. (2008)."Hormonal therapy for cancer", Medicine, Volume 36, Issue 1, 29–32.

[72] Tran N., Webster T.J. (2010). "Magnetic nanoparticles: Biomedical applications and challenges", Journal of Materials Chemistry 20, 8760–8767.

[73] Giri J., Pradhan P., Sriharsha T., Bahadur D.(2005), "Preparation and investigation of potentiality of different soft ferrites for hyperthermia applications", Journal of Applied Physics 97 10Q916-910Q916-913.

[74] Dutz S., Clement J.H., Eberbeck D., Gelbrich T., Hergt R., Muller R.(2009). "J. Wotschadlo, M. Zeisberger, Ferrofluids of magnetic multicore nanoparticles for biomedical applications", Journal of Magnetism and Magnetic Materials 321, 1501–1504.

[75] Hiergeist R., Andra W., Buske N., Hergt R., Hilger I., Richter U., Kaiser W., (1999) "Application of magnetite ferrofluids for hyperthermia", Journal of Magnetism and Magnetic Materials 201, 420–422.

[76] Danhier F, Feron O, Préat V. (2010). "To exploit the tumor microenvironment: Passive and active Tumor Targeting of Nanocarriers for Anti-cancer Drug Delivery", J Control Release, 1;148(2):135-46.

[77] Rani, K. and S. Paliwal "A Review on Targeted Drug Delivery: its Entire Focus on Advanced Therapeutics and Diagnostics".

[78] Sinha R, Kim GJ, Nie S, Shin DM. (2006). "Nanotechnology in cancer therapeutics: bioconjugated nanoparticles for drug delivery", Mol. Cancer Ther.5(8),1909–1917.

[79] Smith AM, Duan H, Mohs AM, Nie S. (2008). "Bioconjugated quantum dots for *in vivo* molecular and cellular imaging",Adv. Drug Deliv. Rev.60 (11),1226–1240.

[80] Matsumura Y, Maeda H. (1986). "A new concept for macromolecular therapeutics in cancer chemotherapy –mechanism of tumoritropic accumulation of proteins and the antitumor agent smancs", Cancer Res. 46 (12 Pt 1),6387–6392.

[81] Maeda H., Sawa T., Konno T. (2001) "Mechanism of tumor-targeted delivery of macromolecular drugs, including the EPR effect insolid tumor and clinical overview of the prototype polymeric drug SMANCS", J. Control. Release 74, 47–61.

[82] Unezaki S.,Maruyama K.,Hosoda J.,Nagae I.,Koyanagi Y.,Nakata M.,Ishida O., Iwatsuru M.,Tsuchiya S. (1996)."Directmeasurement of extravasation of polyethyleneglycolcoated liposomes into solid tumor tissue by in vivo fluorescence", Int. J. Pharm. 144, 11–17.

[83] Danhier F., Feron O., Préat V.(2010). "To exploit the tumor microenvironment: Passive and active tumor targeting of nanocarriers for anti-cancer drug delivery", Journal of Controlled Release 148 135–146.

[84] Malam Y., Loizidou M., Seifalian A.M. (2009). "Liposomes and nanoparticles: nanosized vehicles for drug delivery in cancer", Trends Pharmacol. Sci. 30 592–599.

[85] Gullotti E., Yeo Y. (2009). "Extracellularly activated nanocarriers: a new paradigm of tumor targeted drug delivery", Mol. Pharm. 6, 1041–1051.

[86] Bae Y.H. (2009). "Drug targeting and tumor heterogeneity", J. Control. Release, 133, 2–3.

[87] Heldin C.H., Rubin K., Pietras K., Ostman A. (2004). "High interstitial fluid pressure an obstacle in cancer therapy", Nat. Rev. Cancer 4, 806–813.

[88] Peer, D., J. M. Karp, S. Hong, O. C. Farokhzad, R. Margalit and R. Langer (2007). "Nanocarriers as an emerging platform for cancer therapy." Nature nanotechnology 2(12): 751-760.

[89] Mohanty, C., M. Das, J. R Kanwar and S. K Sahoo (2011). "Receptor mediated tumor targeting: an emerging approach for cancer therapy." Current drug delivery 8 (1): 45-58.

[90] Mostafavi, S. H. and R. Jayachandra Babu (2013). "Nano-Sized Drug Delivery." Journal of Molecular Pharmaceutics & Organic Process Research.

[91] Kumar Khanna, V. (2012). "Targeted delivery of nanomedicines." ISRN pharmacology.

[92] Bertrand, N., J. Wu, X. Xu, N. Kamaly, O. C. Farokhzad (2014). "Cancer nanotechnology: The impact of passive and active targeting in the era of modern cancer biology." Advanced drug delivery reviews 66: 2-25.

[93]Garg, A. (2009). "Targeted drug delivery and enhanced intracellular release using functionalized liposomes".

[94] Moghimi S.M, Peer D., Langer R. (2011). "Reshaping the future of nanopharmaceuticals: ad iudicium". ACS Nano , 5:8454–8.

[95] Xiao Z, Levy-Nissenbaum E, Alexis F, Lupta´k A, Teply BA, Chan JM, (2012). "Engineering of targeted nanoparticles for cancer therapy using internalizing aptamers isolated by cell-uptake selection", ACS Nano, 6:696–704.

[96] Perfezou M, Turner A, Merkoc, A.(2012). "Cancer detection using nanoparticle-based sensors", Chem Soc Rev, 41:2606–22.

[97] Lu Y, Low P.S., (2002). "Folate-mediated delivery of macromolecular anticancer therapeutic agents", Adv Drug Deliv Rev, 54:675–93.

[98] Chan, P., M. Kurisawa, J. E. Chung and Y.-Y. Yang (2007). "Synthesis and characterization of chitosan poly (ethylene glycol)-folate as a non-viral carrier for tumor-targeted gene delivery." Biomaterials 28(3): 540-549.

[99] Clementi, A. (2008). "Synthesis of Novel Targeted Drug Delivery Systems for Cancer Therapy", Dublin Institute of Technology, 05-01.

[100]http://www.rcsb.org/pdb/images/4KMY_asyr_r_250.jpg?bioNum=0 http://www.rcsb.org/pdb/images/4KM6_bio_r_500.jpg?bioNum=1, [accessed March 3, 2017].

[101] Martino D. A.(2014). "Chitosan Folic Acid as System for Site Specific Controlled Release", Tomas Bata University in Zlin, Czech Republic.

[102] Heath, J. R. and M. E. Davis (2008). "Nanotechnology and cancer." Annual review of medicine 59: 251.

[103] Ruo, L. (2012). "Chitosan Particles For The Controlled Release of Proteins", Politecnico di Torino.

[104] Zwicke, G. L., G. A. Mansoori and C. J. Jeffery (2012). "Utilizing the folate receptor for active targeting of cancer nanotherapeutics", Nano reviews 3.

[105] Safari, J. and Z. Zarnegar (2014). "Advanced drug delivery systems: Nanotechnology of health design A review." Journal of Saudi Chemical Society 18(2): 85-99.

[106] https://www.researchgate.net/figure/262303696_fig1_Figure-1-Different-types-of-nanocarriers-for-drug-delivery-A-Lipid-based-systems [accessed Nov 7, 2016]

[107] Garg T., Singh O., Arora S. (2011). "Dendrimer- A Novel Scaffold For Drug Delivery", RSR Murthy Department of Pharmaceutics, ISF College of Pharmacy, Moga (Punjab), India, Volume 7, Issue 2, Article-039

[108] Mukherjee, B., N. S. Dey, R. Maji, P. Bhowmik, P. J. Das and P. Paul (2014). "Current Status and Future Scope for Nanomaterials in Drug Delivery".

[109] Cho, K., X. Wang, S. Nie and D. M. Shin (2008). "Therapeutic nanoparticles for drug delivery in cancer." Clinical cancer research 14 (5): 1310-1316.

[110] Sonke S, Tomalia D.A. (2005). "Dendrimers in biomedical applications reflections on the Field", Advanced Drug Delivery Reviews, 57, 2106 – 2129.

[111] Vallejo A.: "Simulating Dendrimer Growth and Light Harvesting, Department of Chemical Engineering University of Illinois at Chicago".

[112] Barbara K, Maria B., (2001). "Review Dendrimers: properties and applications", Acta Biochimica Polonica, 48 (1), 199- 208.

[113] https://image.slidesharecdn.com/dendrimers-140804035037-phpapp01/95/dendrimers-a-recent-drug-delivery-system-19-638.jpg?cb=1407124400 [accessed March 3, 2017]

[114] Miyata K., Christie J.R., Kataoka K. (2011). "Polymeric Micelles for Nano-Scale Drug Delivery", Reactive & Functional Polymers,71, 227–234.

[115] Sennaroğlu Bostan M.(2015). "Preparation and Characterization of Gene and Drug Delivery Systems",.

[116] Yadav H.K.S., Nagavarma B.V. N, Ayaz A, Vasudha L.S, Shivakumar H.G. (2012). "Different Techniques for Preparation Of Polymeric Nanoparticles -A Review". Asian J Pharm Clin Res, Vol 5, Suppl 3, 16-23.

[117] Bianco A., Kostarelos K., Partidos C.D., Prato M. (2004). "Biomedical applications of functionalised carbon nanotubes", Advance Article on the web 21st December 2004.

[118] Attama A.A, Müller-Goymann C.C.,(2008). "Effect of Beeswax Modification on the Lipid Matrix and Solid Lipid Nanoparticle Crystallinity", Colloids Surf. A: Physicochem. Eng. Aspects.,315: 189-195.

[119] Wissing, S.A., Kayser O., Müller R.H., 2004. "Solid lipid nanoparticles for parenteral drug delivery", Advanced Drug Delivery Reviews, 56(9): p. 1257-1272.

[120] Ito A., Shinkai M., Honda H., Kobayashi T.(2005). "Medical application of functionalized magnetic nanoparticles " Volume 100, Issue 1, , Pages 1–1.

[121] Cao Q, Han X, Li L.(2011). "Enhancement of the efficiency of magnetic targeting for drug delivery: Development and evaluation of magnet system", J Magn Magn Mater, 323, 1919–1924.

[122] Figuerola A, Di Corato R, Manna L, Pellegrino T. (2010)."From iron oxide nanoparticles towards advanced iron-based inorganic materials designed for biomedical applications", Pharmacol Res, 62, 126–143.

[123] Asmatulu R, Zalich MA, Claus RO, Riffle J. (2005). "Synthesis, characterization and targeting of biodegradable magnetic nanocomposite particles by external magnetic fields", J. Magn Magn. Mater, 292, 108–119

[124] Chomoucka J, Drbohlavova J, Huska D, Adam V, Kizek R, Hubalem J.(2010). "Magnetic nanoparticles and targeted drug delivering", Pharm Res, 62, 144–149.

[125] Chang J.H, Kang K.H, Choi J, Jeong Y.K.(2008). "High efficiency protein separation with organosilane assembled silica coated magnetic nanoparticles", Superlattice Microst, 44, 442–448.

[126] Pan B.F., Gao F., Gu H.C.(2005), "Dendrimer modified magnetite nanoparticles for protein immobilization", J. Colloid Interface Sci, 284, 1–6.

[127] Grassi-Schultheiss P.P., Heller F., Dobson J. (1997). "Analysis of magnetic material in the human heart, spleen and liver", Biometals, 10, 351–355.

[128] Figuerola A., Di Corato R., Manna L., Pellegrino T. (2010). "From iron oxide nanoparticles towards advanced iron-based inorganic materials designed for biomedical applications", Pharmacol Res, 62, 126–143.

[129] Yallapu M.M, Othman S.F, Curtis E.T, Gupta B.K, Jaggi M., Chauhan S.C. (2011). "Multi-functional magnetic nanoparticles for magnetic resonance imaging and cancer therapy" Biomaterials, 32, 1890–1905.

[130] Wu W, Chen B, Cheng J, Wang J, Xu W, Liu L, Xia G.(2010). "Biocompatibility of Fe3O4/DNR magnetic nanoparticles in the treatment of hematologic malignancies", Int J Nanomedicine, 5, 1079–1084.

[131] Hafeli U.O., Riffle J.S., Harris-Shekhawat L., CarmichaelBaranauskas A., Mark F., Dailey J.P., Bardenstein D.(2009) "Cell uptake and in vitro toxicity of magnetic nanoparticles suitable for drug delivery", Mol Pharm, 6, 1417–1428.

[132] Dobrovolskaia M.A., McNeil S.E.(2007). "Immunological properties of engineered nanomaterials", Nat. Nano, 2, 469–478.

[133] Wilczewska A.Z., Niemirowicz K., Markiewicz K.H., Car H.(2012). "Nanoparticles as drug delivery systems", Institute of Pharmacology Polish Academy of Sciences, review.

[134] Kang, S.A., Jang, K.H., Seo, J.W., Kim, K.H., Kim, Y.H., Rairakhwada, D., Seo, M.Y., Lee, J.O., Ha, S.D., Kim, C.H., Rhee, S.K. (2009). "Levan: Applications and Perspectives, Microbial Production of Biopolymers and Polymer Precursors: Applications and Perspectives", ed: Bernd H.A. Rehm, Caister Academic Pres , 145-161.

[135] Chiang, C.J., Wang, J.Y., Chen, P.T. and Chao,Y.P. (2008). "Enhanced levan production using chitin-binding domain fused levansucrase immobilized on chitin beads", Applied Microbiology and Biotechnology.

[136] Poli, A., Kazak, H., Gurleyendag, B., Tommonaro, G., Pieretti, G., Oner, E.T., Nicolaus, B. (2009). "High Level Synthesis of Levan by a Novel Halomonas Species Growing on Defined Media". Carbohydr. Pol., 78 651-657.

[137] Mamay, Wahyuningrum D., Hertadi R.(2015). "Isolation and Characterization of Levan from Moderate Halophilic Bacteria *Bacillus licheniformis BK AG2*", Procedia Chemistry Volume 16, Pages 292-298.

[138] Oner T. E.,Hernández L., Combie J. (2016). 2016Review of Levan polysaccharide: From a century of past experiences to future prospects",Biotechnol Adv. Sep-Oct;34(5):827-44.

[139] Srikanth R., Reddy C.H.S., Siddartha G., Uppuluri K.B.(2014). "Review on production, characterization and applications of microbial levan", Carbohydrate Polymers, 120:102-114.

[140] Kim S.J., Chung B.H.(2016). "Antioxidant activity of levan coated cerium oxide nanoparticles", Carbohydr Polym 150, 400-407.

[141] Gupta S., Singh S.K., Das P., Mandal S.C. (2011). "Microbial levan, an ideal prebiotic and immunonutrient in aquaculture", World Aquaculture, 61-63.

[142] Han Y.W, Clark M.A.(1990). "Production and Characterization of Microbial Levan", J. Agric. Food Chem., 38 (2), pp 393–396.

[143] Abhishek S., Daria Z., Matthias S., Ullrich M. S. (2009). "Levanssucrase and levan formation in *Pseudomonas syringiae* and related organisms," in Bacterial Polysaccharides: Current Innovations and Future Trends ed. Ullrich M., editor. (Bremen: Caister Academic Press; ).

[144] Sennaroglu B.M., Cansever M.E., Kazak H., Keskin S.S., Oner E.T., Eroglu M.S. (2014). "Comprehensive characterization of chitosan/PEO/levan ternary blend films ",Carbohydrate Polymers, 102:993-1000.

[145] Bernd H., Rehm A. (2009). "Microbial Production of Biopolymers and Polymer Precursors: Applications and Perspectives", Horizon Scientific Press.

[146] Sturzoiu et al. (2011). "Zymomonas mobilis Levan is Involved in Metalloproteinases Activation in Healing of Wounded and Burned Tissues", Animal Science and Biotechnologies, 44 (1).

[147] Wu, Q., Zheng, C., Ning, Z.X., Yang, B. (2007). "Modification of Low Molecular Weight Polysaccharides from Tremella Fuciformis and Their Antioxidant Activity in Vitro", Int. J. Mol. Sci., 8 670-679.

[148] Huang, X., Hu, Y., Zhao, X., Lu, Y., Wang, J., Zhang, F., Sun, J. (2008). "Sulfated Modification can Enhance the Adjuvant Activity of Astragalus Polysaccharide for ND Vaccine",Carbohydr. Polym., 73 303-308.

[149] Menderes, S.F., Santos Jr, O.D., Barbosa, A.M., Vasconcelos, A.F.D., Aranda-Selverio, G., Monteiro, N.K., Dekker, R.F.H., Pereira, M.S., Tovar, A.M.F., Mourao, P.A.D.S., Corradi da Silva, M.D.L. (2009). "Sulfonation and Anticoagulant Activity of Botryosphaeran from Botryosphaeria rhodina MAMB-05 Grown on Fructose", Int. J. Biol. Macromol., 45 305-309.

[150] Robert,E., Boulevard, L. (1998). "Levan derivatives, their preparation, compositions and applications including medical and food applications" US patent, WO 98/03184.

[151] Costa et al.(2013). "Adhesive nanostructured multilayer films using a bacterial exopolysaccharide for biomedical applications", J. Mater. Chem. B**,** ,1, 2367-2374

[152] Leite A.J., Silva J.M., Ates O., Eroğlu M.S., Öner E., Mano J.F. (2014)."Bioadhesive and bioactive methacrylated nanocomposite levan-based beads for bone tissue applications"Presentation at 2nd International Conference on Biological and Biomimetic Adhesives, PP01-03, p. 85 (Available from URL: www.icbba2014.org/pdf/ICBBA2014_CONGRESS_BOOK.pdf).

[153] Kim Y.H., Kim J.G., Jang J.W., Lee S.Y., Heo W.B., Kim K.H. (2012). "Study on the synthesis of modified levan and its properties on the hair International Federation of Societies of Cosmetic Chemists", Johannesburg, South Africa, Poster Session5, Number 302 Available from URL: http://www.ifscc2012.co.za/coschem/index.cfm/scientific-programme/poster-session-5/

[154] Kim C. H., Rhee S. K., Kim K.H., Kim K. S., Han C. S., Choi B.R.(2005). "Beta-Fructosyl-L-Ascorbic Acid And The Preparation Method There of Technical Field"Bioland Ltd., Patent WO2005026183 A1.

[155] Bower D. I., Maddams W. F.(1989). "The Vibrational Spectroscopy of Polymers", Ed., R. W. Cahn, E. A. Davis and I. M. Ward, Cambridge University Press, Cambridge.

[156] Brian C. Smith, 2011. "Fundamentals of Fourier Transform Infrared Spectroscopy", Second Edition, CRC Press.

[157] http://articheck.co.uk/wp-content/uploads/2015/01/FT-IR.gif

[158] Cullity, B. D. (2009). "Element of x-ray diffraction", 2nd Ed., Addison- Wesley publishing company.

[159] Richard J. D. Tilley, (2006). "Crystals and Crystal Structures", John Wiley & Sons.

[160] Danilchenko S. N., Kukharenko O. G., Moseke C., Protsenko I. Y.U., Sukhodub L. F., Sulkio-Cleff B. (2002). Cryst. Res. Technol., 37, 11 1234.

[161] Wells O. G. (1974). "Scanning Electron Microscopy", McGraw-Hill, New York.

[162] https://wwuphoto.files.wordpress.com/2014/01/sem-training-2.pdf

[163] https://www.researchgate.net/figure/263849645_fig12_Figure-215-Schematic-Diagram-of-SEM-Scanning-electron-microscope.

[164] Reimer L. (2013). "Scanning Electron Microscopy: Physics of Image Formation and Microanalysis", Springer.

[165] http://earthscience.rice.edu/wp-content/uploads/2016/01/Electron-beam-sample-interaction.bmp.

[166] https://upload.wikimedia.org/wikipedia/commons/thumb/3/34/Electron_emission_mechanisms.svg/791px-Electron_emission_mechanisms.svg.png.

[167] Scanning Electron Microscope A to Z, Basic knowledge for using the SEM, JEOL.

[168] Bell, D.C., Garratt-Reed A.J. (2003). "Energy Dispersive X-ray Analysis in the Electron Microscope", Garland Science,

[169]https://www2.warwick.ac.uk/fac/sci/physics/current/postgraduate/regs/mpags/ex5/techniques/structural/tem

[170] http://www.nobelprize.org/educational/physics/microscopes/tem/

[171] Moudgil, H. K. (2014). "Textbook of Physical Chemistry", Phi Learning Pvt.

[172] Gabbott, P. (2008). "Principles and Applications of Thermal Analysis", John Wiley & Sons,

[173] http://www.rsic.iitb.ac.in/tg-dta.html ,

[174] Perkampus, H.H. (2013)., "UV-VIS Spectroscopy and Its Applications", Springer Science & Business Media.

[175] http://chemtech.org/cn/cn212/212-6.htm

[176] Binnig G., Quate C., Gerber, C. (1986). "Atomic Force Microscope", Physical Review Letters, 56: 930-933.

[177] Aguilar, Z. (2012). "Nanomaterials for Medical Applications", Newnes.

[178] Serry, F.M. (2010). "Application of Atomic Force Microscopy for Contact Lens Manufacturing".

[179] Bhardwaj S., Physics Practical For B.Tech. II Sem.

[180] Minges, M.L. (1989). "Elecronic Materials Handbook". Vol. 1 Electronic Package.Materials Park, OH: ASM.

[181] Foner, S. (1959). Rev. Sci. Inst., 30,548.

[182] Jaeger H., Pechan M.J. (2003). "A simple vibrating sample magnetometer for use in a materials physics course", Wesley Burgei Am. J. Phys., Vol. 71, No. 8.

[183] Jiles D.(2016). "Introduction to Magnetism and Magnetic Materials", Third Edition, page 63.

[184] Hooijschuur J.H. (2017). "Fluorescence Spectroscopy", Chromedia.

[185] Lakowicz J. R. (2007). " Principles of Fluorescence Spectroscopy", Springer Science & Business Media.

[186] https://upload.wikimedia.org/wikipedia/commons/thumb/9/91/Fluorimeter_Schema_einfach.png/1231px-Fluorimeter_Schema_einfach.png

[187] Yuan Y., Lee T.R. (2013). "Contact Angle and Wetting Properties, Surface Science Techniques" Springer Series in Surface Sciences pp 3-34,

[188] http://soft-matter.seas.harvard.edu/index.php/File:Contact_angle.png

[189] Gul I.H., Ahmed W., Maqsood A. (2008). "Electrical and magnetic characterization of nanocrystalline Ni–Zn ferrite synthesis by co-precipitation route", Journal of Magnetism and Magnetic Materials 320, 270–275.

[190] Sahoo B., Sahu S.K., Pramanik P.(2011). "A novel method for the immobilization of urease on phosphonate grafted iron oxide nanoparticle", Journal of Molecular Catalysis B: Enzymatic 69, 95–102.

[191] Küçükasik F., Kazak H., Güney D., Finore I., Poli A., Yenigün O.,Nicolaus B., Öner E. (2011). "Appl. Microbiol. Biotechnol. ", 89, 1729.

[192] Huang Q., Zhang L. (2011). Carbohydr. Polym., 83, 1363.

[193] Suflet D.M., Chitanu G.C., Popa V.I.(2006). React. Funct. Polym., 66, 1240.

[194] Suflet D.M., Chitanu G.C., Desbrières J. (2010). Carbohydr. Polym., 82, 1271.

[195] Axente E., Sima F., Ristoscu C., Mihailescu N., Mihailescu I. N. (2014) "Biopolymer Thin Films Synthesized by Advanced Pulsed Laser Techniques", Springer Series in Materials Science.

[196] Y. Kinemuchi, K. Ishizaka, H. Suematsu, W. Jiang, K. Yatsui, (2002). Thin Solid Films 407 109.

[197] Waldron R.D. (1955). , Phys. Rev. 99 1727–1735.

[198] Gul I.H., Pervaiz E. (2012). "Comparative study of $NiFe_{2-x}Al_xO4$ ferrite nanoparticles synthesized by chemical co-precipitation and sol–gel combustion techniques", Materials Research Bulletin 47 1353–1361.

[199] Gabal M.A., Al-Juaid A.A. , El-Rashed S., Hussein M.A.(2017). "Synthesis and characterization of nano-sized $CoFe_2O_4$ via facile methods: A comparative study", Materials Research Bulletin Volume 89, Pages 68–78.

[200] Gul I.H., Maqsood A., Naeem M., Naeem Ashiq M. (2010). "Optical, magnetic and electrical investigation of cobalt ferrite nanoparticles synthesized by co-precipitation route", Journal of Alloys and Compounds 507 201–206.

[201] Prabhakaran T., MangalarajaR.V., Denardin J.C., Jiménez J.A. (2017). "The effect of reaction temperature on the structural and magnetic properties of nano $CoFe_2O_4$", Ceramics International Volume 43, Issue 7, Pages 5599–5606.

[202] Srivastava V., Kohout T., Sillanpää M. (2016). "Potential of cobalt ferrite nanoparticles ($CoFe_2O_4$) for remediation of hexavalent chromium from synthetic and printing press wastewater", Journal of Environmental Chemical Engineering, Volume 4, Issue 3, Pages 2922–2932.

[203] Safi R.,Ghasemi A, Shoja-Razavi R., Ghasemi E., Sodaee T. (2016). "Rietveld structure refinement, cations distribution and magnetic features of CoFe2O4 nanoparticles synthesized by co-precipitation, hydrothermal, and combustion methods", Ceramics International, 42, 6375–6382.

[204] Manikandan V., Vanitha A., Kumar R.E., Kavita S. (2017). "Influence of sintering temperature on structural, dielectric and magnetic properties of Li substituted $CuFe_2O_4$ nanoparticles", Journal of Magnetism and Magnetic Materials, 426 11–17.

[205] Vadivela M., Ramesh Babua R., Ramamurthib K., Arivanandhanc M. (2017). "Enhanced dielectric and magnetic properties of polystyrene added $CoFe_2O_4$ magnetic nanoparticles", Journal of Physics and Chemistry of Solids , 102 1–11.

[206] Gul I.H., Maqsood A., Naeem M., Ashiq N.M.(2010). "Optical, magnetic and electrical investigation of cobalt ferrite nanoparticles synthesized by co-precipitation route", Journal of Alloys and Compounds , 507 201–206.

[207] Hudson A.S., (1968). Marconi Rev. 37 43.

[208] Gul I.H., Maqsood A. (2008). "Structural, magnetic and electrical properties of cobalt ferrites prepared by the sol–gel route", Journal of Alloys and Compounds , 465 227–231.

[209] Praveena K, Sadhana K., Srinath S., Murthy S. R.(2013). "Effect of pH on structural and magnetic properties of nanocrystalline Y3Fe5O12 by aqueous co-precipitation method", Materials Research Innovations DOI 10.1179/1433075X13Y.0000000116.

[210] Jagminas A., Kurtinaitienė M., Mažeika K.(2013). "Synthesis of cobalt ferrite nanoparticles by co-precipitation at ambient and hydrothermal conditions", Chemija. vol. 24. No. 2. P. 103–110.

[211] Fernándeza C. P., Zabottob F.L., Garciab D. , Kiminami Ruth H.G.A. (2016). "In situ sol–gel co-synthesis under controlled pH and microwave sintering of PZT/CoFe2O4 magnetoelectric composite ceramics", Ceramics International, 42 3239–3249.

[212] Nadir Osman.S.E.,Moyo T. (2015). "Influence of annealing process on the structure and magnetic behavior of $Ba_{0.5}Co_{0.5}Fe_2O_4$ nanoparticles", Physics Procedia, Volume 75, Pages 1133–1141.

[213] Zhu B. , Yang C. , Xie Q. , Zhang Y. , Ping Li. (2013). "Influence of Rapid Thermal Annealing on the Structure and Magnetic Properties of $CoFe_2O_4$ Films Prepared by Sol-Gel Method", Journal Ferroelectrics, Volume 445, Issue 1.

[214] T.E. Torres et al.,(2010). "Magnetic properties and energy absorption of $CoFe_2O_4$ nanoparticles for magnetic hyperthermia", Journal of Physics: Conference Series, Vol. 200, 72101. http://83.169.23.21/de/en/spectrum/ee-spectrum16/magnetic_hyperthermiamht-analysisofinductivenanoheating/

[215] Nadeem, K., Shahid M., Mumtaz M.(2014). "Competing crystallite size and zinc concentration in silica coated cobalt ferrite nanoparticles", Progress in Natural Science: Materials International Volume 24, Issue 3, Pages 199–204.

[216] Manikandan A., Sridhar R., Antony A.S., Ramakrishna S. (2014). " A simple aloe vera plant-extracted microwave and conventional combustion synthesis: Morphological, optical, magnetic and catalytic properties of CoFe2O4 nanostructure", Journal of Molecular Structure , 1076 188–200.

[217] Vadivel M., Ramesh Babu R., Ramamurthi K., Arivanandhan M. (2017). "Enhanced dielectric and magnetic properties of polystyrene added $CoFe_2O_4$ magnetic nanoparticles", Journal of Physics and Chemistry of Solids ,102 1–11.

[218] Sahoo B., Pramanik P., Sahu S.K. (2011). "A novel method for the immobilization of urease on phosphonate grafted iron oxide nanoparticle", Journal of Molecular Catalysis B: Enzymatic 69 95–102.

[219] Lee, C., Ostafin, A., Takagi, C. (2009). "Enhanced Emission of Gold Nanoparticles with Atypical Electron Transfer From Surface Bound Molecules to Gold Surface", AIChE Annual Meeting.

[220] Szymanska-Chargot M., Zdunek A. (2013). "Use of FT-IR Spectra and PCA to the Bulk Characterization of Cell Wall Residues of Fruits and Vegetables Along a Fraction Process", Food Biophys. , 8(1): 29–42.

[221] Nandakumar A. (2013). "Surface modification of electrospun fibre meshes by oxygen plasma for bone regeneration", Biofabrication, Volume 5, Number 1.

[222] Nadeem K., Shahid K., Mumtaz M.(2014). "Competing crystallite size and zinc concentration in silicacoated cobalt ferrite nanoparticles", Progress in Natural Science 24, 3.

[223] Zhu L., Ma J., Jia N., Zhao Y., Shen H.(2009)."Chitosan-coated magnetic nanoparticles as carriers of 5-fluorouracil: preparation, characterization and cytotoxicity studies", Colloids and Surfaces B: Biointerfaces, 68(1):1-6.

[224] Mushtaq M.W, Kanwal F., Batool A., Jamil T., Zia-ul-Haq M., Ijaz B., Huang Q., Ullah Z. "Polymer-coated CoFe2O4 nanoassemblies as biocompatible magnetic nanocarriers for anticancer drug delivery", Journal of Materials Science, 1-12.

[225] Hathout A.S., Aljawish A., Sabry B.A., El-Nekeety A.A., Roby M.H., Deraz N.M., Aly S.E., Abdel-Wahhab M.A.(2017) "Synthesis and characterization of cobalt ferrites nanoparticles with cytotoxic and antimicrobial properties", Journal of Applied Pharmaceutical Science, Vol. 7(01):086-92.

# APPENDIX

# BIBLIOGRAPHY

**Name Surname** : **Ilker CALGERIS**

**Place and Date of Birth** : **Karabuk / 15.3.1982**

**Language** : **English**

**E-mail** : **ilkercalgeris@gmail.com**

**Education**

| Degree | Department/Program | University/High School | Gaduation Year |
|---|---|---|---|
| High School | Mathematics | Karabük Demir Çelik Lisesi | 2000 |
| Bachelor of Science | Chemistry | Celal Bayar University | 2004 |
| Master of Science | Biochemistry | Marmara University | 2010 |

**Work Experience**

| Year | Company | Position |
|---|---|---|
| 2005-….. | Directorate General of Security | Officer |
| 2012-2015 | Ministry of Foreign Affairs | Attache |

# PUBLICATIONS:

1. Calgeris, İ.,Cakmakcı, E., Ogan,A.,Kayaman Apohan,N. "Preparation and drug release properties of lignin–starch biodegradable films" Starch - Starke 64(5) · May 2012.
2. Costa, R.R., Neto, I, A., Calgeris,I., Correia,R,C., Pinho,C,M,A., Fonseca,J., Öner T,E., Mano, F, J. "Adhesive nanostructured multilayer films using a bacterial exopolysaccharide for biomedical applications" J. Mater. Chem. B, 2013,**1**, 2367-2374

**PRESENTATIONS**

1. S. Rehman, I. Calgeris, M. Mujahid, E. T. Oner; Synthesis and Characterization of Bio-Compatible Ferromagnetic Hydroxyapatite Composite, International Conference on Nanoscale Magnetism (ICNM-2013), September 02– 06, 2013, Istanbul, Turkey